A GLOBALLY CONVERGENT NUMERICAL METHOD FOR COEFFICIENT INVERSE PROBLEMS

by

NATEE PANTONG

Presented to the Faculty of the Graduate School of

The University of Texas at Arlington in Partial Fulfillment

of the Requirements

for the Degree of

DOCTOR OF PHILOSOPHY

THE UNIVERSITY OF TEXAS AT ARLINGTON

August 2009

ACKNOWLEDGEMENTS

I would like to acknowledge and extend my heartfelt gratitude to my supervising professor Dr. Jianzhong Su for his constant motivation, encouragement and for making the completion of this dissertation possible.

I wish to thank my programming advisor Dr. Hua Shan for providing me invaluable resources and techniques in programming which is a significant portion of this dissertation and Dr. Hanli Liu for providing biomedical information. I also wish to thank Dr. Guojun Liao, Dr. Ren-Cang Li, Dr. Hristo V. Kojouharov and Dr. Gaik Ambartsoumian for their invaluable support and for taking time to serve on my dissertation committee.

I would like to extend my appreciation to Group Captain Utis Siricupt, Group Captain Prakasit Jareunying and Group Captain Vipada Koonkontod, the Royal Thai Air Force Officers, for their support, encouragement and for giving me an opportunity to pursue graduate studies. I am especially grateful to my programming languages instructors, Wing Commander Sompong Pokaseam and Wing Commander Tewa Kanchanachom.

I am grateful to all the teachers who taught me during the years I spent in school both in Thailand and in the Unites States. I also thank several of my friends who have supported me throughout my education.

Finally, I would like to express my deep gratitude to my mother Supatra, my brother Kua and my wife Isarinthip who have encouraged and inspired me. I am extremely grateful to my mother for her sacrifice, encouragement and patience.

June 29, 2009

ABSTRACT

A GLOBALLY CONVERGENT NUMERICAL METHOD FOR

COEFFICIENT INVERSE PROBLEMS

NATEE PANTONG, Ph.D.

The University of Texas at Arlington, 2009

Supervising Professor: Jianzhong Su

In our terminology "globally convergent numerical method" means a numerical method, whose convergence to a good approximation for the correct solution is independent of the initial approximation. A new numerical imaging algorithm of reconstruction of optical absorption coefficients from near infrared light data with a continuous-wave has been purposed to solves a coefficient inverse problem for an elliptic equation with the data generated by the source running along a straight line. A regularization process, so-called "exterior forward problem", for preprocessing data with noise on the boundary has also been purpose for the problem related to matching fluid in experiment. A rigorous convergence analysis shows that this method converges globally. A heuristic approach for approximating "tail-function" which is a crucial part of our problem has been performed and verified in numerical experiments, so as the global convergence. Applications to both electrical impedance and optical tomography are discussed. Numerical experiments in the 2D case are presented.

TABLE OF CONTENTS

LIST OF FIGURES

LIST OF TABLES

CHAPTER 1

INTRODUCTION

1.1 Introduction

In our terminology "globally convergent numerical method" means a numerical method, whose convergence to a good approximation for the correct solution for any initial approximation is guaranteed by mathematics proof. For commonly used locally convergent numerical method, the phenomenon of multiple local minima and ravines of least squares residual functions represent the major obstacle for reliable numerical solutions of Coefficient Inverse Problems (CIPs) for Partial Differential Equations (PDEs). Due to the applied nature of the discipline of Inverse Problems, the issue of addressing the problem of local minima has *vital importance* for this discipline. Indeed, any gradient-like optimization method of such a functional would likely to have convergence to a local minimum located far from the correct solution. The vast majority of current numerical method for CIPs are locally convergent ones, like, for example Newton-like method, see, e.g., [1][2][3][4] and many issues of Inverse Problems. That is, convergence of such a method to the true solution is rigorously guaranteed only if the initial guess is located sufficiently close to that solution. However, in the majority of applications such as e.g., medical and military ones, the optical media of interest is highly heterogeneous, which means that a good first guess is unknown. The latter naturally raises the question about the reliability of locally convergent numerical method for those applications, and this question is well known to many practitioners working on computations of real world Inverse Problems.

Thus, we are interested in the issue of globally convergent numerical methods for CIPs. We call a numerical method globally convergent if the following two conditions are in place: (1) a rigorous convergence analysis ensures that this method leads to a good approximation of the true solutions regardless on the availability of a first good guess, and (2) numerical experiments confirm the said convergence properly.

In this paper we present an globally convergent method for an CIP for the equation

$$\Delta w(\boldsymbol{x}, \boldsymbol{x}_0) - a(\boldsymbol{x}) w(\boldsymbol{x}, \boldsymbol{x}_0) = -\delta(\boldsymbol{x} - \boldsymbol{x}_0) \qquad (1.1)$$

$$\lim_{|\boldsymbol{x}| \to \infty} w(\boldsymbol{x}, \boldsymbol{x}_0) = 0. \qquad (1.2)$$

Here x_0 is the source position that runs along a line to generate the data for the inverse problem. We assume throughout this paper that the function $a(\boldsymbol{x}) \in C^\alpha(\mathbb{R}^2)$, $a \geq$ const. > 0 where $\alpha \in (0, 1)$. Uniqueness and existence of the solution of the problem (1.1) and (1.2) is such that $w \in C^{2+\alpha}(|\boldsymbol{x} - \boldsymbol{x}_0| \geq \varepsilon)$, for all $\varepsilon > 0$ follows from classic arguments, see [5] for further reference.

The first generation of globally convergent numerical methods has stated from the so-called convexification algorithm [5]. This algorithm was developed for the case of Coefficient Inverse Problems (CIPs) for hyperbolic and parabolic equations with incomplete data, the studies are based on frequency/time-dependent data. In particular, the convexification is used to treat CIPs for the elliptic equations, which are Laplace transforms of hyperbolic and parabolic ones. Here the seeked coefficients were dependent on the running parameter, i.e., the so-called 'pseudo frequency'. In the case of of optimal imaging of diffuse media this corresponds to the so-called constant wave (CW) light, theory and numerical implementations can be found in our work in [6]. At the same time, there is an applied interest in CIPs for elliptic equations with the data depending on the running source. This corresponds to the

constant current in the case of imaging of undersurface objects (e.g., land mines and underground bunkers) using the method electrical impedance tomography (EIT).

The essential difference between the frequency/time-dependent data and data depending on the running source, say CW, is that the effect of light distribution from far away light source (the so-called 'tail') cannot be neglected in the CW case while it can be set to zero in the frequency/time-dependent because of the clear asymptotic behavior of the Laplace transform of the solution of the forward problem.

In the past the authors have made several attempts to work out a globally convergent numerical method for this CIP. In our first publication [6], a heuristic approach of approximating the tail in CW case has been introduced where good numerical reconstruction of target coefficients $a(\boldsymbol{x})$ are obtained. We had developed the idea of heuristic iterative "accelerator" for convergence of tail and to confirm the desired globally convergence in [7]. Another version of globally convergence has been developed in [8]. Unlike all previous case where the globally convergent numerical methods are considered in rectangular domain, we have successfully implemented this method for a realistic physical domain (arbitrary convex shape domain). The approximation of the tail-function in the latter case is much more difficult because of the irregularity of unstructured mesh. The steps of converting the inverse problem for a realistic shape to an equivalent problem in an artificial rectangular region had been added to the algorithm in [7], the numerical results in our latest work still showed that the globally convergent numerical methods still holds in the arbitrary convex shape domain.

In Our previous work [6][7][8], we had rigorously prove global convergence by assuming that we know a good approximation for the tail-function, subsection 3.3.2, i.e. we assume that we know a good approximation of the forth term of the asymptotic behavior of the function $\ln[w(\boldsymbol{x}, \boldsymbol{x}_0)]$ for $|\boldsymbol{x}_0| \rightarrow \infty$, equation 3.18. Contrary to

those previous results, the new idea of making the tail-function small are presented in this paper and another version of globally convergence theorem are also proved. This idea is motivated by a globally convergent numerical method that was recently developed in [9]. However, the main difference of [9] with the current result is that in [9] the time dependent data were used. Because of that, the tail-function in [9] is small automatically as a high "pseudo frequency" limit of the solution of an associated forward problem resulting from the Laplace transform of the original hyperbolic equation.

We also purpose a new regularization method for filtering noisy boundary condition. This idea is originally from our work in [8]. Its basic idea is to use a "continuation" or "homotopy" method [10]. The homotopy method connects the system we want to solve with a different but related system that is easier to solve. In our case, our inverse reconstruction is a continuation of the reconstruction of an other diffusion tomography problem where the light source is very far away, called "tail-function".

1.2 Statement of the Inverse Problem and Applications

1.2.1 The Inverse Problem

Denote $\boldsymbol{x} = (x, y)$. Let $\Omega \subset \mathbb{R}^2$ be a bounded domain and $\Gamma = \partial\Omega$. Let B be a constant. Suppose that in equation (1.1) $\boldsymbol{x}_0 = (B, s) \notin \overline{\Omega}$. Determine the coefficient $a(\boldsymbol{x})$ for $\boldsymbol{x} \in \Omega$, assuming that the following function $\varphi(\boldsymbol{x}, \boldsymbol{x}_0)$ is given

$$w(\boldsymbol{x}, \boldsymbol{x}_0) = \varphi(\boldsymbol{x}, \boldsymbol{x}_0), \qquad \forall \boldsymbol{x} \in \Gamma, \quad \forall s \in [\underline{s}, \overline{s}], \tag{1.3}$$

where $\overline{s}$ is a sufficient large number, $\underline{s} < \overline{s}$ is a certain fixed number and

$$\{\boldsymbol{x}_0 \in (B, s), s \geq \underline{s}\} \cap \overline{\Omega} = \varnothing \,.$$

We consider the 2-D case for the sake of simplicity only for this complicated problem. Generalizations of our method on the 3-D case are feasible. We are unaware about

a existence and uniqueness result for this Inverse Problem. Nevertheless, because of applications, it is a priority to develop a globally convergent numerical method for this problem. The latter is the goal of this dissertation.

1.2.2   Applications

1.2.2.1 Electrical impedance tomography (EIT)

One of applications of the EIT is in search of land mines and underground bunkers via probing the ground by the constant current at different source locations. Let $v(\boldsymbol{x}, \boldsymbol{x}_0)$ be the voltage generated by the source of the constant current located at $\boldsymbol{x}_0$ and let $\sigma(\boldsymbol{x})$ be the electric conductivity of the medium, $\sigma(\boldsymbol{x}) \geq$ const. > 0. Then the function $v(\boldsymbol{x}, \boldsymbol{x}_0)$ satisfies the following equation

$$\nabla \cdot [\sigma(\boldsymbol{x})\nabla v(\boldsymbol{x}, \boldsymbol{x}_0)] = -\delta(\boldsymbol{x} - \boldsymbol{x}_0).$$

Replacing the function v with the function $w = v\sqrt{\sigma}$ and assuming that $\sigma(\boldsymbol{x}) = 1$ in a neighborhood of the source position $\boldsymbol{x}_0$ reduces above equation to equation (1.1) where

$$a(\boldsymbol{x}) = \frac{\Delta\left(\sqrt{\sigma(\boldsymbol{x})}\right)}{\sqrt{\sigma(\boldsymbol{x})}}.$$

Hence we arrive at the inverse problem (1.1) with the unknown coefficient in the latter form.

1.2.2.2 Optical diffusion tomography

In optical tomography, there are several types of light source to probe the light absorption and scattering media, figure 2.2. In our case, we use lasers with the CW light as the light source. The first application of the optical diffusion tomography is in optical medical imaging of tumor-like abnormalities both in human organs and small animals using near-infrared (NIR) light with the wavelength of light somewhere between 500 and 1000 nm [11]. The second feasible application is in optical imaging
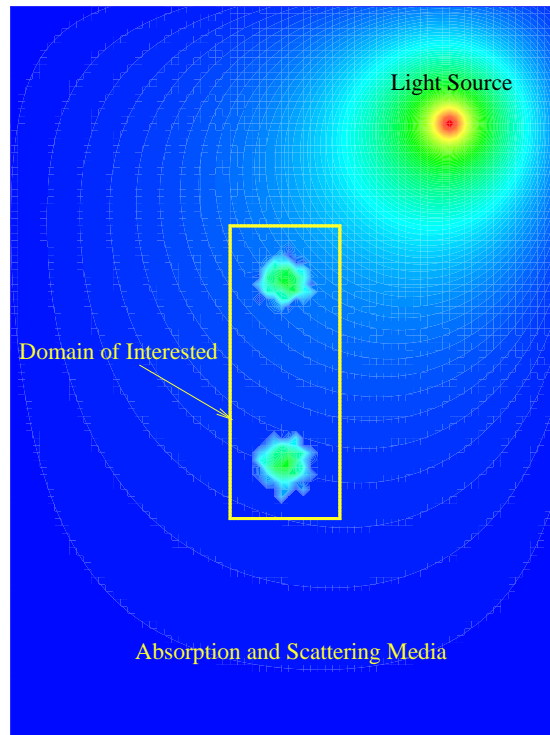
Figure 1.1. Optical Tomography Scheme.

of targets on battlefields via smog and flames using propagation of light originated by lasers. Both cases of transmitted and back reflected light are feasible in both applications. The light source should move along a straight line and the measurements of the output light should be performed at the boundary of the domain of interest. Interestingly, the diffuse-like propagation of light would be helpful, because the direct light can miss the target, one might still image it because photons would still 'sense' that target due to diffusion of light.

In this paper, we focus on the inverse problem of this application. The main purpose is to using NIR to probe light propagation in a diffuse medias in order to

distint derive images of their reduced scattering and absorption coefficient (μ_s and μ_a, respectively). The governing equation is Diffusion equation

$$\nabla \cdot [D(\boldsymbol{x})\nabla w(\boldsymbol{x}, \boldsymbol{x}_0)] - \mu_a w(\boldsymbol{x}, \boldsymbol{x}_0) = -\delta(\boldsymbol{x} - \boldsymbol{x}_0) \tag{1.4}$$

where $w(\boldsymbol{x})$ be the light intensity (solution of the diffusion equation) due to the light source located at $\boldsymbol{x}_0$, $D(\boldsymbol{x}) = 1/[3\mu'_s(\boldsymbol{x})]$. Both coefficients are measured in (1/cm). Details of simplifying above diffusion equation to equation (1.1) has been deduced in following.

1.3 Studying of Inverse Reconstruction Algorithm on Optical Diffusion Tomography

Near-infrared light (NIR) studies in biomedical fields have been quite extensive in resent years. Various efforts in NIR breast and brain imaging have been made by several research groups [12][13][14][15][16][17] in either laboratory or clinical studies. The targeted areas including detection of brain injury/trauma [18], determination of cerebrovascular hemodynamics and oxygenation [19][20], and functional brain imaging in response to a variety of neurological activations [21][22]. Frequency-domain (FD) breast imagers have been developed, and there have been reports of *in vivo* results of optical properties of abnormalities from female volunteers and patients [23].

The main biophysical mechanism of optical signals of NIR techniques is based on changes in the concentration of oxygenated hemoglobin (HbO) and deoxygenated hemoglobin (Hb). Moreover, increasing evidence points to the feasibility of NIR study of other human organs, such as the prostate and others [24][25][26][27]. As a low-cost alternative to FD imaging systems, continuous-wave NIR breast imaging systems have been developed in [14][28].

To spatially quantify light absorption and reduced scattering coefficients from NIR measurements, one needs to extract these quantities from mathematical models. Since these physical properties are described by coefficients in the corresponding diffusion model (1.4) or [29], one needs to solve an inverse problem based on the diffusion partial differential equation. Some of our work on the inverse reconstruction algorithm used for NIR tomographic imaging have been introduced in [6][7][8] where our latest results is the implementation of this algorithm in a real physical domain or arbitrary convex shape domain.

As mentioned earlier, this technique has been extended to the case of the running source instead of changing time or frequency. The original diffusion equation (1.4) has been studied as in [6][7][8], where the scattering coefficient μ'_s is assumed to be constant. This assumption is justified by the fact that in NIR applications the coefficient μ'_s usually changes quite slowly with respect to $\boldsymbol{x} \in \Omega$ for the wavelength between 500 to 1000 nm, whereas the absorption coefficient μ_a changes significantly, see, e.g., experimental studies in [30]. Furthermore, μ_a can be used for the diagnostics. By this assumption, one can set the coefficient $a(\boldsymbol{x})$ in (1.1) as

$$a(\boldsymbol{x}) = 3(\mu'_s \mu_a)(\boldsymbol{x})\,. \tag{1.5}$$

In chapter 2, we obtain a nonlinear integral differential equation, which is generated by the above Inverse Problem. This equation is independent on the unknown coefficient. Although a similar equation was obtained in [6][7][8], our current equation is the main novelty of this publication. This is because we divide both sides of the equation for the function $\ln w$ by s^2; which eventually leads to small tails. The main difficulty of our method consists in an approximate solution of that integral differential equation. We derive a layer stripping procedure for this solution and prove the convergence theorem. In chapter 3 we describe the numerical implementation

including our filtering technique, procedure of an enhanced approximation of tails, numerical computing of layer stripping and backward substitution. Results of numerical experiments are presented in chapter 4. Conclusion and discussion about this technique are presented in chapter 5.

CHAPTER 2

MATHEMATICAL MODEL

According to the inverse problem in subsection 1.2.1, the parameter B in $\boldsymbol{x}_0 = (B, s)$ is constant. We rewrite equation (1.1) to depend on $\boldsymbol{x}$ and s as following:

$$\Delta w(\boldsymbol{x}, s) - a(\boldsymbol{x})w(\boldsymbol{x}, s) = -\delta(x - B, y - s) \tag{2.1}$$

$$\lim_{|\boldsymbol{x}| \to \infty} w(\boldsymbol{x}, s) = 0. \tag{2.2}$$

And let's rewrite the inverse problem as following:

The inverse problem

Denote $\boldsymbol{x} = (x, y)$. Let $\Omega \subset \mathbb{R}^2$ be a bounded domain and $\Gamma = \partial\Omega$. Let B be a constant. Determine the coefficient $a(\boldsymbol{x})$ in equation (2.1) for $\boldsymbol{x} \in \Omega$, assuming that the following function $\varphi(\boldsymbol{x}, s)$ is given

$$w(\boldsymbol{x}, s) = \varphi(\boldsymbol{x}, s), \qquad \forall \boldsymbol{x} \in \Gamma, \quad \forall s \in [\underline{s}, \overline{s}], \tag{2.3}$$

where $\overline{s}$ is a sufficient large number, $\underline{s} < \overline{s}$ is a certain fixed number and

$$\{\boldsymbol{x}_0 \in (s, B), s \geq \underline{s}\} \cap \overline{\Omega} = \varnothing.$$

Now we consider the mathematical model for the inverse problem.

2.1 Nonlinear Integral Differential Equation

Since the source $\boldsymbol{x}_0 = (B, s) \notin \Omega$ and our inverse problem is performed in Ω domain, equation (2.1) can be written as

$$\Delta w(\boldsymbol{x}, s) - a(\boldsymbol{x})w(\boldsymbol{x}, s) = 0, \quad \boldsymbol{x} \in \Omega \tag{2.4}$$

10
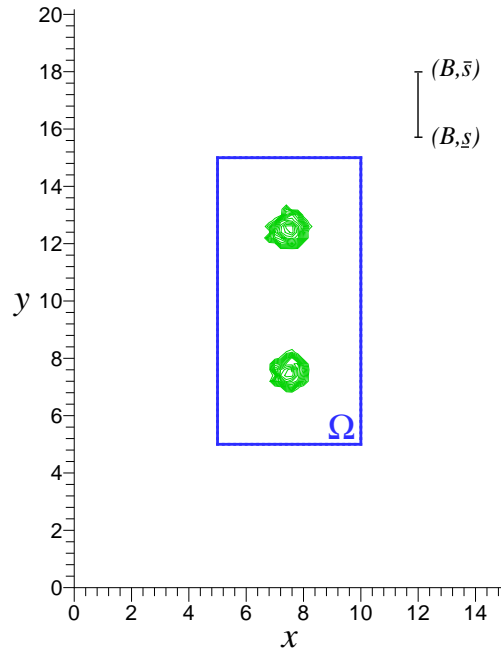
Figure 2.1. Show the geometry of inverse problem.

Function w is positive by the maximum principle, we can consider the function $u = \ln w$ and obtain the following equation from equation (2.4)

$$\Delta u(\boldsymbol{x}, s) + [\nabla u(\boldsymbol{x}, s)]^2 = a(\boldsymbol{x}) \tag{2.5}$$

$$u(\boldsymbol{x}, s) = \phi(\boldsymbol{x}, s) \quad \forall\, (\boldsymbol{x}, s) \in \Gamma \times (\underline{s}, \overline{s})\,, \tag{2.6}$$

where $\phi = \ln \varphi$. To eliminate the unknown coefficient $a(\boldsymbol{x})$ from equation (2.5), we differentiate it with respect to s and let

$$u(\boldsymbol{x}, s) = -\int_s^{\overline{s}} p(\boldsymbol{x}, \tau)\, d\tau + u(\boldsymbol{x}, \overline{s})\,, \quad \boldsymbol{x} \in \Omega\,, \quad s \in [\underline{s}, \overline{s}] \tag{2.7}$$

where $p(\boldsymbol{x}, s) = \frac{\partial}{\partial s} u(\boldsymbol{x}, s)$. The second term in equation (2.7), $u(\boldsymbol{x}, \overline{s})$, is the so-called "tail-function". We know only the first term of equation (2.7). As it was pointed out in the Introduction, if we would know the second term also, as it is the case of the time dependent data of [9], then we will have a standard integral

differential equations. However, the absence of the knowledge of this term significantly complicates the matter compared with [9]. Our development of heuristic procedure of an iterative approximation of the function $u(\boldsymbol{x}, \overline{s})$ in section 4.2 and result in section 7.2 of [7] showed good results of the inverse reconstruction of following nonlinear integral differential equation

$$\Delta p(\boldsymbol{x}, s) - 2\nabla p(\boldsymbol{x}, s) \int_{s}^{\overline{s}} \nabla p(\boldsymbol{x}, \tau) \, d\tau + 2\nabla p(\boldsymbol{x}, s) \cdot \nabla u(\boldsymbol{x}, \overline{s}) = 0 \,. \tag{2.8}$$

This paper is focused on the new technique of making tail-function small as in the globally convergent numerical methods [9] where the nonlinear integral differential equation are different from equation (2.8). We deduce the another form on inverse problem as following. Let

$$v(\boldsymbol{x}, s) = \frac{u(\boldsymbol{x}, s)}{s^2} \,. \tag{2.9}$$

Equation (2.5) becomes

$$\Delta v(\boldsymbol{x}, s) + s^2 [\nabla v(\boldsymbol{x}, s)]^2 = \frac{a(\boldsymbol{x})}{s^2} \tag{2.10}$$

Denote

$$q(\boldsymbol{x}, s) = \frac{\partial}{\partial s} v(\boldsymbol{x}, s) \,. \tag{2.11}$$

We have

$$\Delta q(\boldsymbol{x}, s) + 2s^2 \nabla q(\boldsymbol{x}, s) \cdot \nabla v(\boldsymbol{x}, s) + 2s[\nabla v(\boldsymbol{x}, s)]^2 = -2\frac{a(\boldsymbol{x})}{s^3} \,, \tag{2.12}$$

$$\boldsymbol{x} \in \Omega \,, \quad s \in (\underline{s}, \overline{s}]$$

where

$$v(\boldsymbol{x}, s) = -\int_{s}^{\overline{s}} q(\boldsymbol{x}, \tau) \, d\tau + v(\boldsymbol{x}, \overline{s}) \,, \quad \boldsymbol{x} \in \Omega \,, \quad s \in [\underline{s}, \overline{s}] \tag{2.13}$$

where $\overline{s}$ is a large number which will be chosen in numerical experiments. The new small tail-function in equation (2.13) is obtained by

$$v(\boldsymbol{x}, \overline{s}) = \frac{u(\boldsymbol{x}, \overline{s})}{\overline{s}^2} \,. \tag{2.14}$$

We obtain from equation (2.10), (2.12) and (2.13) the following "Nonlinear Integral Differential Equation"

$$\Delta q + 2s^2 \nabla q \cdot \left(- \int_s^{\bar{s}} \nabla q \, d\tau + \nabla \bar{v} \right) + 2s \left(- \int_s^{\bar{s}} \nabla q \, d\tau + \nabla \bar{v} \right)^2$$

$$= -\frac{2}{s} \left(- \int_s^{\bar{s}} \Delta q \, d\tau + \Delta \bar{v} \right) - 2s \left(- \int_s^{\bar{s}} \nabla q \, d\tau + \nabla \bar{v} \right)^2 , \qquad (2.15)$$

where $\bar{v} = v(\boldsymbol{x}, \bar{s})$.

In addition, equation (2.3),(2.9) and (2.11) imply that the following Dirichlet boundary condition is given for the function q

$$q(\boldsymbol{x}, s) = \psi(\boldsymbol{x}, s), \quad \forall \, (\boldsymbol{x}, s) \in \partial\Omega \times [\underline{s}, \bar{s}], \qquad (2.16)$$

where

$$\psi(\boldsymbol{x}, s) = \frac{\partial}{\partial s} \left(\frac{\ln \varphi(\boldsymbol{x}, s)}{s^2} \right). \qquad (2.17)$$

The problem (2.15), (2.16) is nonlinear. In addition both functions q and $\bar{v}$ are unknown here. Now the main question is *How to approximate well both functions q and $\bar{v}$ using (2.15), (2.16)?* The reason why we can approximate both these function is that we treat them differently. If we approximate them well (in a certain sense, specified below), then the target coefficient $a(\boldsymbol{x})$ would be reconstructed easily via backwards calculations, see subsection 3.3.4.

2.2   Layer Stripping with Respect to the Source Position

We now describe in detail how to discretize for s-variable. An analogue of the nonlinear equation of this section for a different CIP, in which the original PDE was either hyperbolic or parabolic was previous derived in [9]. However there are substantial different because [9] is a piecewise constant function but ours is piecewise linear continuous functions.
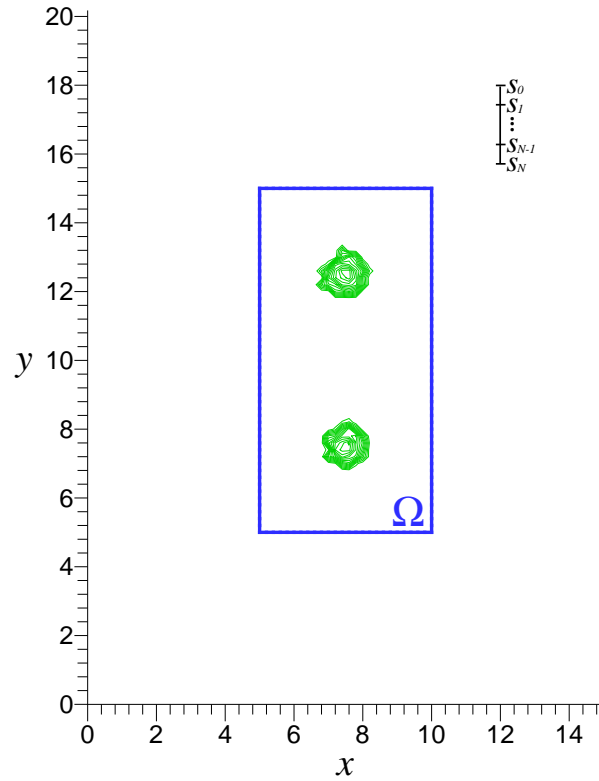
Figure 2.2. Show the geometry of layer stripping.

2.2.1 Nonlinear Equation

We approximate the function $q(\boldsymbol{x}, s)$ as a *piecewise linear continuous function* with respect to the pseudo frequency s. That is, we assume that there exists a partition

$$\underline{s} = s_N < s_{N-1} < \cdots < s_1 < s_0 = \overline{s}, \quad s_{n-1} - s_n = h \tag{2.18}$$

of the interval $[\underline{s}, \overline{s}]$ with sufficient small grid step size h such that

$$q(\boldsymbol{x}, s) = \frac{s_{n-1} - s}{h} q_n(\boldsymbol{x}) + \frac{s - s_n}{h} q_{n-1}(\boldsymbol{x}) \quad \text{for } s \in [s_n, s_{n-1}). \tag{2.19}$$

where $q_n(\boldsymbol{x}) = q(\boldsymbol{x}, s_n)$. We have following approximation by trapezoidal rule:

— for $s \in [s_n, s_{n-1})$, $n \geq 2$,

$$\int_s^{\bar{s}} q(\boldsymbol{x}, \tau) \, d\tau = \frac{s_{n-1} - s}{2} \big(q(\boldsymbol{x}, s) + q_{n-1}(\boldsymbol{x})\big) + \frac{h}{2} \left(q_0(\boldsymbol{x}) + 2 \sum_{j=1}^{n-2} q_j(\boldsymbol{x}) + q_{n-1}(\boldsymbol{x})\right).$$

— for $s \in [s_1, s_0)$,

$$\int_s^{\bar{s}} q(\boldsymbol{x}, \tau) \, d\tau = \frac{s_0 - s}{2} \big(q(\boldsymbol{x}, s) + q_0(\boldsymbol{x})\big).$$

— and for $s = s_0$,

$$\int_s^{\bar{s}} q(\boldsymbol{x}, \tau) \, d\tau = 0.$$

Hence for $s \in [s_n, s_{n-1})$, $n \geq 1$, we have

$$\int_s^{\bar{s}} q(\boldsymbol{x}, \tau) \, d\tau = \frac{s_{n-1} - s}{2} \big(q(\boldsymbol{x}, s) + q_{n-1}(\boldsymbol{x})\big)$$

$$+ \begin{cases} 0 & , n = 1 \\ \dfrac{h}{2} \left(q_0(\boldsymbol{x}) + 2 \displaystyle\sum_{j=1}^{n-2} q_j(\boldsymbol{x}) + q_{n-1}(\boldsymbol{x})\right) & , n \geq 2 \end{cases} \tag{2.20}$$

We approximate the boundary condition (2.16) as a piecewise linear continuous function,

$$\psi(\boldsymbol{x}, s) = \frac{s_{n-1} - s}{h} \psi_n(\boldsymbol{x}) + \frac{s - s_n}{h} \psi_{n-1}(\boldsymbol{x}), \text{ for } s \in [s_n, s_{n-1}) \text{ and } \boldsymbol{x} \in \partial\Omega, \tag{2.21}$$

where

$$\psi_n = \psi(\boldsymbol{x}, s_n). \tag{2.22}$$

We write equation (2.15) as

$$\Delta q - 2s^2 \nabla q \cdot \left(\int_s^{\bar{s}} \nabla q \, d\tau - \nabla \bar{v}\right) + 4s \left(\int_s^{\bar{s}} \nabla q \, d\tau - \nabla \bar{v}\right)^2$$

$$= \frac{2}{s} \left(\int_s^{\bar{s}} \Delta q \, d\tau - \Delta \bar{v}\right), \tag{2.23}$$

and we have that, for $n \geq 0$

$$
q_n^s(\boldsymbol{x}) = \begin{cases} q_0(\boldsymbol{x}) & , n = 0 \\[2ex] \dfrac{s_{n-1} - s}{h} q_n(\boldsymbol{x}) + \dfrac{s - s_n}{h} q_{n-1}(\boldsymbol{x}) & , n \geq 1 \text{ and } s \in [s_n, s_{n-1}) \end{cases} , \quad (2.24)
$$

$$
\psi_n^s(\boldsymbol{x}) = \begin{cases} \psi_0(\boldsymbol{x}) & , n = 0 \\[2ex] \dfrac{s_{n-1} - s}{h} \psi_n(\boldsymbol{x}) + \dfrac{s - s_n}{h} \psi_{n-1}(\boldsymbol{x}) & , n \geq 1 \text{ and } s \in [s_n, s_{n-1}) \end{cases} \quad (2.25)
$$

and

$$
T_n = \left\{ \begin{array}{ll} 0 & , n = 1 \\[2ex] \dfrac{h}{2}\left(q_0(\boldsymbol{x}) + 2 \sum_{j=1}^{n-2} q_j(\boldsymbol{x}) + q_{n-1}(\boldsymbol{x}) \right) & , n \geq 2 \end{array} \right\} - \bar{v} . \quad (2.26)
$$

We substitute equations (2.19), (2.20) and (2.21) to (2.23) to obtain

$-$ for $n = 0$

$$
\Delta q_0^s + 2s_0^2 \nabla q_0^s \cdot \nabla \bar{v} + 4s_0 (\nabla \bar{v})^2 = -\frac{2}{s_0} (\Delta \bar{v}) , \quad (2.27)
$$

note that we obtain above linear equation since

$$
\int_s^{\bar{s}} q(\boldsymbol{x}, \tau) \, d\tau = 0 ,
$$

$-$ and for $n \geq 1$

$$
\Delta q_n^s(\boldsymbol{x}) - 2s^2 \nabla q_n^s(\boldsymbol{x}) \cdot \nabla \left[\frac{s_{n-1} - s}{2} \left(q_n^s(\boldsymbol{x}) + q_{n-1}(\boldsymbol{x}) \right) + T_n \right]
$$

$$
+ 4s \left\{ \nabla \left[\frac{s_{n-1} - s}{2} \left(q_n^s(\boldsymbol{x}) + q_{n-1}(\boldsymbol{x}) \right) + T_n \right] \right\}^2
$$

$$
= \frac{2}{s} \Delta \left[\frac{s_{n-1} - s}{2} \left(q_n^s(\boldsymbol{x}) + q_{n-1}(\boldsymbol{x}) \right) + T_n \right] . \quad (2.28)
$$

Simplify equation (2.28) to obtain

$$
\Delta q_n^s(\boldsymbol{x}) - A_n (\nabla q_n^s)^2 - B_n \nabla q_n^s \nabla q_{n-1} - C_n \nabla q_n^s \nabla T_n
$$

$$
= D_n \Delta q_{n-1}(\boldsymbol{x}) + E_n \Delta T_n - F_n (\nabla q_{n-1})^2 - G_n \nabla q_{n-1} \nabla T_n - H_n (\nabla T_n)^2 \quad (2.29)
$$

where those new notations are defined here

$$A_n = \frac{s(s_{n-1} - s)(2s - s_{n-1})}{\left(1 - \frac{s_{n-1}-s}{s}\right)} = (s_{n-1} - s)s^2 \qquad , \quad |A_n| < h\bar{s}^2$$

$$B_n = \frac{s(s_{n-1} - s)(3s - 2s_{n-1})}{\left(1 - \frac{s_{n-1}-s}{s}\right)} = \frac{(s_{n-1} - s)(3s - 2s_{n-1})s^2}{2s - s_{n-1}} \quad , \quad |B_n| < 2h\bar{s}^2$$

$$C_n = \frac{(2s^2 - 4s(s_{n-1} - s))}{\left(1 - \frac{s_{n-1}-s}{s}\right)} = \frac{2s^2(3s - 2s_{n-1})}{2s - s_{n-1}} \qquad , \quad |C_n| < 4s^2$$

$$D_n = \frac{\frac{s_{n-1}-s}{s}}{\left(1 - \frac{s_{n-1}-s}{s}\right)} = \frac{s_{n-1} - s}{2s - s_{n-1}} \qquad , \quad |D_n| < h$$

$$E_n = \frac{\frac{2}{s}}{\left(1 - \frac{s_{n-1}-s}{s}\right)} = \frac{2}{2s - s_{n-1}} \qquad , \quad |E_n| < 1$$

$$F_n = \frac{s(s_{n-1} - s)^2}{\left(1 - \frac{s_{n-1}-s}{s}\right)} = \frac{s^2(s_{n-1} - s)^2}{2s - s_{n-1}} \qquad , \quad |F_n| < h\bar{s}^2$$

$$G_n = \frac{4s(s_{n-1} - s)}{\left(1 - \frac{s_{n-1}-s}{s}\right)} = \frac{4s^2(s_{n-1} - s)}{2s - s_{n-1}} \qquad , \quad |G_n| < h\bar{s}^2$$

$$H_n = \frac{4s}{\left(1 - \frac{s_{n-1}-s}{s}\right)} = \frac{4s^2}{2s - s_{n-1}} \qquad , \quad |H_n| < \bar{s}^2 .$$

$$(2.30)$$

From the inequalities in (2.30), we have

$$\max_{1 \leq n \leq N} \{|A_n|, |B_n|, |C_n|, |D_n|, |E_n|, |F_n|, |G_n|, |H_n|\}$$

are bounded. And especially

$$\max_{1 \leq n \leq N} \{|A_n|\} < h\bar{s}^2 .$$

With the latter term, by taking h small, we mitigate the influence of the nonlinear term with $(\nabla q_n^s)^2$ in equation (2.29), and we use this in our iterative algorithm via solving a linear problem on each iterative step.

2.2.2   Reconstruction of the Target Coefficient

Suppose that function $\{q_n\}_{n=0}^{N-1} = \{q_n^s\}_{n=0}^{N-1}$, where parameter s of q_n^s is evaluated at s_n, are approximated via solving problems (2.24), (2.25) and (2.29) and that the tail-function is also approximated. Then we construct the target coefficient $a(\boldsymbol{x})$ by backward calculation as follows. First we reconstruct the function $u_n(\boldsymbol{x}) = u(\boldsymbol{x}, s_n)$ by (2.9) as

$$
u_n(\boldsymbol{x}) =
\begin{cases}
s_0^2 v_\infty(\boldsymbol{x}) & , \ n = 0 \\[2mm]
s_n^2 \left[-\dfrac{h}{2} \left(q_0(\boldsymbol{x}) + 2 \sum_{j=1}^{n-1} q_j(\boldsymbol{x}) + q_n(\boldsymbol{x}) \right) + v_\infty(\boldsymbol{x}) \right] & , \ n \geq 1
\end{cases}
\tag{2.31}
$$

where $v_\infty(\boldsymbol{x})$ is approximation of tail-function $\bar{v}(\boldsymbol{x})$, the heuristic approach of approximation v_∞ are explained in subsection 3.3.2. In principle we can reconstruct the target coefficient $a(\boldsymbol{x})$ from equation (2.5). However, it is unstable to take second derivative. Hence, we first reconstruct the function $w_n(\boldsymbol{x}) = w(\boldsymbol{x}, s_n)$ as

$$
w_n(\boldsymbol{x}) = \exp[u_n(\boldsymbol{x})]. \tag{2.32}
$$

Next, we use equation (2.4) to obtain the coefficient $a_n(\boldsymbol{x})$ by numerical method, details are described in subsection 3.3.4.

2.2.3   The Algorithm for Approximating Function q_n^s

In this subsection we describe an algorithm of sequential solutions for $n = 0, \ldots, N$ of boundary value problem (2.25), (2.29), assuming that an approximation $v_\infty(\boldsymbol{x})$ for the tail-function is found, see subsection 3.3.2. For the sake of convenience of our analysis of our convergence analysis, we assume here and in section 2.3 that our domain of interest Ω is such that its boundary $\partial\Omega \in C^{2+\alpha}$, $\alpha =$const.> 0. We also assume that functions $\psi_n^s(\boldsymbol{x}) \in C^{2+\alpha}(\partial\Omega)$, $v_\infty \in C^{2+\alpha}(\partial\overline{\Omega})$, We rely on the classic Schauder theorem (§1 of Chapter 3 of [31]), which we reformulate in

subsection 2.3.2. In addition, we assume that for each n we make infinitely many inner iterations to ensure convergence of functions $q_{n,k}^s \in C^{2+\alpha}(\overline{\Omega})$, $k \to \infty$ to function q_n^s in space $C^{2+\alpha}(\overline{\Omega})$. This convergence is established in Theorem 2.3.2. Since it is practically impossible to arrange infinitely many iterations, this is one of discrepancies between our theory and computational practice. We describe all major discrepancies in subsection 3.3.3.

Step 0. We need to find an approximation for the function q_0^s. To do this, we solve equation (2.27) for q_0^s with boundary condition (2.25) and use v_∞ instead of $\bar{v}$ as follows

$$\Delta q_0^s + 2s_0^2 \nabla q_0^s \cdot \nabla v_\infty + 4s_0(\nabla v_\infty)^2 = -\frac{2}{s_0}(\Delta v_\infty) \tag{2.33}$$

Note that we obtain above linear equation since

$$\int_s^{\bar{s}} q(\boldsymbol{x}, \tau) \, d\tau = 0 \,.$$

The reconstruction of $a_0(\boldsymbol{x})$ is obtained using equations (2.31),(2.32) and (2.4).

Before beginning of *Step 1*, we substitute the actual $\bar{v}$ in equation (2.26) with approximation v_∞ as following:

$$T_n = \left\{ \begin{array}{ll} 0 & , \; n = 1 \\ \dfrac{h}{2}\left(q_0^s\left(\boldsymbol{x}\right) + 2\sum_{j=1}^{n-2} q_j^s\left(\boldsymbol{x}\right) + q_{n-1}^s(\boldsymbol{x}) \right) & , \; n \geq 2 \end{array} \right\} - v_\infty \,.$$

Step 1. We now find an approximation for the function q_1^s. To do this, we solve equation (2.28) with the boundary condition (2.25) at $n = 1$ iteratively for q_1^s. That is, we should solve

$$\Delta q_1^s\left(\boldsymbol{x}\right) - A_1(\nabla q_1^s)^2 - B_1 \nabla q_1^s \nabla q_0^s - C_1 \nabla q_1^s \nabla T_1$$

$$= D_1 \Delta q_0^s\left(\boldsymbol{x}\right) + E_1 \Delta T_1 - F_1(\nabla q_0^s)^2 - G_1 \nabla q_0^s \nabla T_1 - H_1(\nabla T_1)^2 \,. \tag{2.34}$$

We solve equation (2.34) iteratively as

$$\Delta q_{1,k}^s(\boldsymbol{x}) - A_1 \nabla q_{1,k}^s \nabla q_{1,k-1}^s - B_1 \nabla q_{1,k}^s \nabla q_0^s - C_1 \nabla q_{1,k}^s \nabla T_1$$

$$= D_1 \Delta q_0^s(\boldsymbol{x}) + E_1 \Delta T_1 - F_1 (\nabla q_0^s)^2 - G_1 \nabla q_0^s \nabla T_1 - H_1 (\nabla T_1)^2. \quad (2.35)$$

with $q_{1,k}^s(\boldsymbol{x})$ having same boundary condition as $q_1^s(\boldsymbol{x})$ and $q_{1,0}^s = q_0^s$

We proceed with calculating the function $q_{1,k+1}^s$ as in (2.35). We iterate in (2.35) until the process converges, i.e.,

$$\lim_{k \to \infty} \|q_{1,k}^s - q_{1,k-1}^s\|_{L_2(\Omega)} = 0.$$

We set $q_1^s := q_{1,k}^s$. The next reconstruction $a_1(\boldsymbol{x})$ is obtained using equations (2.31),(2.32) and (2.4).

Step n. We now find an approximation for the function q_n^s assuming that function $q_0^s, \ldots, q_{n-1}^s$ with respect to $s_0, \ldots, s_{n-1}$, respectively, are found. We solve iteratively equation (2.28) with the boundary condition (2.25) at arbitrary $n > 1$ as following

$$\Delta q_{n,k}^s(\boldsymbol{x}) - A_n \nabla q_{n,k}^s \nabla q_{n,k-1}^s - B_n \nabla q_{n,k}^s \nabla q_{n-1}^s - C_n \nabla q_{n,k}^s \nabla T_n$$

$$= D_n \Delta q_{n-1}^s(\boldsymbol{x}) + E_n \Delta T_n - F_n (\nabla q_{n-1}^s)^2 - G_n \nabla q_{n-1}^s \nabla T_n - H_n (\nabla T_n)^2. \quad (2.36)$$

with $q_{n,k}^s(\boldsymbol{x})$ having same boundary condition as $q_n^s(\boldsymbol{x})$ and $q_{n,0}^s = q_{n-1}^s$. We iterate until the precess converges, i.e., until

$$\lim_{k \to \infty} \|q_{n,k}^s - q_{n,k-1}^s\|_{L_2(\Omega)} = 0.$$

We set $q_n^s = q_{n,k}^s$. Then $a_n(\boldsymbol{x})$ is obtained using equations (2.31),(2.32) and (2.4).

Then we find function $a_0, \ldots, a_{N-1}$ where N is the number of subintervals of the interval $[\underline{s}, \overline{s}]$. Finally, the resulting function $a(\boldsymbol{x})$ is

$$a(\boldsymbol{x}) = \frac{1}{N} \sum_{n=0}^{N-1} a_n(\boldsymbol{x}). \quad (2.37)$$

2.3   Convergence

Below we follow the concept of Tikhonov for ill-posed problems [32], which is one of backbones of this theory. By this concept one should assume first that there exists an "ideal" exact solution of the problem with the exact data. Next, one should assume the presence of an error in the data of the level ζ, where $\zeta > 0$ is a small parameter. Suppose that an approximate solution is constructed for an sufficiently small ζ. This solution is called a "regularized solution", if the ζ-dependent family of these solutions tends to that exact solution as ζ tends to zero. Hence, one should prove this convergence (Theorem 2.3.2).

In this section we use the Schauder's theorem [31] to estimate function $q_{n,k}^s$. Since the Schauder's theorem requires $C^{2+\alpha}$ smoothness of the boundary $\partial\Omega$, we assume in this section that $\Omega \in \mathbb{R}^2$ is a convex bounded domain with $\partial\Omega \in C^{2+\alpha}$. This is in a disagreement with our domain Ω is rectangle. However we use the rectangle only because of the problem of tail-function, in which we cannot approximate it well heruistically for the case of a more general domain. However, an analogue of our convergence result (Theorem 2.3.2) can be proven for the case when Ω is rectangle and an FEM (i.e. discrete) version of equation (2.27) and (2.29) is considered with a fixed number R of finite elements. To do this, one need to consider the weak formulation of equation (2.27) and (2.29) and to use the Lax-Migram theorem [33] instead of the Schauder's theorem. Although the Lax-Migram theorem would provide only estimates of H^1 norms of functions q_n^s rather than more desirable C^2 norms, but using the equivalency of norm in finite dimensional spaces, we can still get estimates of C^2 norms and these estimates would naturally depend on R.

2.3.1 Exact Solution

Following the Tikhonov concept, we need to introduce the definitions of the exact solution first. We assume that there exists an exact coefficient function $a^*(\boldsymbol{x}) \in C^\alpha(\overline{\Omega})$, where constant $\alpha \in (0,1)$, which is a solution of our Inverse Problem. Let the function

$$w^*(\boldsymbol{x}, s) \in C^{2+\alpha}(|\boldsymbol{x} - \boldsymbol{x}_0| \geq \varepsilon), \ \forall \varepsilon > 0, \ \forall \boldsymbol{x}_0 = (B, s) > 0, \forall s \in [\underline{s}, \overline{s}]$$

be the solution of the problem (2.1), (2.2) with $a(\boldsymbol{x}) := a^*(\boldsymbol{x})$. Let

$$u^*(\boldsymbol{x}, s) = \ln w^*(\boldsymbol{x}, s), \ q^*(\boldsymbol{x}, s) = \frac{\partial u^*(\boldsymbol{x}, s)}{\partial s}, \ u_\infty^*(\boldsymbol{x}) = u^*(\boldsymbol{x}, \overline{s}).$$

By equation (2.5)

$$\Delta u^*(\boldsymbol{x}, s) + [\nabla u^*(\boldsymbol{x}, s)]^2 = a^*(\boldsymbol{x}). \tag{2.38}$$

Also, the function q^* satisfies the following analogue of equation (2.23)

$$\Delta q^* - 2s^2 \nabla q^* \cdot \left(\int_s^{\overline{s}} \nabla q^* \, d\tau + \nabla \overline{v}^* \right) + 4s \left(\int_s^{\overline{s}} \nabla q^* \, d\tau - \nabla \overline{v}^* \right)^2$$
$$= \frac{2}{s} \left(\int_s^{\overline{s}} \Delta q^* \, d\tau - \Delta \overline{v}^* \right) \tag{2.39}$$

with the boundary condition (2.16)

$$q^*(\boldsymbol{x}, s) = \psi^*(\boldsymbol{x}, s), \quad \forall (\boldsymbol{x}, s) \in \partial\Omega \times [\underline{s}, \overline{s}], \tag{2.40}$$

where $\psi^*(\boldsymbol{x}, s) = \frac{\partial}{\partial s} \ln \varphi^*(\boldsymbol{x}, s)$, where $\varphi^*(\boldsymbol{x}, s) = w^*(\boldsymbol{x}, s)$ for $(\boldsymbol{x}, s) \in \partial\Omega \times [\underline{s}, \overline{s}]$.

Definition. We call the function $q^*(\boldsymbol{x}, s)$ the *exact solution* of the problem (2.23), (2.16) with the *exact boundary* condition $\psi^*(\boldsymbol{x}, s)$. Naturally, the function $a^*(\boldsymbol{x})$ from equation (2.38) is called the exact solution of our Inverse Problem.

Therefore

$$q^*(\boldsymbol{x}, s) \in C^{2+\alpha}(\overline{\Omega}) \times C^1[\underline{s}, \overline{s}]. \tag{2.41}$$

We now approximate the function $q_n^*(\boldsymbol{x})$, $n \geq 0$, for representing the function $q^*(\boldsymbol{x}, s)$ as follows

— for $n = 0$

$$q_0^*(\boldsymbol{x}) = q^*(\boldsymbol{x}, s_0)$$

— and for $n \geq 1$, for any $s \in [s_n, s_{n-1})$ by averaging

$$q_n^*(\boldsymbol{x}) = \frac{1}{h} \int_{s_n}^{s_{n-1}} q^*(\boldsymbol{x}, s) \, ds \,, \quad \psi_n^*(\boldsymbol{x}) = \frac{1}{h} \int_{s_n}^{s_{n-1}} \psi^*(\boldsymbol{x}, s) \, ds$$

Then by (2.41) for $n \geq 1$

$$q^*(\boldsymbol{x}, s) = q_n^*(\boldsymbol{x}) + Q_n(\boldsymbol{x}, s) \,, \qquad \psi^*(\boldsymbol{x}, s) = \psi_n^*(\boldsymbol{x}) + \Psi_n(\boldsymbol{x}, s) \tag{2.42}$$

$s \in [s_n, s_{n-1})$, where functions Q_n, Ψ_n are such that for $s \in [s_n, s_{n-1})$

$$\|Q_n(\boldsymbol{x}, s)\|_{C^{2+\alpha}(\overline{\Omega})} \leq C^* h \,, \quad \|\Psi_n(\boldsymbol{x}, s)\|_{C^{2+\alpha}(\overline{\Omega})} \leq C^* h \,,$$

$$\forall s \in [s_n, s_{n-1}) \,, \quad n = 1, \ldots, N \,, \tag{2.43}$$

where the constant $C^* > 0$ depends only on $C^{2+\alpha}(\overline{\Omega}) \times C^1[\underline{s}, \overline{s}]$ and $C^{2+\alpha}(\overline{\Omega}) \times C^1[\underline{s}, \overline{s}]$ norms of function q^* and ψ^* respectively. Hence

$$q_n^*(\boldsymbol{x}) = \psi_n^*(\boldsymbol{x}) \,, \quad \boldsymbol{x} \in \partial\Omega \,, \tag{2.44}$$

and the following analog of equations (2.33) and (2.36) hold

$$\Delta q_0^* + 2s_0^2 \nabla q_0^* \cdot \nabla \bar{v}^* + 4s_0 (\nabla \bar{v}^*)^2 = -\frac{2}{s_0} (\Delta \bar{v}^*) \tag{2.45}$$

and

$$\Delta q_n^*(\boldsymbol{x}) - A_n (\nabla q_n^*)^2 - B_n \nabla q_n^* \nabla q_{n-1}^* - C_n \nabla q_n^* \nabla T_n^*$$

$$= D_n \Delta q_0^*(\boldsymbol{x}) + E_n \Delta T_n^* - F_n (\nabla q_0^*)^2 - G_n \nabla q_0^* \nabla T_n^* - H_n (\nabla T_n^*)^2 + R_n(\boldsymbol{x}, h) \tag{2.46}$$

with

$$T_n^* = \begin{cases} 0 & , \ n = 1 \\ \dfrac{h}{2}\left(q_0^*(\boldsymbol{x}) + 2\displaystyle\sum_{j=1}^{n-2} q_j^*(\boldsymbol{x}) + q_{n-1}^*(\boldsymbol{x}) \right) & , \ n \geq 2 \end{cases} - \bar{v}^* \,,$$

respectively, where the function $R_n(\boldsymbol{x}, h) \in C^\alpha(\overline{\Omega})$ and

$$\max_{1 \leq n \leq N} \|R_n(\boldsymbol{x}, h)\|_{C^{2+\alpha}(\overline{\Omega})} \leq C^* h \quad , \ n = 1, 2, \ldots, N \tag{2.47}$$

We also assume that the data $\varphi(\boldsymbol{x}, s)$ in (2.3) are given with error. This naturally produces an error in the function $\psi(\boldsymbol{x}, s)$ in (2.16). An additional error is introduced due to taking the average value of $\psi^*(\boldsymbol{x}, s)$ over the interval $[s_n, s_{n+1})$. Hence, it is reasonable to assume that

$$\|\psi_n^*(\boldsymbol{x}) - \psi_n^s(\boldsymbol{x})\|_{C^{2+\alpha}(\partial\Omega)} \leq C_1(\sigma + h)\,, \tag{2.48}$$

where $\sigma > 0$ is a small parameter characterizing the level of the error in the data $\varphi(\boldsymbol{x}, s)$ and the constant $C_1 > 0$ is independent on numbers σ, h and n.

Remark It should be noted that usually the data $\varphi(\boldsymbol{x}, s)$ in (2.3) are given a random noise. Although the differentiation of the noisy data is an ill-posed problem, but there exist effective numerical regularization methods of its solution, see subsection 3.3.1 for our way of handling it.

2.3.2 Convergence Theorem

First, we reformulate the Schauder's theorem in a way, which is convenient for our case, see §1 of Chapter 3 of [31] for this theorem. Introduce the positive constant M^* by letting

$$B^* = 12\bar{s}^2 \cdot \max\{S^*, 1\}$$

and

$$M^* = B^* \cdot \max\left\{ \max_{0 \leq n \leq N} \|q_n^*\|_{C^{2+\alpha}(\overline{\Omega})}, \max_{0 \leq m,n \leq N} \|q_m^*\|_{C^{2+\alpha}(\overline{\Omega})} \|q_n^*\|_{C^{2+\alpha}(\overline{\Omega})}, C^*, C_1, 2 \right\}$$

where C^*, C_1 are constants from (2.47), (2.48), respectively, and $S^* = \bar{s} - \underline{s}$. Consider the Dirichlet boundary value problem

$$\Delta\tilde{q} + \sum_{j=1}^{3} b_j(\boldsymbol{x})\tilde{q}_{x_j} - d(\boldsymbol{x})\tilde{q} = f(x), \quad x \in \Omega,$$

$$\tilde{q}\Big|_{\partial\Omega} = g(x) \in C^{2+\alpha}(\overline{\Omega}),$$

where functions

$$b_j, d, f \in C^{\alpha}(\overline{\Omega}), \quad d(\boldsymbol{x}) \geq 0; \quad \max\left(\|b_j\|_{C^{2+\alpha}(\overline{\Omega})}, \|d\|_{C^{2+\alpha}(\overline{\Omega})}\right) \leq M^*.$$

By the Schauder theorem there exists unique solution $\tilde{q} \in C^{2+\alpha}(\overline{\Omega})$ of this problem and with a constant $K = K(M^*, \Omega) > 0$ the following estimate holds

$$\|\tilde{q}\|_{C^{2+\alpha}(\overline{\Omega})} \leq K\left[\|g\|_{C^{2+\alpha}(\overline{\Omega})} + \|f\|_{C^{2+\alpha}(\overline{\Omega})}\right].$$

For the tail-function, we choose a small number $\xi \in (0,1)$ and by equation (2.14) we can choose such $\bar{s}^2 = \bar{s}^2(\xi) >> 1$ such that

$$\|\bar{v}^*\|_{C^{2+\alpha}(\overline{\Omega})} \leq \xi.$$

Theorem 2.3.2

Let $\Omega \subset \mathbb{R}^2$ be a convex bounded domain with the boundary $\partial\Omega \in C^{2+\alpha}$. Suppose that an approximation v_{∞} for the tail is constructed in such a way that

$$\|v_{\infty}\|_{C^{2+\alpha}(\overline{\Omega})} \leq \xi, \tag{2.49}$$

where $\xi \in (0,1)$ is a sufficient small number and that this function v_{∞} is used in (2.33),(2.35) and (2.36). Denote $\eta = \max\{\sigma, h, \xi\}$, σ is noise level of data and h is step size, and suppose that the number $Nh = \bar{s} - \underline{s}$ is such that

$$Nh < \frac{1}{20KM^*}. \tag{2.50}$$

Then there exists a sufficiently small number $\eta_0 = \eta_0(K(M^*, \Omega), M^*, c, \underline{s}, \overline{s}) \in (0, 1)$ such that for all $\eta \in (0, \eta_0)$ and for every integer $n \in [0, N-1]$ the following estimates hold

$$\|q_{\tilde{n}}^s - q_n^*\|_{C^{2+\alpha}(\overline{\Omega})} \leq KM^*(20\eta), \tag{2.51}$$

$$\|q_{\tilde{n}}^s\|_{C^{2+\alpha}(\overline{\Omega})} \leq 2M. \tag{2.52}$$

2.3.3   Proof of Theorem 2.3.2

This proof basically consists in estimating differences between our constructed functions $q_{n,k}^s$, and function q_n^*. We are doing this using the Schauder theorem. In this proof we assume that $\eta \in (0, \eta_0)$. Denote

$$\tilde{q}_{n,k}(\boldsymbol{x}) = q_{n,k}^s(\boldsymbol{x}) - q_n^*(\boldsymbol{x}), \ \ \tilde{v}_\infty(\boldsymbol{x}) = v_\infty(\boldsymbol{x}) - \bar{v}^*(\boldsymbol{x}),$$

$$\tilde{\psi}_n(\boldsymbol{x}) = \psi_n^s(\boldsymbol{x}) - \psi_n^*(\boldsymbol{x}), \ \ \tilde{T}_n(\boldsymbol{x}) = T_n(\boldsymbol{x}) - T_n^*(\boldsymbol{x}). \tag{2.53}$$

Note that, in this theorem $\|\cdot\|$ is equivalent to $\|\cdot\|_{C^{2+\alpha}(\overline{\Omega})}$. The proof basically consists in estimating these differences. (Detail of derivations of their estimated are shown in appendix A).

First we show the approximation of T_n, T_n^* and $\tilde{T}_n$. For $n = 1$ we have

$$\|T_1\| \leq \xi \ \ , \ \ \ \|T_1^*\| \leq \xi \ \ \text{and} \ \ \ \|\tilde{T}_1\| \leq 2\xi.$$

And for $n \geq 2$ we have

$$\begin{aligned} \|T_n\| \ &\leq \ h \sum_{j=0}^{n-1} \|\tilde{q}_j\| + S^* \max_{0 \leq j \leq n-1} \|q_j^*\| + \xi \\ \|T_n^*\| \ &\leq \ S^* \max_{0 \leq j \leq n-1} \|q_j^*\| + \xi \\ \|\tilde{T}_n\| \ &\leq \ h \sum_{j=0}^{n-1} \|\tilde{q}_j\| + 2\xi. \end{aligned}$$

First, we estimate $\tilde{q}_0$. Subtract equation (2.45) from (2.33). We obtain

$$\Delta\tilde{q}_0 + 2s_0^2\nabla\tilde{q}_0\nabla v_\infty = -2s_0^2\nabla q_0^*\nabla(v_\infty-\bar{v}^*) - 4s_0\nabla(v_\infty-\bar{v}^*)\nabla(v_\infty+\bar{v}^*) - \frac{2}{s_0}\Delta(v_\infty-\bar{v}^*),$$
(2.54)

$$\tilde{q}_0 = \tilde{\psi}_0 \quad, \quad \text{on } \partial\Omega.$$

Since $\|2s_0^2 v_\infty\| \leq 4\bar{s}^2\|\bar{v}^*\| \leq M^*$, by Schauder theorem, we have

$$\|\tilde{q}_0\| \leq KM^*(5\eta).$$
(2.55)

And hence

$$\|q_0^s\| = \|\tilde{q}_0 + q_0^*\| \leq \|\tilde{q}_0\| + \|q_0^*\| \leq KM^*(5\eta) + M^* \leq 2M^*.$$
(2.56)

Second, we estimate $\tilde{q}_{1,1}$. Set in equation (2.46) $n = 1$ and subtract it from (2.35) at $k = 1$, recalling that $q_{1,0}^s = q_0^s$. We obtain

$$\Delta\tilde{q}_{1,1} - A_1\nabla\tilde{q}_{1,1}\nabla\tilde{q}_0 - A_1\nabla\tilde{q}_{1,1}\nabla q_0^* - B_1\nabla\tilde{q}_{1,1}\nabla\tilde{q}_0 - B_1\nabla\tilde{q}_{1,1}\nabla q_0^* - C_1\nabla\tilde{q}_{1,1}\nabla T_1$$

$$= A_1\nabla q_1^*\nabla\tilde{q}_0 + A_1\nabla q_1^*\nabla q_0^* - A_1\nabla q_1^*\nabla q_1^* + B_1\nabla q_1^*\nabla\tilde{q}_0 + C_1\nabla q_1^*\nabla\tilde{T}_1$$

$$+ D_1\Delta\tilde{q}_0 + E_1\Delta\tilde{T}_1 - F_1\nabla\tilde{q}_0\nabla\tilde{q}_0 - 2F_1\nabla\tilde{q}_0\nabla q_0^*$$

$$- G_1\nabla\tilde{q}_0\nabla T_1 - G_1\nabla q_0^*\nabla\tilde{T}_1 - H_1\nabla\tilde{T}_1\nabla T_1 - H_1\nabla\tilde{T}_1\nabla T_1^* - R_1,$$
(2.57)

$$q_{1,1}^s = \tilde{\psi}_1 \quad, \quad \text{on } \partial\Omega.$$

Since

$$\|A_1\nabla\tilde{q}_0\| \leq h\bar{s}^2\|\tilde{q}_0\| \leq M^*$$

$$\|A_1\nabla q_0^*\| \leq h\bar{s}^2\|q_0^*\| \leq M^*$$

$$\|B_1\nabla\tilde{q}_0\| \leq 2h\bar{s}^2\|\tilde{q}_0\| \leq M^*$$

$$\|B_1\nabla q_0^*\| \leq 2h\bar{s}^2\|q_0^*\| \leq M^*$$

$$\|C_1\nabla T_1\| \leq 8\bar{s}^2\|T_1\| \leq M^*,$$

by Schauder theorem, we have

$$\|\tilde{q}_{1,1}\| \leq KM^*(16\eta). \tag{2.58}$$

Hence

$$\|q_{1,1}^s\| = \|\tilde{q}_{1,1} + q_1^*\| \leq \|\tilde{q}_{1,1}\| + \|q_1^*\| \leq KM^*(16\eta) + M^* \leq 2M^*. \tag{2.59}$$

Now we estimate $\tilde{q}_{1,k}$. Assume that

$$\|\tilde{q}_{1,k-1}\| \leq KM^*(16\eta) \quad \text{and} \quad \|q_{1,k-1}^s\| \leq 2M^*. \tag{2.60}$$

Set in equation (2.46) $n = k$ and subtract it from (2.35). We obtain

$$\Delta\tilde{q}_{1,k} - A_1\nabla\tilde{q}_{1,k}\nabla\tilde{q}_{1,k-1} - A_1\nabla\tilde{q}_{1,k}\nabla q_0^* - B_1\nabla\tilde{q}_{1,k}\nabla\tilde{q}_0 - B_1\nabla\tilde{q}_{1,k}\nabla q_0^* - C_1\nabla\tilde{q}_{1,k}\nabla T_1$$

$$= A_1\nabla q_1^*\nabla\tilde{q}_{1,k-1} + A_1\nabla q_1^*\nabla q_0^* - A_1\nabla q_1^*\nabla q_1^* + B_1\nabla q_1^*\nabla\tilde{q}_0 + C_1\nabla q_1^*\nabla\tilde{T}_1$$

$$+ D_1\Delta\tilde{q}_0 + E_1\Delta\tilde{T}_1 - F_1\nabla\tilde{q}_0\nabla\tilde{q}_0 - 2F_1\nabla\tilde{q}_0\nabla q_0^*$$

$$- G_1\nabla\tilde{q}_0\nabla T_1 - G_1\nabla q_0^*\nabla\tilde{T}_1 - H_1\nabla\tilde{T}_1\nabla T_1 - H_1\nabla\tilde{T}_1\nabla T_1^* - R_1. \tag{2.61}$$

$$q_{1,k}^s = \tilde{\psi}_1 \quad , \quad \text{on } \partial\Omega.$$

Since

$$\|A_1\nabla\tilde{q}_{1,k-1}\| \leq h\bar{s}^2\|\tilde{q}_{1,k-1}\| \leq M^*$$

$$\|A_1\nabla q_0^*\| \leq h\bar{s}^2\|q_0^*\| \leq M^*$$

$$\|B_1\nabla\tilde{q}_0\| \leq 2h\bar{s}^2\|\tilde{q}_0\| \leq M^*$$

$$\|B_1\nabla q_0^*\| \leq 2h\bar{s}^2\|q_0^*\| \leq M^*$$

$$\|C_1\nabla T_1\| \leq 8\bar{s}^2\|T_1\| \leq M^*,$$

by Schauder theorem, we have

$$\|\tilde{q}_{1,k}\| \leq KM^*(16\eta). \tag{2.62}$$

Hence

$$\|q_{1,k}^s\| = \|\tilde{q}_{1,k} + q_1^*\| \le \|\tilde{q}_{1,k}\| + \|q_1^*\| \le KM^*(16\eta) + M^* \le 2M^*. \tag{2.63}$$

And therefore we finally have

$$\|\tilde{q}_1\| \le KM^*(16\eta) \quad \text{and} \quad \|q_1^s\| \le 2M^*. \tag{2.64}$$

Now we estimate $\tilde{q}_{2,1}$. Set in equation (2.46) $n = 2$ and subtract it from (2.36) at $n = 2, k = 1$, recalling that $q_{2,0}^s = q_1^s$. We obtain

$$\Delta\tilde{q}_{2,1} - A_2\nabla\tilde{q}_{2,1}\nabla\tilde{q}_1 - A_2\nabla\tilde{q}_{2,1}\nabla q_1^* - B_2\nabla\tilde{q}_{2,1}\nabla\tilde{q}_1 - B_2\nabla\tilde{q}_{2,1}\nabla q_1^* - C_2\nabla\tilde{q}_{2,1}\nabla T_2$$

$$= A_2\nabla q_2^*\nabla\tilde{q}_1 + A_2\nabla q_2^*\nabla q_1^* - A_2\nabla q_2^*\nabla q_2^* + B_2\nabla q_2^*\nabla\tilde{q}_1 + C_2\nabla q_2^*\nabla\tilde{T}_2$$

$$+ D_2\Delta\tilde{q}_1 + E_2\Delta\tilde{T}_2 - F_2\nabla\tilde{q}_1\nabla\tilde{q}_1 - 2F_2\nabla\tilde{q}_1\nabla q_1^*$$

$$- G_2\nabla\tilde{q}_1\nabla T_2 - G_2\nabla q_1^*\nabla\tilde{T}_2 - H_2\nabla\tilde{T}_2\nabla T_2 - H_2\nabla\tilde{T}_2\nabla T_2^* - R_2, \tag{2.65}$$

$$q_{2,1}^s = \tilde{\psi}_2 \quad , \quad \text{on } \partial\Omega.$$

Since

$$\|A_2\nabla\tilde{q}_1\| \le h\bar{s}^2\|\tilde{q}_{1,k-1}\| \le M^*$$

$$\|A_2\nabla q_1^*\| \le h\bar{s}^2\|q_1^*\| \le M^*$$

$$\|B_2\nabla\tilde{q}_1\| \le 2h\bar{s}^2\|\tilde{q}_1\| \le M^*$$

$$\|B_2\nabla q_1^*\| \le 2h\bar{s}^2\|q_1^*\| \le M^*$$

$$\|C_2\nabla T_2\| \le 4\bar{s}^2\|T_2\| \le 4\bar{s}^2\big[Nh \cdot KM^*(16\eta) + \max_{0\le j\le 1}\|q_j^*\| + \xi\big]$$

$$\le 4\bar{s}^2\big[\eta + \max_{0\le j\le 1}\|q_j^*\| + \xi\big] \le M^*,$$

by Schauder theorem, we have

$$\|\tilde{q}_{2,1}\| \le KM^*(20\eta). \tag{2.66}$$

Hence

$$\|q_{2,1}^s\| = \|\tilde{q}_{2,1} + q_2^*\| \le \|\tilde{q}_{2,1}\| + \|q_2^*\| \le KM^*(20\eta) + M^* \le 2M^*. \qquad (2.67)$$

Now we estimate $\tilde{q}_{2,k}$. Assume that

$$\|\tilde{q}_{2,k-1}\| \le KM^*(16\eta) \quad \text{and} \quad \|q_{2,k-1}^s\| \le 2M^*. \qquad (2.68)$$

Set in equation (2.46) $n = 2$ and subtract it from (2.36) at $n = 2$. We obtain

$$\Delta\tilde{q}_{2,k} - A_2\nabla\tilde{q}_{2,k}\nabla\tilde{q}_{2,k-1} - A_2\nabla\tilde{q}_{2,k}\nabla q_1^* - B_2\nabla\tilde{q}_{2,k}\nabla\tilde{q}_1 - B_2\nabla\tilde{q}_{2,k}\nabla q_1^* - C_2\nabla\tilde{q}_{2,k}\nabla T_2$$

$$= A_2\nabla q_2^*\nabla\tilde{q}_{2,k-1} + A_2\nabla q_2^*\nabla q_1^* - A_2\nabla q_2^*\nabla q_2^* + B_2\nabla q_2^*\nabla\tilde{q}_1 + C_2\nabla q_2^*\nabla\tilde{T}_2$$

$$+ D_2\Delta\tilde{q}_1 + E_2\Delta\tilde{T}_2 - F_2\nabla\tilde{q}_1\nabla\tilde{q}_1 - 2F_2\nabla\tilde{q}_1\nabla q_1^*$$

$$- G_2\nabla\tilde{q}_1\nabla T_2 - G_2\nabla q_1^*\nabla\tilde{T}_2 - H_2\nabla\tilde{T}_2\nabla T_2 - H_2\nabla\tilde{T}_2\nabla T_2^* - R_2, \qquad (2.69)$$

$$q_{2,k}^s = \tilde{\psi}_2 \quad , \quad \text{on } \partial\Omega.$$

Since

$$\|A_2\nabla\tilde{q}_{2,k-1}\| \le h\bar{s}^2\|\tilde{q}_{1,k-1}\| \le M^*$$

$$\|A_2\nabla q_1^*\| \le h\bar{s}^2\|q_1^*\| \le M^*$$

$$\|B_2\nabla\tilde{q}_1\| \le 2h\bar{s}^2\|\tilde{q}_1\| \le M^*$$

$$\|B_2\nabla q_1^*\| \le 2h\bar{s}^2\|q_1^*\| \le M^*$$

$$\|C_2\nabla T_2\| \le 4\bar{s}^2\|T_2\| \le 4\bar{s}^2\left[Nh \cdot KM^*(16\eta) + \max_{0\le j\le 1}\|q_j^*\| + \xi\right]$$

$$\le 4\bar{s}^2\left[\eta + \max_{0\le j\le 1}\|q_j^*\| + \xi\right] \le M^*,$$

by Schauder theorem, we have

$$\|\tilde{q}_{2,k}\| \le KM^*(20\eta). \qquad (2.70)$$

Hence

$$\|q_{2,k}^s\| = \|\tilde{q}_{2,k} + q_2^*\| \leq \|\tilde{q}_{2,k}\| + \|q_2^*\| \leq KM^*(20\eta) + M^* \leq 2M^*. \qquad (2.71)$$

And therefore we finally have

$$\|\tilde{q}_2\| \leq KM^*(20\eta) \quad \text{and} \quad \|q_2^s\| \leq 2M^*. \qquad (2.72)$$

We now estimate the function $\tilde{q}_{n,k}$. Assume that

$$\|\tilde{q}_{n-1}\| \leq KM^*(20\eta) \quad , \quad \|q_{n-1}^s\| \leq 2M^* \qquad (2.73)$$

and

$$\|\tilde{q}_{n,k-1}\| \leq KM^*(20\eta) \quad , \quad \|q_{n,k-1}^s\| \leq 2M^*. \qquad (2.74)$$

Subtract equation (2.46) from (2.36), we obtain

$$\Delta\tilde{q}_{n,k} - A_n\nabla\tilde{q}_{n,k}\nabla\tilde{q}_{n,k-1} - A_n\nabla\tilde{q}_{n,k}\nabla q_{n-1}^* - B_n\nabla\tilde{q}_{n,k}\nabla\tilde{q}_{n-1} - B_n\nabla\tilde{q}_{n,k}\nabla q_{n-1}^* - C_n\nabla\tilde{q}_{n,k}\nabla T_n$$

$$= A_n\nabla q_n^*\nabla\tilde{q}_{n,k-1} + A_n\nabla q_n^*\nabla q_{n-1}^* - A_n\nabla q_n^*\nabla q_n^* + B_n\nabla q_n^*\nabla\tilde{q}_{n-1} + C_n\nabla q_n^*\nabla\tilde{T}_n$$

$$+ D_n\Delta\tilde{q}_{n-1} + E_n\Delta\tilde{T}_n - F_n\nabla\tilde{q}_{n-1}\nabla\tilde{q}_{n-1} - 2F_n\nabla\tilde{q}_{n-1}\nabla q_{n-1}^*$$

$$- G_n\nabla\tilde{q}_{n-1}\nabla T_n - G_n\nabla q_{n-1}^*\nabla\tilde{T}_n - H_n\nabla\tilde{T}_n\nabla T_n - H_n\nabla\tilde{T}_n\nabla T_n^* - R_n, \qquad (2.75)$$

$$q_{n,k}^s = \tilde{\psi}_n \quad , \quad \text{on } \partial\Omega.$$

Since

$$\|A_n\nabla\tilde{q}_{n,k-1}\| \leq h\bar{s}^2\|\tilde{q}_{n,k-1}\| \leq M^*$$

$$\|A_n\nabla q_{n-1}^*\| \leq h\bar{s}^2\|q_{n-1}^*\| \leq M^*$$

$$\|B_n\nabla\tilde{q}_{n-1}\| \leq 2h\bar{s}^2\|\tilde{q}_{n-1}\| \leq M^*$$

$$\|B_n\nabla q_{n-1}^*\| \leq 2h\bar{s}^2\|q_{n-1}^*\| \leq M^*$$

$$\|C_n\nabla T_n\| \leq 4\bar{s}^2\|T_n\| \leq 4\bar{s}^2\Big[Nh\cdot KM^*(16\eta) + \max_{0\leq j\leq n-1}\|q_j^*\| + \xi\Big]$$

$$\leq 4\bar{s}^2\Big[\eta + \max_{0\leq j\leq n-1}\|q_j^*\| + \xi\Big] \leq M^*,$$

by Schauder theorem, we have

$$\|\tilde{q}_{n,k}\| \leq KM^*(20\eta).$$

(2.76)

Hence

$$\|q_{n,k}^s\| = \|\tilde{q}_{n,k} + q_n^*\| \leq \|\tilde{q}_{n,k}\| + \|q_n^*\| \leq KM^*(20\eta) + M^* \leq 2M^*.$$

(2.77)

And therefore we finally have

$$\|\tilde{q}_n\| \leq KM^*(20\eta) \quad \text{and} \quad \|q_n^s\| \leq 2M^*.$$

(2.78)

Estimates (2.78) completes the proof of this theorem. $\square$

CHAPTER 3

NUMERICAL METHODS

3.1 Introduction

This chapter presents the numerical method of our simulation. According to the inverse problem in subsection 1.2.1, the boundary condition $w(\boldsymbol{x}, \boldsymbol{x}_0) = \varphi(\boldsymbol{x}, \boldsymbol{x}_0)$ for all $\boldsymbol{x} \in \partial\Omega$ is required to solve equation (1.1). These boundary data will be obtained from the measurement at the boundary of $\partial\Omega$ by the CCD Camera, CCD stands for a "Charge-Coupled Device", where measurement data contains a noise influence. We had presented a technique to filter these noise component by using least-square polynomial [6][7][8]. In this paper we purpose an alternative way of filtering noise on boundary, this idea is taken from our publication [8]. The technique is similar to the conversion of of the arbitrary shape domain to a rectangular domain and solving equation (1.1), (1.2) on rectangular domain, so called *computation* domain for the inverse problem. The equation and its boundary data for the latter conversion is named the "exterior forward problem". By employing this technique, we slightly modify the inverse problem and make the whole process correspond to the mathematical model in chapter 2. The new *inverse problem* is

Denote $\boldsymbol{x} = (x, y)$. Let $\mathcal{A} \subset \mathbb{R}^2$ be a bounded domain and $\Gamma = \partial\mathcal{A}$. Let B be a constant. Determine the coefficient $a(\boldsymbol{x})$ in equation (2.1) for $\boldsymbol{x} \in \mathcal{A}$, assuming that the following function $\tilde{\varphi}(\boldsymbol{x}, s)$ is given

$$w(\boldsymbol{x}, s) = \tilde{\varphi}(\boldsymbol{x}, s), \qquad \forall \boldsymbol{x} \in \Gamma, \quad \forall s \in [\underline{s}, \overline{s}], \tag{3.1}$$

33

where $\bar{s}$ is a sufficient large number, $\underline{s} < \bar{s}$ is a certain fixed number and

$$\{\boldsymbol{x}_0 \in (s, B), s \geq \underline{s}\} \cap \overline{\mathcal{A}} = \varnothing \,.$$

The domain of interest is no longer Ω domain, see figure 3.1. The difference is in Ω domain after applying the exterior forward problem. To clarify, the inverse problem in subsection 1.2.1 is still present but we will now solve the inverse problem using the result of the exterior forward problem. Hence, the boundary data $w(\boldsymbol{x}, \boldsymbol{x}_0) = \varphi(\boldsymbol{x}, \boldsymbol{x}_0)$ on $\partial\Omega$ in the inverse problem of subsection 1.2.1 is not from the measurement directly but it is from the exterior forward problem base on the measurement. By applying this technique, the computation with noisy data on $\partial\mathcal{A}$ will provide a smooth and continuous data on $\partial\Omega$, detail in subsection 3.3.1 and see its scheme in figure 3.2. Such a method is analogous to the matching fluid in experiments.

The simulation process includes five steps:

(i) *Generating measurement data*: We obtain our simulated measurement data by solving the forward problem of equation (1.1), (1.2) in Ω_0 domain with known $a(\boldsymbol{x})$. This Ω_0 domain is a rectangular domain satisfying $\Omega_0 \supset \Omega \supset \mathcal{A}$. The reason for considering the rectangular Ω_0 along with the rectangular Ω and $\mathcal{A}$ is that it is natural to approximate the solution of the problem (1.1), (1.2) in the infinite domain by the solution of equation, (1.1) in Ω_0 with Robin boundary conditions at $\partial\Omega_0$. We have established numerically that for the range of parameters we use, the solution of (1.1), (1.2) is close in $\mathcal{A}$ to the solution of equation (1.1) in the bigger rectangle Ω_0 with the Robin boundary conditions at its sides. Figure 3.1 illustrates rectangular Ω_0 ,Ω and $\mathcal{A}$.

(ii) *Filtering measurement data*: After the forward problem of equation (1.1), (1.2) in Ω_0 is solved, we assign the measurement data plus noise on $\partial\mathcal{A}$. Figure 3.1 shows the domain of interest $\mathcal{A}$. Then we solve the exterior forward problem in $\Omega_0 - \mathcal{A}$
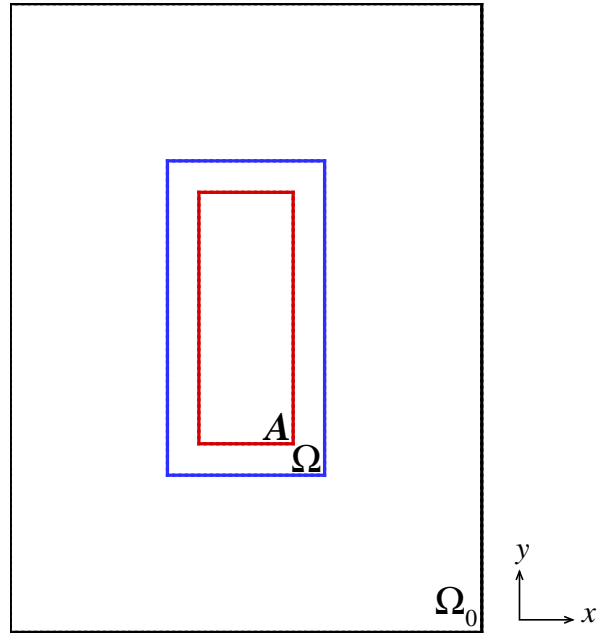
Figure 3.1. Three domains layout.

with the Robin boundary condition on $\partial\Omega_0$ and Dirichlet condition on $\partial\mathcal{A}$. Function $a(\boldsymbol{x})$ in $\Omega_0 - \mathcal{A}$ is set to the background value k^2.

(iii) *Computing the tail function*: The tail function in this paper is slightly changed from [6][7][8]. The tail function is considered to be a crucial in our numerical computation, our design in such the tail function is more precise. The four side tail version is introduced in this paper. The idea of the four side tail function is to average of tail functions from (1) the original tail function (angle#1) as in [6][7][8] and (2) additional tail functions (angle#2, #3 and #4), see figure 3.5 for the location of light source.

(iv) *Numerical Layer stripping*: This computation is directly related to our layer stripping in section 2.2. Since the convergence of this technique has been proved for

$q_n^s(\boldsymbol{x})$ for all $s \in [s_n, s_{n-1})$. In the numerical method we set $s = s_n$, this makes $q_n^s(\boldsymbol{x}) = q_n(\boldsymbol{x})$ and equation (2.29) becomes simpler. The first s-derivatives function (2.17), for computing q_n, are on the boundary $\partial\Omega$ since it is our basic computation domain for inverse problem. Subsection 3.3.1 describes how these values are obtained.

(v) *Backward substitution*: This is also related to subsection 2.2.2, the purpose is to obtain the target coefficient $a(\boldsymbol{x})$.

The details of the fives step above are explained in the following section.

3.2 Generating Measurement Data with the Forward Problem

The simulated measurement data on the boundary of $\partial\mathcal{A}$ is generated using equation (2.1). We numerically compute the "forward problem" of equation (2.1) with condition (2.2) on Ω_0 using the finite element method (FEM) where the Robin boundary condition $\vec{n} \cdot \nabla w(\boldsymbol{x}, s) + w(\boldsymbol{x}, s) = 0$ is applied on $\partial\Omega_0$. The solution of (2.1) on Ω_0 is computed with the known $a(\boldsymbol{x})$. This $a(\boldsymbol{x})$ function represent the required coefficient what is needed to perform the reconstruction stage in the inverse problem. In fact, the measurement data is obtained from the CCD camera where $a(\boldsymbol{x})$ is unknown. Hence the presence of $a(\boldsymbol{x})$ in our forward problem is just for the simulation purpose. We assume that in our inverse problem, $a(\boldsymbol{x})$ is still unknown.

This known $a(\boldsymbol{x})$ plays an important role in giving an example of cofficient μ_s' and μ_a that we need to perform the reconstruction. In chapter 4, we evaluate some examples of these coefficient as we discussed in section 1.3.

For each light source $s = (B, s)$, we solve equation (2.1) using *Weak Formulation* of FEM. Let η be the test function. Multipling both side of equation (2.1) by η and integrating over Ω_0 gives

$$\int_{\Omega_0} \eta \Delta w \, d\boldsymbol{x} - \int_{\Omega_0} \eta a w \, d\boldsymbol{x} = - \int_{\Omega_0} \eta \delta \, d\boldsymbol{x} \qquad (3.2)$$

or

$$\int_{\partial\Omega_0} \eta(\vec{n}\cdot\nabla w)\,d\boldsymbol{x} - \int_{\Omega_0} \nabla\eta\cdot\nabla w\,d\boldsymbol{x} - \int_{\Omega_0} \eta a w\,d\boldsymbol{x} = -\int_{\Omega_0} \eta\delta\,d\boldsymbol{x} \qquad (3.3)$$

With the Robin boundary condition $\vec{n}\cdot\nabla w(\boldsymbol{x},s) + w(\boldsymbol{x},s) = 0$ then we have $\vec{n}\cdot\nabla w = -w(\boldsymbol{x},s)$ on $\partial\Omega_0$. We then numerically solve weak form of the following equation

$$\int_{\partial\Omega_0} \eta w\,d\boldsymbol{x} + \int_{\Omega_0} \nabla\eta\cdot\nabla w\,d\boldsymbol{x} + \int_{\Omega_0} \eta a w\,d\boldsymbol{x} = \int_{\Omega_0} \eta\delta\,d\boldsymbol{x}. \qquad (3.4)$$

for each light source s.

After the solution $w(\boldsymbol{x},s)$ on Ω_0 are computed, we can extract the boundary data of $\mathcal{A}$ to be our simulated measurement data for each light source s. We introduce the random noise as the random process with respect to the detector locations, this noise is added to the extracted data on $\partial\mathcal{A}$. Let $\bar{\varphi}(\boldsymbol{x},s)$ be the extracted data on $\partial\mathcal{A}$. We compute $\widetilde{\varphi}(\boldsymbol{x},s) = \bar{\varphi}(\boldsymbol{x},s)[1+\chi(\boldsymbol{x})]$ on $\partial\mathcal{A}$ where $\chi(\boldsymbol{x})$ is the random variable, which we introduce as $\chi = 0.02W$, where W is a white noise with the equal distribution at $[-1,1]$. Hence, $\widetilde{\varphi}(\boldsymbol{x},s)$ represents the 2% multiplicative random noise on $\partial\mathcal{A}$. We will use this boundary data with noise as simulated data in our inverse problem.

3.3   Reconstruction of the Coefficient $a(\boldsymbol{x})$ from Measurement Data

The reconstruction of the coefficient $a(\boldsymbol{x})$, the inverse problem, employed the algorithm so-called layer stripping which was mentioned in section 2.2. In section 3.2, Ω domain is mentioned as the computation domain, its boundary data on Ω domain is not the actual measurement from the CCD camera, it is obtained via the exterior forward problem for pre-processing the noise in measurement data on $\partial\mathcal{A}$. After we obtain the boundary on Ω domain we compute the tail function, subsection 3.3.2. We then compute the layer stripping, subsection 3.3.3, and the target coefficient $a(\boldsymbol{x})$ is the result of applying the backward substitution, subsection 3.3.4.
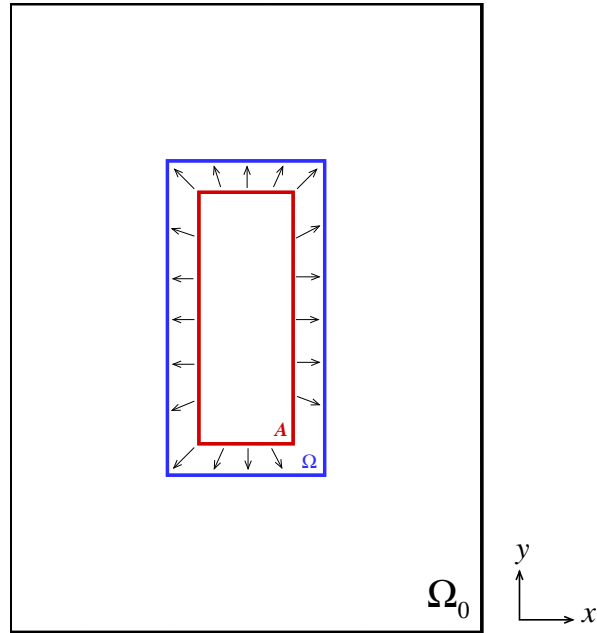
Figure 3.2. Exterior forward problem scheme.

3.3.1 Filtering Measurement Data

The regularization method which was introduced in this paper to pre-process the noise in measurement data differs from the one we used in [6][7][8]. Our technique employs the property of the diffusion equation that gives the smooth and continuous solution within the domain of computation. Hence by computing (2.1) on $\Omega_0 - \mathcal{A}$ with $w(\boldsymbol{x}, s) = \widetilde{\varphi}(\boldsymbol{x}, s)$ on $\mathcal{A}$ (interior boundary of $\Omega_0 - \mathcal{A}$) and the Robin condition $\vec{n} \cdot \nabla w(\boldsymbol{x}, s) + w(\boldsymbol{x}, s) = 0$ on $\partial \Omega_0$ (exterior boundary of $\Omega_0 - \mathcal{A}$) will give a smooth and continuous data on $\partial \Omega$, see figure 3.2.

Recall that the full forward problem for equation (2.1) is for the entire domain Ω_0. Figure 3.3(a) shows the solution of the forward problem (2.1) which was done to obtain the "measurement data" on $\mathcal{A}$ in the numerical experiment. Note that in a
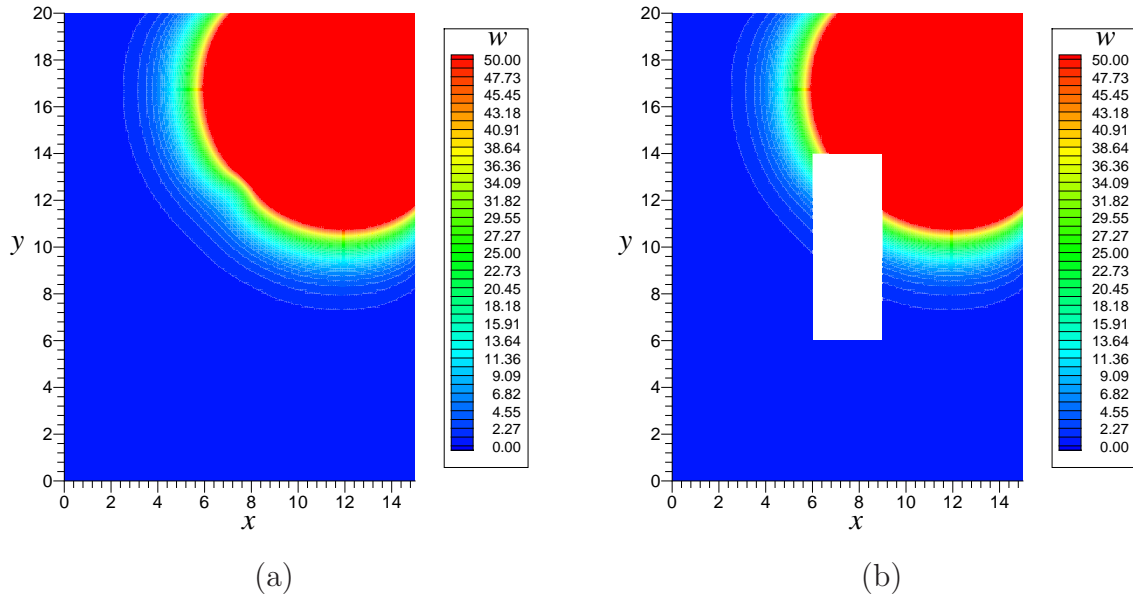
Figure 3.3. The forward problem solution shows no visible difference on $\Omega_0 - \mathcal{A}$ between the solution of the full forward problem (a) and the solution extrapolated from the boundary-value data at $\partial\mathcal{A}$ via an exterior forward problem (b).

real application, the solution to the full forward problem is not available. The data on $\mathcal{A}$ can only be obtained from measurement. But in both the numerical experiment and the real application, the exterior forward problem of equation (2.1) can be solved to obtain a numerical solution in domain $\Omega_0 - \mathcal{A}$, figure 3.3(b) displays this solution. The approximation error of the solution of the exterior forward problem against the full forward problem on $\partial\Omega$ can be found in subsection 4.1.6. A very good agreement of those two solution is found comparing the two results on $\partial\Omega$, indicating that solving the exterior forward problem is a precise and stable way to filter the measurement data to the computational domain Ω.

For the exterior forward problem, we solve (2.1) on $\Omega_0 - \mathcal{A}$ with the boundary condition as mentioned above. The weak form of exterior problem is slightly different

from (3.4). Let η be the test function. Multiplying both side of equation (2.1) by η and integrating over $\Omega_0 - \mathcal{A}$ give

$$\int_{\Omega_0-\mathcal{A}} \eta \Delta w \, d\boldsymbol{x} - \int_{\Omega_0-\mathcal{A}} \eta a w \, d\boldsymbol{x} = -\int_{\Omega_0-\mathcal{A}} \eta \delta \, d\boldsymbol{x}$$

or

$$\int_{\partial(\Omega_0-\mathcal{A})} \eta(\vec{n} \cdot \nabla w) \, d\boldsymbol{x} - \int_{\Omega_0-\mathcal{A}} \nabla \eta \cdot \nabla w \, d\boldsymbol{x} - \int_{\Omega_0-\mathcal{A}} \eta a w \, d\boldsymbol{x} = -\int_{\Omega_0-\mathcal{A}} \eta \delta \, d\boldsymbol{x}.$$

Since $\vec{n} \cdot \nabla w = -w$ on $\partial\Omega_0$ and the Dirichlet boundary condition is imposed on $\partial\mathcal{A}$. We then numerically solve the weak form of the following equation

$$\int_{\partial\Omega_0} \eta w \, d\boldsymbol{x} + \int_{\Omega_0-\mathcal{A}} \nabla \eta \cdot \nabla w \, d\boldsymbol{x} + \int_{\Omega_0-\mathcal{A}} \eta a w \, d\boldsymbol{x} = \int_{\Omega_0-\mathcal{A}} \eta \delta \, d\boldsymbol{x}. \qquad (3.5)$$

by imposing the Dirichlet condition on $\partial\mathcal{A}$ for each light source s.

Once the filtering process is complete, let $\varphi(\boldsymbol{x}, s)$ be the boundary value of $\partial\Omega$. This boundary value is used to compute the tail function and compute the layer stripping procedure where the first s-derivatives, see (2.17), are processed on $\partial\Omega$ by the formula

$$\psi_n(\boldsymbol{x}) = \frac{1}{s_n^2} \left(\frac{\ln \varphi_{n+1}(\boldsymbol{x}) - \ln \varphi_n(\boldsymbol{x})}{s_{n+1} - s_n} \right) \qquad (3.6)$$

where $n = 0, 1, 2, 3$ and $\varphi_n(\boldsymbol{x}) = \varphi(\boldsymbol{x}, s_n)$, $n = 0, \dots, 3$ are the boundary value of Ω.

3.3.2   Computing the Tail Function

A crucial part of our problem is finding a good quality approximation of the tail-function $u(\boldsymbol{x}, \bar{s})$. In our case, however, the free parameter s in (B, s) is the location of the light source. For real world applications, the source location cannot be very far from the domain of interest, this is due to both the restriction in size and the limit of the light intensity. We have undertaken to understand the behavior of solutions when the location of light sources moves at realistic scales.
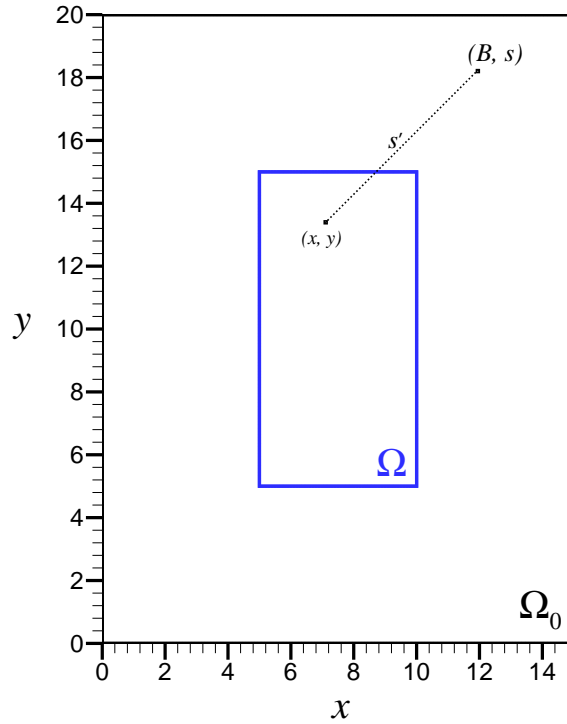
Figure 3.4. Distance of light source $s' = |(x - B, y - s)|$.

3.3.2.1 The Mathematical Model of Tail

First, we consider the fundamental solution of the 2D diffusion equation for the case $a(\boldsymbol{x}) \equiv k^2$ where k^2 is background value of our domain, or we simply say the case with no inclusions in domain Ω. This solution is

$$\widetilde{w}_0(\boldsymbol{x}, s) = \frac{1}{2\pi} K_0(ks') \tag{3.7}$$

where K_0 is a modified Bessel function and $s' = |(x - B, y - s)|$, see figure 3.4. Its asymptotic behaviors is

$$K_0(ks') = \sqrt{\frac{\pi}{2s'}} e^{-ks'} \left[1 + O(\frac{1}{s'})\right] \quad , \ s' \to \infty. \tag{3.8}$$

Represent solution of equation (2.4) with

$$w(\boldsymbol{x}, s) = \widetilde{w}_0(\boldsymbol{x}, s) + W(\boldsymbol{x}, s). \tag{3.9}$$

Since $\widetilde{w}_0$ satisfies $\Delta\widetilde{w}_0 - k^2\widetilde{w}_0 = 0$ in Ω, then equation (2.4) becomes

$$\Delta W - [a(\boldsymbol{x}) - k^2]\widetilde{w}_0 - [a(\boldsymbol{x}) - k^2]W - k^2 W = 0. \tag{3.10}$$

Therefore we have

$$\Delta W - k^2 W = [a(\boldsymbol{x}) - k^2]w. \tag{3.11}$$

This is the *Inhomogeneous Helmholtz* equation where the solution can be written as follows

$$W(\boldsymbol{x}, s) = -\frac{1}{2\pi} \int_\Omega K_0\left(k|\boldsymbol{x} - \xi|\right) [a(\xi) - k^2]w(\xi, s)\, d\xi. \tag{3.12}$$

Substituting equation (3.12) into equation (3.9), the solution of equation (2.4) becomes the following integral equation

$$w(\boldsymbol{x}, s) = \widetilde{w}_0(\boldsymbol{x}, s) - \frac{1}{2\pi} \int_\Omega K_0\left(k|\boldsymbol{x} - \xi|\right) [a(\xi) - k^2]w(\xi, s)\, d\xi. \tag{3.13}$$

We introduce the function

$$\overline{W}(\boldsymbol{x}, s) = 2\sqrt{2\pi s'}e^{ks'}w(\boldsymbol{x}, s). \tag{3.14}$$

Hence, multiplication of $\sqrt{s'}e^{ks'}$ to equation (3.13) gives

$$\overline{W}(\boldsymbol{x}, s) = \left[1 + O(\frac{1}{s'})\right] - \frac{1}{2\pi} \int_\Omega K_0\left(c|\boldsymbol{x} - \xi|\right) [a(\xi) - k^2] \frac{2\sqrt{2\pi s'}e^{ks'}}{2\sqrt{2\pi\widetilde{s}}e^{k\widetilde{s}}} \overline{W}(\xi, s)\, d\xi, \tag{3.15}$$

where $\widetilde{s} = |\xi - s|$, $s = (B, s)$. From equation (3.15), we have the asymptotic term

$$\frac{\sqrt{s'}e^{ks'}}{\sqrt{\widetilde{s}}e^{k\widetilde{s}}} \to 1 \quad \text{as} \quad s \to \infty.$$

Therefore $\overline{W}$ has a unique solution decaying at infinity, and equation (3.15) becomes

$$\overline{W}(\boldsymbol{x}, s) = 1 + \widetilde{g}(\boldsymbol{x}) + O(\frac{1}{s'}) \quad , \text{ as } s' \to \infty. \tag{3.16}$$

Another form of equation (3.16) based on equation (3.14) is the asymptotic behavior of w as $s' \to \infty$

$$w(\boldsymbol{x}, s) = \frac{e^{-ks'}}{2\sqrt{2\pi s'}}(1 + \tilde{g}(\boldsymbol{x}) + O(\frac{1}{s'})) \quad , \text{ as } s' \to \infty. \tag{3.17}$$

The function $\tilde{g}(\boldsymbol{x})$ is unknown and is independent of s'. Since we are interested in the function $u = \ln w$, we have

$$u(\boldsymbol{x}, s) = -ks' - \ln 2\sqrt{2\pi} - \frac{1}{2}\ln s' + g(\boldsymbol{x}) + O(\frac{1}{s'}) \quad , \text{ as } s' \to \infty, \tag{3.18}$$

where $g(\boldsymbol{x})$ is also independent of s'. If we can approximate $g(\boldsymbol{x})$ we can also approximate $u(\boldsymbol{x}, s)$ and hence $v(\boldsymbol{x}, s)$. Since function $u(\boldsymbol{x}, s)$ can be obtained only at the boundary, no information of $u(\boldsymbol{x}, s)$ within the interior of Ω, we will explain the heuristic approach of approximation $g(\boldsymbol{x})$ with the incomplete $u(\boldsymbol{x}, s)$ in next section.

3.3.2.2 The First Guess of Tail

We approximate the unknown tail function by four different angles, figure 3.5, and the final approximation is the average of four. The four different angles are denoted by the location of light sources, where we put the sets of light source in four different locations. The first location is called angle#1 there are $N+1$ light sources in total, number N are corresponding to the subintervals (2.18), where $M < N+1$ light sources are used for construct $u^{(1)}$, see below. For angle#2, angle#3 and angle#4, the number of light sources are all equal to M, these are used to construct $u^{(2)}$, $u^{(3)}$ and $u^{(4)}$, respectively. Angle#1, angle#2, angle#3 and angle#4 are located at the top-right, bottom-right, top-left and bottom-left of Ω domain.

For the approximation of tail function, the term $-ks' - \ln 2\sqrt{2\pi} - \frac{1}{2}\ln s' + O(\frac{1}{s'})$ in (3.18) is the natural log of the fundamental solution

$$\ln \tilde{w}_0(\boldsymbol{x}, s) = \ln \frac{1}{2\pi}\sqrt{\frac{\pi}{2s'}}e^{-ks'}\left[1 + O(\frac{1}{s'})\right]$$
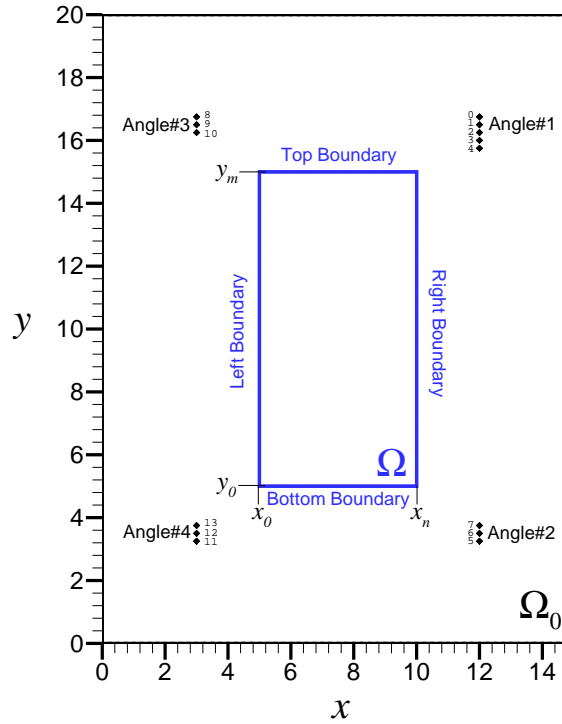
Figure 3.5. Four different angles denoted by light sources.

where the term k^2 is the background value. By numerical method we can get this fundamental solution by computing the forward problem on Ω_0 without inclusions (only background value). Hence in the computation of the first guess of tail, we replace those term by the latter forward solution. With this scheme, we modify equation (3.18) to

$$u(\boldsymbol{x}, s) = \ln w(\boldsymbol{x}, s) = \ln \tilde{w}_0(\boldsymbol{x}, s) + g(\boldsymbol{x}). \tag{3.19}$$

The approximation procedure for finding the first guess of tail , $\bar{u}_0(\boldsymbol{x})$, follows the following steps:

(i) Compute $g^{(n)}$, $n = 1, 2, 3, 4$, in Ω which represent four different functions $g(\boldsymbol{x})$ of each angle. We compute them as follows, see figure 3.5.

– For $g^{(1)}$, we use the left boundary of $\partial\Omega$ where $x = x_0$ for s_i, $i = 0, 1, \ldots, M - 1$. This boundary data is known for all y, that is $w(x_0, y, s_i) = \varphi(x_0, y, s_i)$ is known for all i. The function $g_i^{(1)}(x_0, y)$ is computed as follows

$$g_i^{(1)}(x_0, y) = \ln w(x_0, y, s_i) - \ln \tilde{w}_0(x_0, y, s_i).$$

Then the final $g^{(1)}(x_0, y)$ is computed by

$$g^{(1)}(x_0, y) = \frac{1}{M} \sum_{j=0}^{M-1} g_i^{(1)}(x_0, y).$$

We then use the bottom boundary of $\partial\Omega$ where $y = y_0$ for s_i, $i = 0, 1, \ldots, M - 1$. This boundary data is known for all x, that is $w(x, y_0, s_i) = \varphi(x, y_0, s_i)$ is known for all i. The function $g_i^{(1)}(x_0, y)$ is computed as follows

$$g_i^{(1)}(x, y_0) = \ln w(x, y_0, s_i) - \ln \tilde{w}_0(x, y_0, s_i).$$

Then the final $g^{(1)}(x_0, y)$ is computed by

$$g^{(1)}(x, y_0) = \frac{1}{M} \sum_{j=0}^{M-1} g_i^{(1)}(x, y_0).$$

The required function $g^{(1)}$ is computed by

$$g^{(1)}(\boldsymbol{x}) = \frac{1}{2} \left[g^{(1)}(x_0, y) + g^{(1)}(x, y_0) \right] \quad , \quad \text{where } \boldsymbol{x} \in \Omega. \tag{3.20}$$

– For $g^{(2)}$, we use the left boundary of $\partial\Omega$ where $x = x_0$ for s_i, $i = N, N + 1, \ldots, N + M - 1$. This boundary data is known for all y that is $w(x_0, y, s_i) = \varphi(x_0, y, s_i)$ is known for all i. The function $g_i^{(2)}(x_0, y)$ is computed as follows

$$g_i^{(2)}(x_0, y) = \ln w(x_0, y, s_i) - \ln \tilde{w}_0(x_0, y, s_i).$$

Then the final $g^{(2)}(x_0, y)$ is computed by

$$g^{(2)}(x_0, y) = \frac{1}{M} \sum_{j=N}^{N+M-1} g_i^{(2)}(x_0, y).$$

We then use the top boundary of $\partial\Omega$ where $y = y_m$ for s_i, $i = N, N+1, \ldots, N+M-1$. This boundary data is known for all x that is $w(x, y_m, s_i) = w(x, y_m, s_i)$ is known for all i. The function $g_i^{(2)}(x, y_m)$ is computed as follows

$$g_i^{(2)}(x, y_m) = \ln w(x, y_m, s_i) - \ln \tilde{w}_0(x, y_m, s_i).$$

Then the final $g^{(2)}(x_0, y)$ is computed by

$$g^{(2)}(x, y_m) = \frac{1}{M} \sum_{j=N}^{N+M-1} g_i^{(2)}(x, y_m).$$

The required function $g^{(2)}$ is computed by

$$g^{(2)}(\boldsymbol{x}) = \frac{1}{2} \left[g^{(2)}(x_0, y) + g^{(2)}(x, y_m) \right] \quad , \quad \text{where } \boldsymbol{x} \in \Omega. \tag{3.21}$$

– For $g^{(3)}$, we use the right boundary of $\partial\Omega$ where $x = x_n$ for s_i, $i = N + M, N + M + 1, \ldots, N + 2M - 1$. This boundary data is known for all y that is $w(x_n, y, s_i) = \varphi(x_n, y, s_i)$ is known for all i. The function $g_i^{(3)}(x_n, y)$ is computed as follows

$$g_i^{(3)}(x_n, y) = \ln w(x_n, y, s_i) - \ln \tilde{w}_0(x_n, y, s_i).$$

Then the final $g^{(3)}(x_n, y)$ is computed by

$$g^{(3)}(x_n, y) = \frac{1}{M} \sum_{j=N+M}^{N+2M-1} g_i^{(3)}(x_n, y).$$

We then use the bottom boundary of $\partial\Omega$ where $y = y_0$ for s_i, $i = N + M, N + M + 1, \ldots, N + 2M - 1$. This boundary data is known for all x that is $w(x, y_0, s_i) = \varphi(x, y_0, s_i)$ is known for all i. The function $g_i^{(3)}(x_n, y)$ is computed as follows

$$g_i^{(3)}(x, y_0) = \ln w(x, y_0, s_i) - \ln \tilde{w}_0(x, y_0, s_i).$$

Then the final $g^{(3)}(x_n, y)$ is computed by

$$g^{(3)}(x, y_0) = \frac{1}{M} \sum_{j=N+M}^{N+2M-1} g_i^{(3)}(x, y_0).$$

The required function $g^{(3)}$ is computed by

$$g^{(3)}(\boldsymbol{x}) = \frac{1}{2}\left[g^{(3)}(x_n, y) + g^{(3)}(x, y_0)\right] \quad , \quad \text{where } \boldsymbol{x} \in \Omega. \tag{3.22}$$

    − For $g^{(4)}$, we use the left boundary of $\partial\Omega$ where $x = x_n$ for s_i, $i = N + 2M, N + 2M + 1, \ldots, N + 3M - 1$. This boundary data is known for all y that is $w(x_n, y, s_i) = \varphi(x_n, y, s_i)$ is known for all i. The function $g_i^{(4)}(x_n, y)$ is computed as follows

$$g_i^{(4)}(x_n, y) = \ln w(x_n, y, s_i) - \ln \tilde{w}_0(x_n, y, s_i).$$

Then the final $g^{(4)}(x_n, y)$ is computed by

$$g^{(4)}(x_n, y) = \frac{1}{M} \sum_{j=N+2M}^{N+3M-1} g_i^{(4)}(x_n, y).$$

We then use the top boundary of $\partial\Omega$ where $y = y_m$ for s_i, $i = N, N+2M+1, \ldots, N+ 3M-1$. This boundary data is known for all x that is $w(\boldsymbol{x}, s_i) = \varphi(x, y_m, s_i)$ is known for all i. The function $g_i^{(4)}(x, y_m)$ is computed as follows

$$g_i^{(4)}(x, y_m) = \ln w(x, y_m, s_i) - \ln \tilde{w}_0(x, y_m, s_i).$$

Then the final $g^{(4)}(x_n, y)$ is computed by

$$g^{(4)}(x, y_m) = \frac{1}{M} \sum_{j=N+2M}^{N+3M-1} g_i^{(4)}(x, y_m).$$

The required function $g^{(4)}$ is computed by

$$g^{(4)}(\boldsymbol{x}) = \frac{1}{2}\left[g^{(4)}(x_n, y) + g^{(4)}(x, y_m)\right] \quad , \quad \text{where } \boldsymbol{x} \in \Omega. \tag{3.23}$$

(ii) Once we know $g^{(n)}$, $n = 1, 2, 3, 4$, we compute $u^{(n)}$, $n = 1, 2, 3, 4$, which represent the first guess of tail from each angle. We compute them by

$$
\begin{aligned}
u^{(1)}(\boldsymbol{x}) &= \ln \tilde{w}_0(\boldsymbol{x}, s_0) + g^{(1)}(\boldsymbol{x}) \\
u^{(2)}(\boldsymbol{x}) &= \ln \tilde{w}_0(\boldsymbol{x}, s_N) + g^{(2)}(\boldsymbol{x}) \\
u^{(3)}(\boldsymbol{x}) &= \ln \tilde{w}_0(\boldsymbol{x}, s_{N+M}) + g^{(3)}(\boldsymbol{x}) \\
u^{(4)}(\boldsymbol{x}) &= \ln \tilde{w}_0(\boldsymbol{x}, s_{N+2M}) + g^{(4)}(\boldsymbol{x})
\end{aligned}
$$

on Ω where s_0, s_N, s_{N+M} and s_{N+2M} are the farthest light source location of each angle. Then we compute function $w^{(i)}(\boldsymbol{x}) = \exp\left(u^{(i)}(\boldsymbol{x})\right)$, $i = 1, 2, 3, 4$ and solve for $a^{(i)}$ from the equation

$$
\Delta w^{(i)}(\boldsymbol{x}) - a^{(i)}(\boldsymbol{x}) w^{(i)}(\boldsymbol{x}) = 0
$$

by the weak form of FEM. Let η be the test function. Multiplying both side of above equation by η and integrating over Ω. We obtain

$$
\int_{\Omega} \eta \Delta w^{(i)} \, d\boldsymbol{x} - \int_{\Omega} \eta a^{(i)} w^{(i)} \, d\boldsymbol{x} = 0
$$

$$
\int_{\partial\Omega} \eta(\vec{n} \cdot \nabla w^{(i)}) \, d\boldsymbol{x} - \int_{\Omega} \nabla\eta \cdot \nabla w^{(i)} \, d\boldsymbol{x} - \int_{\Omega} \eta a^{(i)} w^{(i)} \, d\boldsymbol{x} = 0.
$$

Since there is no Robin condition on domain Ω, the first terms is dropped. We then numerically solve the weak form of the following equation

$$
\int_{\Omega} \nabla\eta \cdot \nabla w^{(i)} \, d\boldsymbol{x} + \int_{\Omega} \eta a^{(i)} w^{(i)} \, d\boldsymbol{x} = 0, \quad , \quad a^{(i)} = k^2 \text{ on } \partial\Omega.
$$

(iii) After $a^{(i)}$, $i = 1, 2, 3, 4$ are computed, we average them to get a_{tail} by

$$
a_*(\boldsymbol{x}) = \frac{1}{4}[a^{(1)}(\boldsymbol{x}) + a^{(2)}(\boldsymbol{x}) + a^{(3)}(\boldsymbol{x}) + a^{(4)}(\boldsymbol{x})] \quad , \quad \text{where } \boldsymbol{x} \in \Omega. \tag{3.24}
$$

Note: in iterations for improving quality of tail, subsection 3.3.2.3, we had observed that this $a_*(\boldsymbol{x})$ consists of a background noise, see figure 3.6(a), which make iterations

did not give a good approximation of tail. We solve this problem by removing this background as following. Let $H_1 = \frac{1}{2}\max\{a_*(\boldsymbol{x}) - k^2\}$ in Ω. We set

$$a_{**}(\boldsymbol{x}) = \begin{cases} k^2 & \text{, if } a_*(\boldsymbol{x}) < k^2 + H_1 \\ a_*(\boldsymbol{x}) - H_1 & \text{, otherwise} \end{cases} . \tag{3.25}$$

Above is cutting of 50% of the portion that greater than k^2, see figure 3.6(b). Then we rescale $a_{**}(\boldsymbol{x})$ to have the maximum height that is suitable for the iterations in subsection 3.3.2.3 for any inclusion examples. This maximum height are numerical found to be $k^2 * 1.1$, and we rescale it as following. Let $H_2 = \max\{a_{**}(\boldsymbol{x}) - k^2\}$ in Ω and $V = k^2 * 0.1$. We set

$$a_{\text{tail}}(\boldsymbol{x}) = k^2 + (a_{**}(\boldsymbol{x}) - k^2) * \frac{V}{H_2}. \tag{3.26}$$

After the rescale process, see figure 3.6(c), we solve the weak form of FEM for w_{tail} on Ω by

$$\int_\Omega \nabla\eta \cdot \nabla w_{\text{tail}}\, d\boldsymbol{x} + \int_\Omega \eta a_{\text{tail}} w_{\text{tail}}\, d\boldsymbol{x} = 0, \quad , \quad w_{\text{tail}} = \varphi(\boldsymbol{x}, s_0) \text{ on } \partial\Omega.$$

Note that, $s_0 = \bar{s}$ which is the farthest light source in our layer stripping, see section 2.2.

(iv) We compute the first guess for tails

$$\bar{v}_0(\boldsymbol{x}) = \frac{\bar{u}_0(\boldsymbol{x})}{\bar{s}^2} = \frac{\ln w_{\text{tail}}}{\bar{s}^2}, \quad \boldsymbol{x} \in \Omega. \tag{3.27}$$

This tail $\bar{v}_0(\boldsymbol{x})$ is known as the first guess. By using $\bar{v}_0(\boldsymbol{x})$ as a tail function for the inverse problem, it has provided most of the information about locations of the inclusions. These locations were reconstructed precisely. However the peak value of the reconstructed coefficient within inclusions was too low compared to the peak of original inclusions. Hence an iteration procedure for improving the quality of $\bar{v}_0(\boldsymbol{x})$ is required and is explained in the following section.
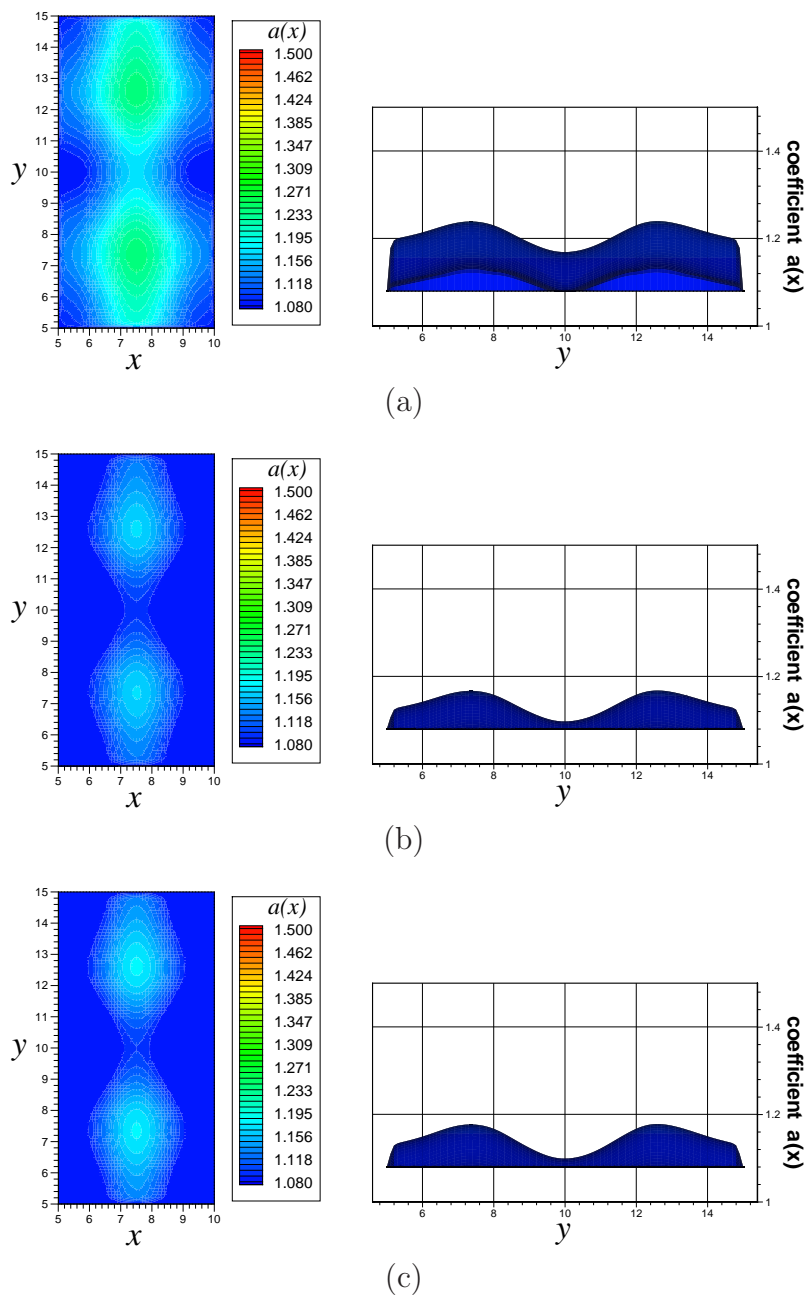
Figure 3.6. (a) Show the distribution of $a_*(\boldsymbol{x})$ in Ω and its cross section profile. (b) Show the distribution of $a_{**}(\boldsymbol{x})$ and its cross section profile. (c) Show the distribution of $a_{\mathrm{tail}}(\boldsymbol{x})$ and its cross section profile.

3.3.2.3 The Iterations for Improving Quality of Tail

An improving procedure in this section is introduced to calibrate the tail function, so that its limiting solution (when it exists) will satisfy the original diffusion model. This involves an iterative process that enhances the reconstructed inclusion. This idea is motivated by letting the following two diffusion equation be evaluated at light source $\boldsymbol{x}_0 = (B, \bar{s})$

$$\Delta \bar{w}_{i-1} - a_{i-1}\bar{w}_{i-1} = \delta \,, \tag{3.28}$$

$$\Delta \bar{w}_i - a_i \bar{w}_i = \delta \,. \tag{3.29}$$

The difference of above two equation can be written as follows

$$\Delta p_i - a_i p_i = (a_i - a_{i-1})\bar{w}_{i-1} \,. \tag{3.30}$$

where $p_i = \bar{w}_i - \bar{w}_{i-1}$. The purpose of this iteration scheme is to improve the quality of $w(\boldsymbol{x}, \bar{s})$. We expecting that $\bar{w}_i(\boldsymbol{x}, \bar{s})$ will converge to a value close to the exact value $w^*(\boldsymbol{x}, \bar{s})$ discussed in subsection 2.3.1 resulting in the tail function $u_\infty(\boldsymbol{x})$ which is close to $u^*(\boldsymbol{x}, \bar{s})$. The iteration process is done by the following procedure:

Step 0. The iteration is initiated with $\bar{w}_0(\boldsymbol{x}, \bar{s})$ being the solution of the uniform background $a_0(\boldsymbol{x}) = k^2$ on Ω and $a_1(\boldsymbol{x})$ obtained from $a_1(\boldsymbol{x}) = \max\{a_{\text{tail}}(\boldsymbol{x}), k^2\}$.

Step 1. We solve equation (3.30) by setting $i = 1$ using the weak form of FEM. Let η be the test function. Multiplying both side of the equation (3.30) by η and integrating over Ω. We obtain

$$\int_\Omega \eta \Delta p_1 \, d\boldsymbol{x} - \int_\Omega \eta a_1 p_1 \, d\boldsymbol{x} = \int_\Omega \eta (a_1 - a_0)\bar{w}_0 \, dx$$

$$\int_{\partial\Omega} \eta(\vec{n} \cdot \nabla p_1) \, d\boldsymbol{x} - \int_\Omega \nabla \eta \cdot \nabla p_1 \, d\boldsymbol{x} - \int_\Omega \eta a_1 p_1 \, d\boldsymbol{x} = \int_\Omega \eta (a_1 - a_0)\bar{w}_0 \, dx \,.$$

Since there is homogeneous Robin condition on domain Ω, the first terms is dropped.

We then numerically solve the weak form of the following equation

$$\int_\Omega \nabla\eta \cdot \nabla p_1 \, d\boldsymbol{x} + \int_\Omega \eta a_1 p_1 \, d\boldsymbol{x} = -\int_\Omega \eta(a_1 - a_0)\bar{w}_0 \, d\boldsymbol{x}. \tag{3.31}$$

The Dirichlet condition in the above equation is $p_1(\boldsymbol{x}, \bar{s}) = \varphi(\boldsymbol{x}, \bar{s}) - \bar{w}_0(\boldsymbol{x}, \bar{s})$ on $\partial\Omega$.

Once we have p_1 on Ω we can compute $\bar{w}_1(\boldsymbol{x}, \bar{s}) = p_1(\boldsymbol{x}, \bar{s}) + \bar{w}_0(\boldsymbol{x}, \bar{s})$ on Ω. And then

compute $\bar{a}(\boldsymbol{x})$ from $\bar{w}_1(\boldsymbol{x})$ using the similar weak form as above equation (3.31) except

the right hand side is zero as follows

$$\int_\Omega \nabla\eta \cdot \nabla\bar{w}_1 \, d\boldsymbol{x} + \int_\Omega \eta\bar{a}\bar{w}_1 \, d\boldsymbol{x} = 0. \tag{3.32}$$

with Dirichlet condition $\bar{a}(\boldsymbol{x}) = k^2$ on $\partial\Omega$. Now move to step 2 by setting $a_2(\boldsymbol{x}) = \max\{\bar{a}(\boldsymbol{x}), k^2\}$.

Step 2: This step is similar to step 1, but the Dirichlet condition of solving

(3.30) is different. We solve equation (3.30) by setting $i = 2$ using the weak form

$$\int_\Omega \nabla\eta \cdot \nabla p_2 \, d\boldsymbol{x} + \int_\Omega \eta a_2 p_2 \, d\boldsymbol{x} = \int_\Omega \eta(a_2 - a_1)\bar{w}_1 \, d\boldsymbol{x}. \tag{3.33}$$

The Dirichlet condition in the above equation is $p_2(\boldsymbol{x}, \bar{s}) = 0$ on $\partial\Omega$. This is because

$\bar{w}_i(\boldsymbol{x}, \bar{s})$ for $i > 0$ is the solution of non uniform background, we use $\bar{w}_i(\boldsymbol{x}, \bar{s}) = \varphi(\boldsymbol{x}, \bar{s})$

on $\partial\Omega$ for $i > 0$. Once we have p_2 on Ω we compute $w_2(\boldsymbol{x}, \bar{s}) = p_2(\boldsymbol{x}, \bar{s}) + \bar{w}_1(\boldsymbol{x}, \bar{s})$ on

Ω. And then compute $\bar{a}(\boldsymbol{x})$ using the weak form

$$\int_\Omega \nabla\eta \cdot \nabla w_2 \, d\boldsymbol{x} + \int_\Omega \eta\bar{a}w_2 \, d\boldsymbol{x} = 0. \tag{3.34}$$

with Dirichlet condition $\bar{a}(\boldsymbol{x}) = k^2$ on $\partial\Omega$. Now we move to step $i > 2$ by setting

$a_3(\boldsymbol{x}) = \max\{\bar{a}(\boldsymbol{x}), k^2\}$.

Step i: This step is similar to step 2, note that a_{i-1} is obtained from step $i - 1$.

We solve equation (3.30) by setting $i = n$ using the weak form

$$\int_\Omega \nabla\eta \cdot \nabla p_i \, d\boldsymbol{x} + \int_\Omega \eta a_i p_i \, d\boldsymbol{x} = \int_\Omega \eta(a_i - a_{i-1})\bar{w}_{i-1} \, d\boldsymbol{x}. \tag{3.35}$$

The Dirichlet condition in the above equation is $p_i(\boldsymbol{x}, \bar{s}) = 0$ on $\partial\Omega$. Once we have p_i on Ω we compute $\bar{w}_i(\boldsymbol{x}, \bar{s}) = p_i(\boldsymbol{x}, \bar{s}) + \bar{w}_{i-1}(\boldsymbol{x}, \bar{s})$ on Ω. And then compute $\bar{a}(\boldsymbol{x})$ using the weak form

$$\int_\Omega \nabla\eta \cdot \nabla\bar{w}_i \, d\boldsymbol{x} + \int_\Omega \eta\bar{a}\bar{w}_i \, d\boldsymbol{x} = 0 \,. \tag{3.36}$$

with dirichlet condition $\bar{a}(\boldsymbol{x}) = k^2$ on $\partial\Omega$. Now we move to the general step $i + 1$ by setting $a_{i+1}(\boldsymbol{x}) = \max\{\bar{a}(\boldsymbol{x}), k^2\}$.

From the above iteration process, the numerical implementation shows that $a_i(\boldsymbol{x}) > 0$ for all i. In fact, the contrast of $a_i(\boldsymbol{x})$ improves as i increases. This also results in the improvement of $\bar{w}_i(\boldsymbol{x}, \bar{s})$ as i increases.

To accelerate convergence, we slightly modify the iterative scheme in equation (3.30) by the term $\lambda_i(\boldsymbol{x})$ where

$$\lambda_i(\boldsymbol{x}) = \exp[Le^{i-1}\big(a_i(\boldsymbol{x}) - a_{i-1}(\boldsymbol{x})\big)^2] \,.$$

Now equation becomes

$$\Delta p_i - a_i p_i = \lambda_i(a_i - a_{i-1})\bar{w}_{i-1} \,. \tag{3.37}$$

With the introduction of $\lambda_i(\boldsymbol{x})$ for acceleration of convergence, the right hand side of equation (3.37) become an exponential function. The value L is used to control the growth of this exponential function. Furthermore, in our numerical computation we also remove background noise, equation (3.25), and rescale, equation (3.26), $a_1(\boldsymbol{x})$ before step 1 to have a certain peak corresponding to L which is set to 7.5 in our numerical computation. One benefit we obtain is that this value L and certain value peak of $a_1(\boldsymbol{x})$ are common for all cases with the same background value. That means in the actual application, we need only single calibration of L for each background value.

As i increases in the iteration, we control the growth of $a_i(\boldsymbol{x})$ by computing the forward problem

$$\Delta\hat{w}(\boldsymbol{x},\bar{s}) - a_i\hat{w}(\boldsymbol{x},\bar{s}) = \delta(\boldsymbol{x}-\boldsymbol{x}_0) \quad , \boldsymbol{x}_0 = (B,\bar{s}) \quad , \quad \boldsymbol{x}\in\Omega_0 \qquad (3.38)$$

with the same FEM formulation and condition as equation (3.4). And then we compare $\hat{w}(\boldsymbol{x},\bar{s})$ with $\varphi(\boldsymbol{x},\bar{s})$ at the middle point on the left boundary of Ω, say point $\boldsymbol{x}_{\mathrm{mid}}$. That is, if the peak value of $a_i(\boldsymbol{x})$ is high enough to make the light intensity of $\hat{w}(\boldsymbol{x},\bar{s})$ at $\boldsymbol{x}_{\mathrm{mid}}$ less than $\varphi(\boldsymbol{x},\bar{s})$, $\varphi(\boldsymbol{x}_{\mathrm{mid}},\bar{s}) - \hat{w}(\boldsymbol{x}_{\mathrm{mid}},\bar{s}) > 0$, we change the λ_i to be $\lambda_i = e^{M-i}$ where M is the number of iteration before we meet this criterion. With this scheme of iteration, we had observed in our numerical implementation that before $\varphi(\boldsymbol{x}_{\mathrm{mid}},\bar{s}) - \hat{w}(\boldsymbol{x}_{\mathrm{mid}},\bar{s}) > 0$, the light intensity $\bar{w}_i(\boldsymbol{x},\bar{s})$ is closed to the actual $w^*(\boldsymbol{x},\bar{s})$. The second choice of $\lambda_i = e^{M-i}$ will force the iteration to converge. The introduction of λ_i makes equations (3.31), (3.33) and (3.35) change to (3.39),

$$\int_\Omega \nabla\eta\cdot\nabla p_i\,d\boldsymbol{x} + \int_\Omega \eta a_i p_i\,d\boldsymbol{x} = \int_\Omega \eta\lambda_i(a_i - a_{i-1})\bar{w}_{i-1}\,d\boldsymbol{x}, \qquad (3.39)$$

where $i = 1,2,\dots$. After $i \geq M$, we iterate until the process converges, i.e., we stop iteration at $i = i_1$, where i_1 is defined via

$$\frac{\|\bar{a}_{i_1}(\boldsymbol{x}) - \bar{a}_{i_1-1}(\boldsymbol{x})\|_{L_2(\Omega)}}{\|\bar{a}_{i_1-1}(\boldsymbol{x})\|_{L_2(\Omega)}} < \varepsilon \qquad (3.40)$$

for a small $\varepsilon > 0$ of our choice.

To obtain more precise approximation of tail, we repeat above procedure with respect to light source s_N which is the farthest light source located on the bottom-right of Ω domain. (the latter iteration is computed with respect to $\bar{s} = s_0$.) Let's denote that this iteration give $\tilde{a}_{i_2}(\boldsymbol{x})$ as a results from same equation as equation (3.39). Then we compute function $\tilde{w}$ by

$$\int_\Omega \nabla\eta\cdot\nabla\bar{w}\,d\boldsymbol{x} + \int_\Omega \eta\left(\frac{\bar{a}_{i_1} + \tilde{a}_{i_2}}{2}\right)\bar{w}\,d\boldsymbol{x} = 0\,. \qquad (3.41)$$
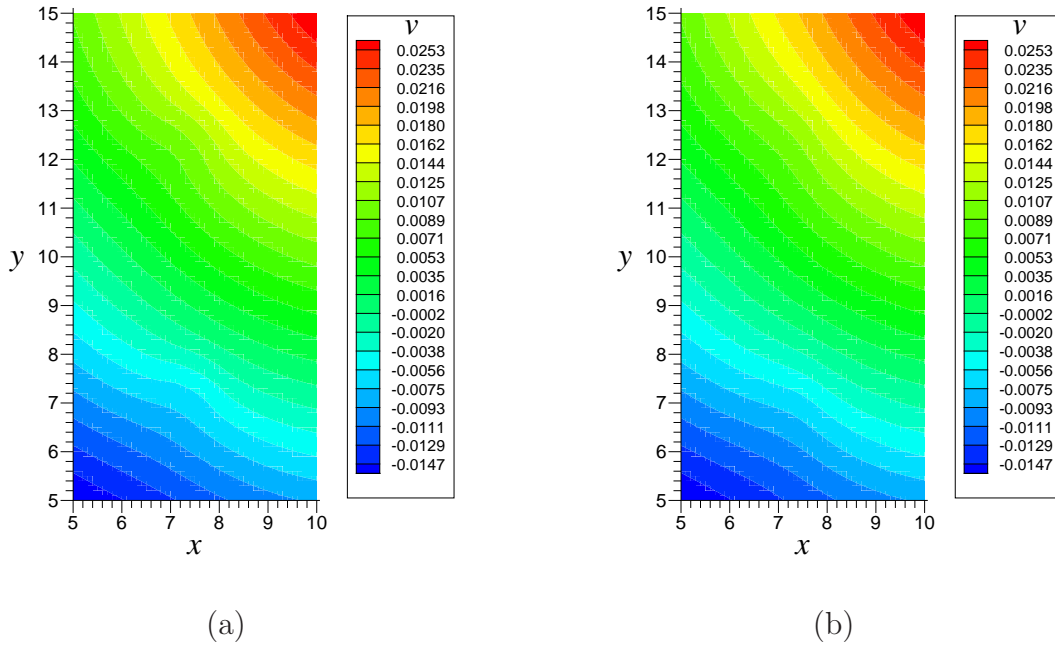
Figure 3.7. Comparison between (a) actual tail, $v(\boldsymbol{x}, \bar{s})$ and (b) approximated tail, $v_\infty(\boldsymbol{x})$.

Above equation is the weak form of FEM, see equation (**??**). The boundary condition is $\tilde{w}(\boldsymbol{x}) = \varphi_0(\boldsymbol{x})$ on $\partial\Omega$ which is the boundary with respect to $\bar{s} = s_0$ where $\bar{s}$ is the farthest light source in the inverse problem. Now we can compute the tail function by

$$v_\infty(\boldsymbol{x}) = \frac{\ln \bar{w}}{\bar{s}^2} \qquad (3.42)$$

Then we proceed by calculating the functions q_n in the following section.

Remark. Unfortunately we cannot yet prove that functions $a_i(\boldsymbol{x}) > 0$. There-fore, we cannot prove analytically neither the existence of solutions of the above Dirichlet boundary value problems for function $p_i(\boldsymbol{x}, \bar{s})$ nor the positivity of function $\bar{w}_i(\boldsymbol{x}, \bar{s})$. Neither can we analytically prove that functions $\bar{w}_i(\boldsymbol{x}, \bar{s})$ converge, nor that our tail $u_\infty(\boldsymbol{x})$ is close to the actual $u^*(\boldsymbol{x})$. Nevertheless, we observe all these "nice"

properties in our computations. Figure 3.7 displays the comparison of graphs of tails side by side, and shows there is little visible difference.

3.3.3 Numerical Computing of Layer Stripping

All the detail of Layer Stripping was given in section 2.2. In this section we focus on solving equation (2.29) for function $q_n^s(\boldsymbol{x})$. Theorem 2.3.2 proves that the algorithm in subsection 2.2.3 will converge for all $s \in [s_n, s_{n-1})$. Hence, to simplify the numerical computing of layer stripping, we can set parameter s of $q_n^s(\boldsymbol{x})$ to be $s = s_n$. By considering equations (2.24) and (2.25), at $s = s_n$ we have $q_n^s(\boldsymbol{x}) = q_n(\boldsymbol{x}) = q(\boldsymbol{x}, s_n)$. We then solve the equation

$$\Delta q_n(\boldsymbol{x}) - A_n(\nabla q_n)^2 - B_n \nabla q_n \nabla q_{n-1} - C_n \nabla q_n \nabla T_n$$

$$= D_n \Delta q_{n-1}(\boldsymbol{x}) + E_n \Delta T_n - F_n(\nabla q_{n-1})^2 - G_n \nabla q_{n-1} \nabla T_n - H_n(\nabla T_n)^2 \quad (3.43)$$

with the boundary condition $q_n(\boldsymbol{x}) = \psi_n(\boldsymbol{x}) = \psi(\boldsymbol{x}, s_n)$ on $\partial\Omega$.

Actually, the formation of equation (3.43) above is for the purpose of proving theorem 2.3.2. In our numerical implementation, we solve the equivalent equation but in a simpler expression as discussed in the following. First we rewrite equation (2.15) as

$$\Delta q + 2s^2 \nabla q \cdot \left(-\int_s^{\bar{s}} \nabla q \, d\tau + \nabla \bar{v} \right) + 4s \left(-\int_s^{\bar{s}} \nabla q \, d\tau + \nabla \bar{v} \right)^2$$

$$+ \frac{2}{s} \left(-\int_s^{\bar{s}} \Delta q \, d\tau + \Delta \bar{v} \right) = 0. \quad (3.44)$$

By discretizing the light souce, s, into

$$\bar{s} = s_0 > s_1 > \cdots > s_{N-1} > s_N = \underline{s}, \quad s_i - s_{i-1} = h,$$

where in above statement, h is negative value, unlike section 2.2. With $q_n(\boldsymbol{x}) = q(\boldsymbol{x}, s_n)$, we represent the integral term in equation (3.44) by Trapezoidal rule as follows

$$-\int_{s_n}^{\bar{s}} q\, d\tau = -\int_{s_n}^{s_0} q\, d\tau := \frac{1}{2}q_0 \cdot h + \sum_{i=1}^{n-1} q_i \cdot h + \frac{1}{2}q_n \cdot h \quad, \quad n = 1, 2, \ldots, N-1\,.$$

Hence, for each light source we have the following equations:

- for $n = 0$: the integral term will become zero, hence from equation (3.44)

$$\Delta q_0 + 2s_0^2 \nabla q_0 \cdot \nabla v_\infty + 4s_0 \nabla v_\infty \cdot \nabla v_\infty + \frac{2}{s_0}\Delta v_\infty = 0\,. \tag{3.45}$$

- for $n = 1, 2, \ldots, N-1$: Applying the Trapezoidal rule to equation (3.44) gives

$$\Delta q_n + 2s_n^2 \nabla q_n \cdot \left(\frac{1}{2}q_0 \cdot h + \sum_{i=1}^{n-1} q_i \cdot h + \frac{1}{2}q_n \cdot h + \nabla v_\infty\right)$$

$$+4s_n \left(\frac{1}{2}q_0 \cdot h + \sum_{i=1}^{n-1} q_i \cdot h + \frac{1}{2}q_n \cdot h + \nabla v_\infty\right)^2$$

$$+\frac{2}{s_n}\left(\frac{1}{2}q_0 \cdot h + \sum_{i=1}^{n-1} q_i \cdot h + \frac{1}{2}q_n \cdot h + \Delta v_\infty\right) = 0\,. \tag{3.46}$$

Note that in the above equations (3.45) and (3.46), for numerical implementation purposes, we replace the tail function $\bar{v}$ with v_∞. Now, let

$$T_n = q_0 \cdot h + 2\sum_{i=1}^{n-1} q_i \cdot h + 2\nabla v_\infty\,, \tag{3.47}$$

and note that this T_n is different from T_n in section 2.2. Substituting the latter into equation (3.46) and simplifying, we have

$$\Delta q_n + s_n^2 \nabla q_n \cdot (\nabla q_n \cdot h + \nabla T_n) + s_n (\nabla q_n \cdot h + \nabla T_n)^2 + \frac{1}{s_n}(\Delta q_n \cdot h + \Delta T_n) = 0\,. \tag{3.48}$$

We distribute all power terms in (3.48) and simplify again to obtain

$$\left(1 + \frac{h}{s_n}\right)\Delta q_n + \left(s_n^2 h + s_n h^2\right)\nabla q_n \cdot \nabla q_n$$

$$+\left(s_n^2 + 2s_n h\right)\nabla q_n \cdot \nabla T_n + s_n \nabla T_n \cdot \nabla T_n + \frac{1}{s_n}\Delta T_n = 0 \qquad (3.49)$$

The computation of equations (3.45) and (3.49) are done by weak form of FEM. Let η be the test function. Multiplying both side of equations (3.45) and (3.49) by η and integrating over Ω. We obtain:

- for $n = 0$:

$$-\mathcal{A}_0 \int_\Omega \eta \Delta q_0 \, d\Omega + \mathcal{C}_0 \int_\Omega \eta \nabla q_0 \cdot \nabla T_0 \, d\Omega = \mathcal{D}_0 \int_\Omega \eta \nabla T_0 \cdot \nabla T_0 \, d\Omega + \mathcal{E}_0 \int_\Omega \eta \Delta T_0 \, d\Omega$$

Integrating by part gives

$$-\mathcal{A}_0 \left(\int_{\partial\Omega} \eta(\vec{n} \cdot \nabla q_0) \, d\Omega - \int_\Omega \nabla\eta \cdot \nabla q_0 \, d\Omega\right) + \mathcal{C}_0 \int_\Omega \eta \nabla q_0 \cdot \nabla T_0 \, d\Omega$$

$$= \mathcal{D}_0 \int_\Omega \eta \nabla T_0 \cdot \nabla T_0 \, d\Omega + \mathcal{E}_0 \int_\Omega \eta \Delta T_0 \, d\Omega \,.$$

Since we have only the Dirichlet BC, then

$$\mathcal{A}_0 \int_\Omega \nabla\eta \cdot \nabla q_0 \, d\Omega + \mathcal{C}_0 \int_\Omega \eta \nabla q_0 \cdot \nabla T_0 \, d\Omega$$

$$= \mathcal{D}_0 \int_\Omega \eta \nabla T_0 \cdot \nabla T_0 \, d\Omega + \mathcal{E}_0 \int_\Omega \eta \Delta T_0 \, d\Omega \,. \qquad (3.50)$$

- for $n = 1, 2, \ldots, N-1$

$$-\mathcal{A}_n \int_\Omega \eta \Delta q_n \, d\Omega + \mathcal{B}_n \int_\Omega \eta \nabla q_n \cdot \nabla q_n \, d\Omega + \mathcal{C}_n \int_\Omega \eta \nabla q_n \cdot \nabla T_n \, d\Omega$$

$$= \mathcal{D}_n \int_\Omega \eta \nabla T_n \cdot \nabla T_n \, d\Omega + \mathcal{E}_n \int_\Omega \eta \Delta T_n \, d\Omega$$

Integrating by part gives

$$-\mathcal{A}_n \left(\int_{\partial\Omega} \eta(\vec{n} \cdot \nabla q_n) \, d\Omega - \int_\Omega \nabla\eta \cdot \nabla q_n \, d\Omega\right)$$

$$+\mathcal{B}_n \int_\Omega \eta \nabla q_n \cdot \nabla q_n \, d\Omega + \mathcal{C}_n \int_\Omega \eta \nabla q_n \cdot \nabla T_n \, d\Omega$$

$$= \mathcal{D}_n \int_\Omega \eta \nabla T_n \cdot \nabla T_n \, d\Omega + \mathcal{E}_n \int_\Omega \eta \Delta T_n \, d\Omega \,.$$

Since we have only the Dirichlet BC, we then have

$$\mathcal{A}_n \int_\Omega \nabla\eta \cdot \nabla q_n \, d\Omega + \mathcal{B}_n \int_\Omega \eta \nabla q_n \cdot \nabla q_n \, d\Omega + \mathcal{C}_n \int_\Omega \eta \nabla q_n \cdot \nabla T_n \, d\Omega$$

$$= \mathcal{D}_n \int_\Omega \eta \nabla T_n \cdot \nabla T_n \, d\Omega + \mathcal{E}_n \int_\Omega \eta \Delta T_n \, d\Omega. \tag{3.51}$$

The new notation in equations (3.50) and (3.51) are defined below

$$T_0 \;=\; 2v_\infty \quad,\quad T_n \;=\; q_0 \cdot h + 2\sum_{i=2}^{n-1} q_i \cdot h + 2v_\infty \quad,\quad n = 1,\ldots,N-1$$

$$\mathcal{A}_0 \;=\; -1 \quad,\quad \mathcal{A}_n \;=\; -\left(1 + \frac{h}{s_n}\right) \qquad,\quad n = 1,\ldots,N-1$$

$$\mathcal{B}_0 \;=\; 0 \quad,\quad \mathcal{B}_n \;=\; \left(s_n^2 h + s_n h^2\right) \qquad,\quad n = 1,\ldots,N-1$$

$$\mathcal{C}_0 \;=\; s_0^2 \quad,\quad \mathcal{C}_n \;=\; \left(s_n^2 + 2s_n h\right) \qquad,\quad n = 1,\ldots,N-1$$

$$\mathcal{D}_0 \;=\; -s_0 \quad,\quad \mathcal{D}_n \;=\; -s_n \qquad,\quad n = 1,\ldots,N-1$$

$$\mathcal{E}_0 \;=\; -\frac{1}{s_0} \quad,\quad \mathcal{E}_n \;=\; -\frac{1}{s_n} \qquad,\quad n = 1,\ldots,N-1.$$

The Dirichlet boundary condition for solving equation (3.50) and (3.51) is $q_n(\boldsymbol{x}) = \psi_n(\boldsymbol{x})$ on Ω where $\psi_n(\boldsymbol{x})$ is defined in equation (3.6).

Equations (3.50) and (3.51) which we derived above are used to solve the algorithm in section 2.2.3. Equation (3.50) is used to solve equation (2.33). Equation (3.51) is for solving equations (2.35) and (2.36) where $q_{i,k}^s$ are evaluated at $s = s_i$, $i = 1,\ldots,N-1$, hence we solve for $q_{i,k}$. The convergence criterion for

$$\lim_{k\to\infty} \|q_{i,k} - q_{i,k-1}\|_{L_2(\Omega)} = 0 \quad,\; i = 1,\ldots N-1$$

is replaced by

$$\frac{\|q_{i,k} - q_{i,k-1}\|_{L_2(\Omega)}}{\|q_{i,k}\|_{L_2(\Omega)}} < \varepsilon \tag{3.52}$$

for a small $\varepsilon > 0$ of our choice same as inequality (3.40). And when the above criterion is met, we set $q_i = q_{i,k}$.

Once q_n's are obtained for all $N - 1$, we use the backward substitution in next section to obtain the target coefficient $a(\boldsymbol{x})$.

3.3.4   Backward Substitution

Suppose that function $\{q_i\}_{i=0}^{N-1}$ are approximated via solving problems (3.50) and (3.51) with the boundary condition in (3.6). First we compute function $u_n(\boldsymbol{x}) = u(\boldsymbol{x}, s_n)$

$$
u_n(\boldsymbol{x}) = \begin{cases} s_0^2 v_\infty(\boldsymbol{x}) & , \ n = 0 \\ s_n^2 \left[-\dfrac{h}{2}\left(q_0(\boldsymbol{x}) + 2\sum_{j=1}^{n-1} q_j(\boldsymbol{x}) + q_n(\boldsymbol{x}) \right) + v_\infty(\boldsymbol{x}) \right] & , \ n \geq 1 \end{cases} , \quad (3.53)
$$

Then we compute function $w_n(\boldsymbol{x}) = w(\boldsymbol{x}, s_n)$ by

$$
w_n(\boldsymbol{x}) = \exp[u_n(\boldsymbol{x})] . \tag{3.54}
$$

Next, we use weak form of equation

$$
\Delta w_n(\boldsymbol{x}) - a_n(\boldsymbol{x}) w_n(\boldsymbol{x}) = 0 \quad , \quad \boldsymbol{x} \in \Omega
$$

by the similar FEM formulation as in (**??**)

$$
\int_\Omega \nabla \eta \cdot \nabla w_n \, d\boldsymbol{x} + \int_\Omega \eta a_n w_n \, d\boldsymbol{x} = 0 . \tag{3.55}
$$

where $a_n(\boldsymbol{x}) = k^2$ on $\partial\Omega$ to obtain the coefficient $a_n(\boldsymbol{x})$. And once a_n is obtained for all $n = 0, 1, \ldots, N - 1$, we compute the target coefficient $a(\boldsymbol{x})$ by

$$
a(\boldsymbol{x}) = \frac{1}{N} \sum_{n=0}^{N-1} a_n(\boldsymbol{x}) . \tag{3.56}
$$

CHAPTER 4

NUMERICAL IMPLEMENTATIONS AND RESULTS

We have performed numerical experiments in 2D on several cases of reconstructions using the numerical methods discussed in chapter 3. We have chosen the range of geometrical parameters of the rectangle $\mathcal{A}$, which is typical for optical imaging of small animals and have chosen the range of optical parameters typical for biological tissues [1][11][30].

4.1 Details of Numerical Implementations

4.1.1 Domains

In our numerical simulation, according to our numerical method, we need to do the computing in three different types of domain, i.e., Ω_0, Ω and $\mathcal{A}$. We define these three domains in the following, see also figure 4.1, and use them for all examples.

- Domain $\mathcal{A}$, the domain of interest, is defined as

$$\mathcal{A} = \{(\boldsymbol{x}) = (x, y) : 6\text{cm} < x < 9\text{cm}, \ 6\text{cm} < y < 14\text{cm}\}.$$

- Domain Ω, the computing domain, is defined as

$$\Omega = \{(\boldsymbol{x}) = (x, y) : 5\text{cm} < x < 10\text{cm}, \ 5\text{cm} < y < 15\text{cm}\}.$$

- Domain Ω_0, the simulating domain, is defined as

$$\Omega_0 = \{(\boldsymbol{x}) = (x, y) : 0\text{cm} < x < 15\text{cm}, \ 0\text{cm} < y < 20\text{cm}\}.$$

Dimension of these three domains are clearly defined, the relation of them is $\mathcal{A} \subset \Omega \subset \Omega_0$. Our simulations are based on the assumptions, see also figure 4.2, that
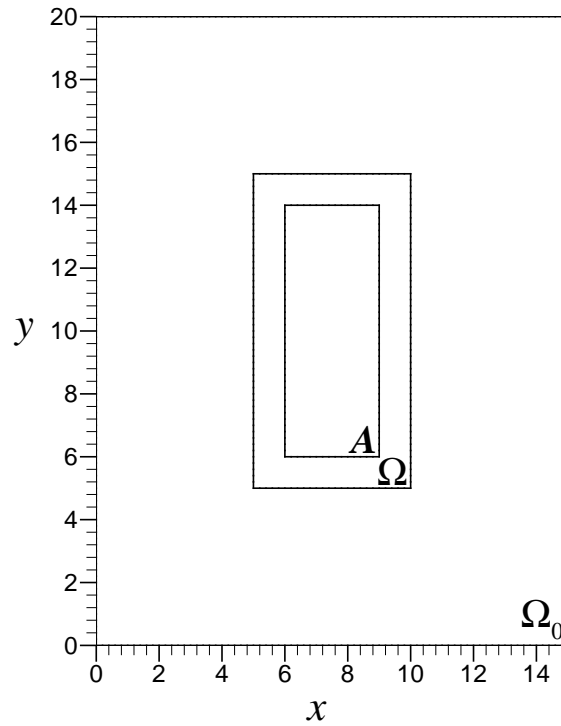
Figure 4.1. The dimension of Ω_0, Ω and $\mathcal{A}$.

(i) We assume that we know the background value of coefficients μ'_s and μ_a inside domain of interested, $\mathcal{A}$, but for the inclusions we don't know anything about them, i.e., location and shape.

(ii) For the domain $\Omega_0 - \mathcal{A}$, we assume that we can fill in the matching fluid where its coefficients μ'_s and μ_a have the same properties as the background of $\mathcal{A}$.

(iii) Light sources are merged into the matching fluid in $\Omega_0 - \mathcal{A}$ where their locations will be defined later in this chapter.

(iv) We can use the CCD Camera to measure the light intensity on $\partial\mathcal{A}$.
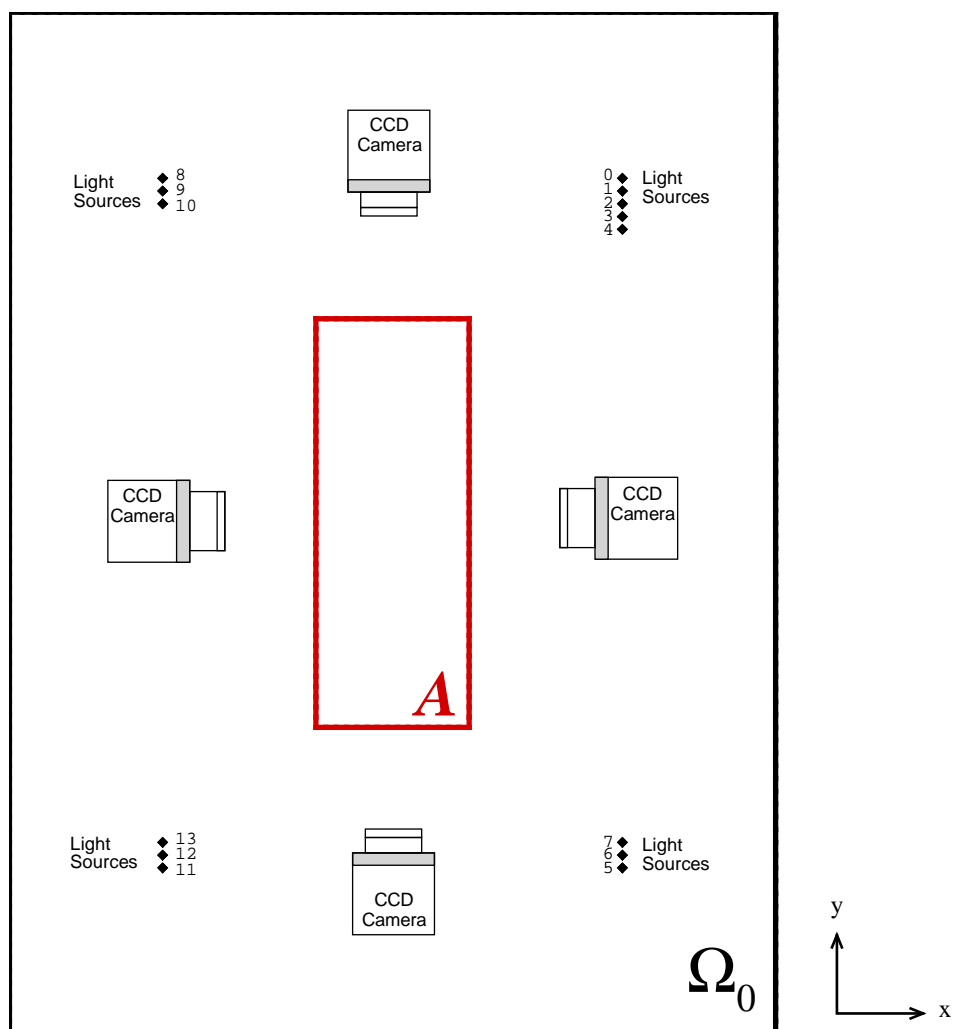
Figure 4.2. Schematic sketch of physical setting of our assumption.

4.1.2   Light Sources

The light sources are located in several positions $\boldsymbol{x}_0 = (12\text{cm}, s_i)$ along the left and $\boldsymbol{x}_0 = (3\text{cm}, s_i)$ along the right hand side of the rectangle $\mathcal{A}$ (in domain Ω_0). In our simulations, we have used an ideal light source modeled by the function $-\delta(\boldsymbol{x} - \boldsymbol{x}_0)$ in the 2D case of (1.1). In numerical simulation $\delta(\boldsymbol{x} - \boldsymbol{x}_0) = c\eta(\boldsymbol{x})$, where η is the finite element at the location and c is the scaling constant to ensure that the integral of δ in Ω_0 equal one.

In our setting, we use totally fourteen, 14, light sources to generate the measurement. Let's denote s_i as a representation of light source. The measurement data from light sources s_i, $i = 0, 1, 2, 3, 4$ located above and right of $\mathcal{A}$, first three, 3, are used for computation of tail from angle#1 and all five, 5, are used for the inverse problem. The light sources s_i, $i = 5, 6, 7$ located below and right of $\mathcal{A}$ are use for computation of tail from angle#2. The light sources s_i, $i = 8, 9, 10$ located above and left of $\mathcal{A}$ are use for computation of tail from angle#3. And lastly, the light sources s_i, $i = 11, 12, 13$ located below and left of $\mathcal{A}$ are use for computation of tail from angle#4, see figure 4.2. Note that, only light sources s_i, $i = 0, 1, 2, 3, 4$, are use for inverse problem, parameter B in $\boldsymbol{x}_0 = (B, s)$ is the fixed location of x for these light sources.

The value of s_i's are numerically show as follows

$$s_0 = 17\text{cm}, \ \ s_i = s_{i-1} - 0.2\text{cm}, \ \ i = 1, 2, 3, 4 \,,$$

$$s_5 = 3\text{cm}, \ \ s_i = s_{i-1} + 0.2\text{cm}, \ \ i = 6, 7 \,,$$

$$s_8 = 17\text{cm}, \ \ s_i = s_{i-1} - 0.2\text{cm}, \ \ i = 9, 10 \quad \text{and}$$

$$s_{11} = 3\text{cm}, \ \ s_i = s_{i-1} + 0.2\text{cm}, \ \ i = 12, 13 \,,$$

where $\boldsymbol{x}_0 = (B, s_i)$, $i = 0, \ldots, 7$ for light source on the right of $\mathcal{A}$ and $\boldsymbol{x}_0 = (\tilde{B}, s_i)$, $i = 8, \ldots, 13$ for light source on the left of $\mathcal{A}$. We set $B = 12\text{cm}$ and $\tilde{B} = 3\text{cm}$.

Although s_i's shown above are not too large to satisfies the condition we mention in subsection 3.3.2 but our numerical results have shown that the tail-function generated by using those values of s_i are approximated well, this reflects from the well reconstruction of $a(\boldsymbol{x})$. In fact, these value of s_i's cannot be set too large because the limitation of the size of space and the location of light source which cannot be located too far from $\mathcal{A}$. Another reason is about the background value in Ω_0. If the background value is large (which is our case), then s_i need to be close to to the domain of interest $\mathcal{A}$, otherwise the light intensity on the boundary of $\mathcal{A}$ is too small.

The number of total light sources for inverse problem in our numerical implementation is five, hence $N = 4$, see subintervals (2.18). Hence, we have computed four functions q_n, see subsection 3.3.3. An increase of the number N did not result in significant improvements of results.

4.1.3   CCD Camera (Charge-Coupled Device Camera)

The receivers, which mimic the so-called CCD camera, are located around domain $\mathcal{A}$. A CCD camera is an image sensor, consisting of an integrated circuit containing an array of linked, or coupled, light-sensitive capacitors. A typical CCD camera can take up to 512×512 data points simultaneously, which will provide an adequate amount of data for our reconstruction.

The measurements of light intensity on $\partial \mathcal{A}$ are taken when the light source s_i is turned on, only one light source can be turned on at a time. That means, the measurement for s_i is kept in $\bar{\varphi}(\boldsymbol{x}, s_i)$, $\boldsymbol{x} \in \partial \mathcal{A}$. For each detector position on the CCD camera, we introduce the random noise as the random process with respect to the detector locations, this noise was added to the measurement data from the forward problem. After we add noise, the measurement with noise will be kept in $\widetilde{\varphi}(\boldsymbol{x}, s_i)$, $\boldsymbol{x} \in \partial \mathcal{A}$, see subsection 3.3.1 for the corresponding of this boundary data.
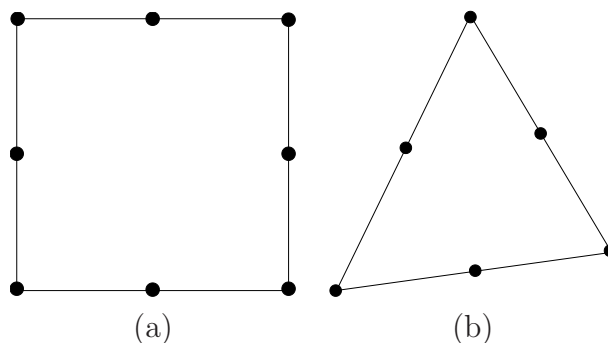
Figure 4.3. (a) Serendipity type of rectangular elements. (b) Quadratic triangular element.

Please note that, actually our measurement data are from the simulations where we compute the forward problem in domain Ω_0.

4.1.4 The Finite Element Mesh

In this study, we use a *serendipity type of rectangular elements*, see figure 4.3(a). The reason that we use rectangular element is because of the tail problem. According to equations (3.20), (3.21), (3.22) and (3.23), the element type should be rectangular. The serendipity type of rectangular element is selected because, bilinear type is not good for the high order equation and the other rectangular types with more point having a smooth high derivative will take too much time for computation.

The detail of finite element mesh are required to be taken into account of the calculation. We know that the dense-grids usually give better results than the coarse-grid but the cost of computational time is another issue that we have to consider. We discuss these details in subsection 5.2.1.

First we show in our simulation the computation in dense-grid, total of 150×200, x, y direction, rectangular elements of Ω_0 is used for forward calculations, see figure 4.4. We test our reconstruction method by using very dense grid for all calculation (see Chapter 5 for discussion of grid size). The total of 30×80 rectangular elements
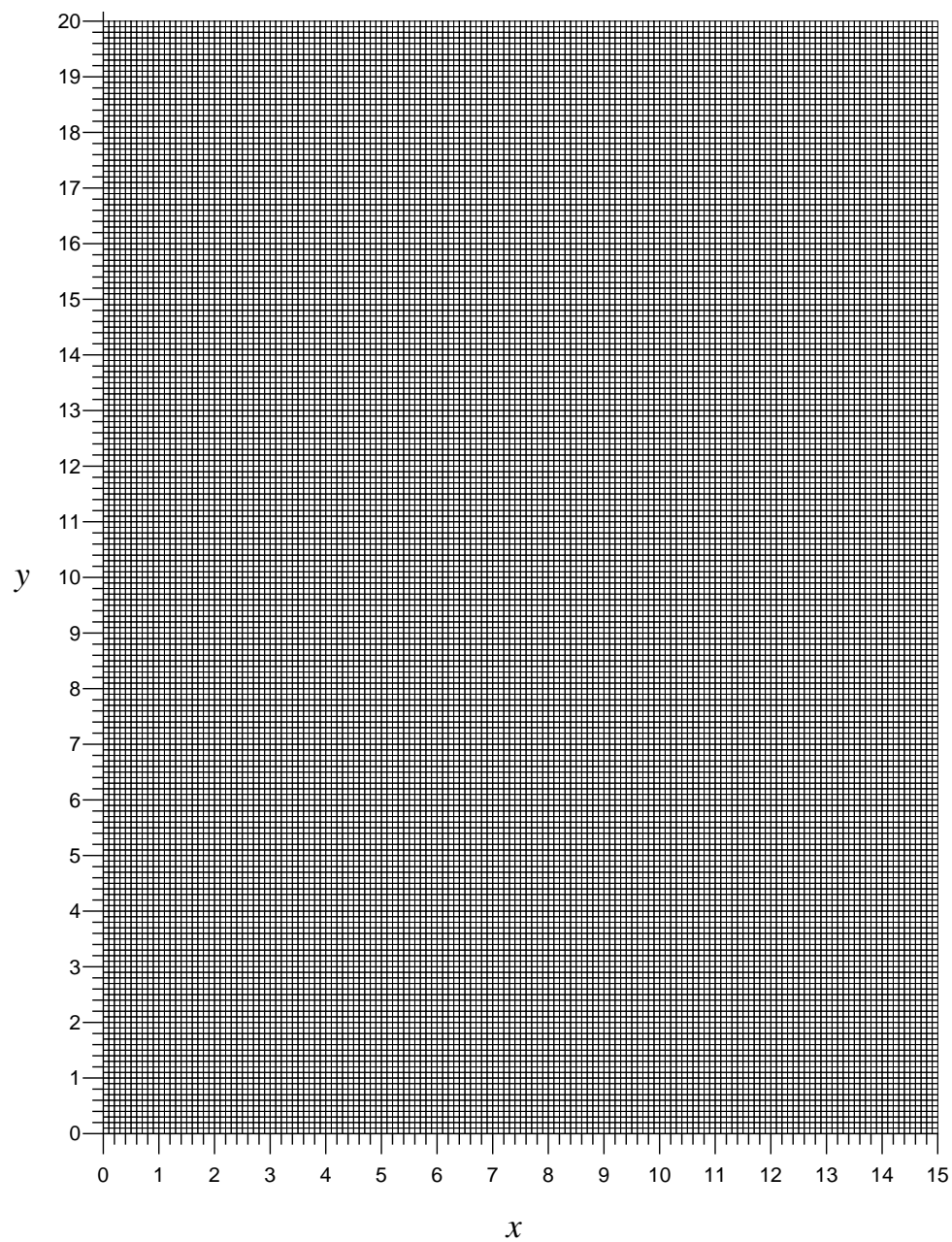
Figure 4.4. Domain mesh of Ω_0 (dense grid).
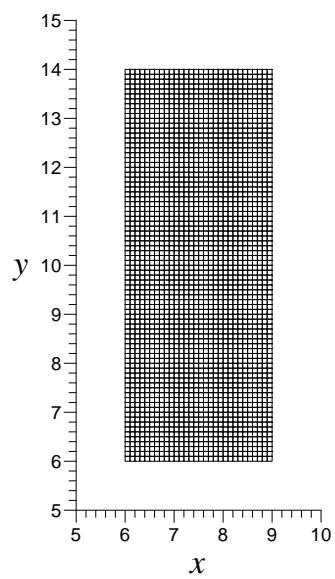
Figure 4.5. Domain mesh of $\mathcal{A}$ (dense grid).
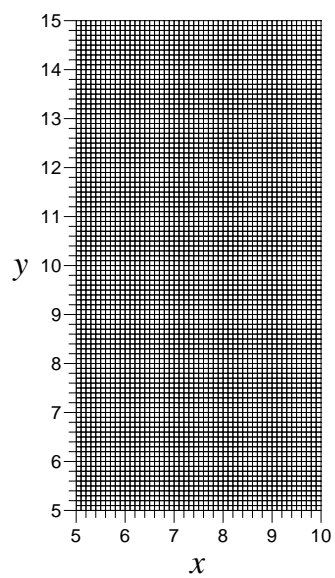
Figure 4.6. Domain mesh of Ω (dense grid).
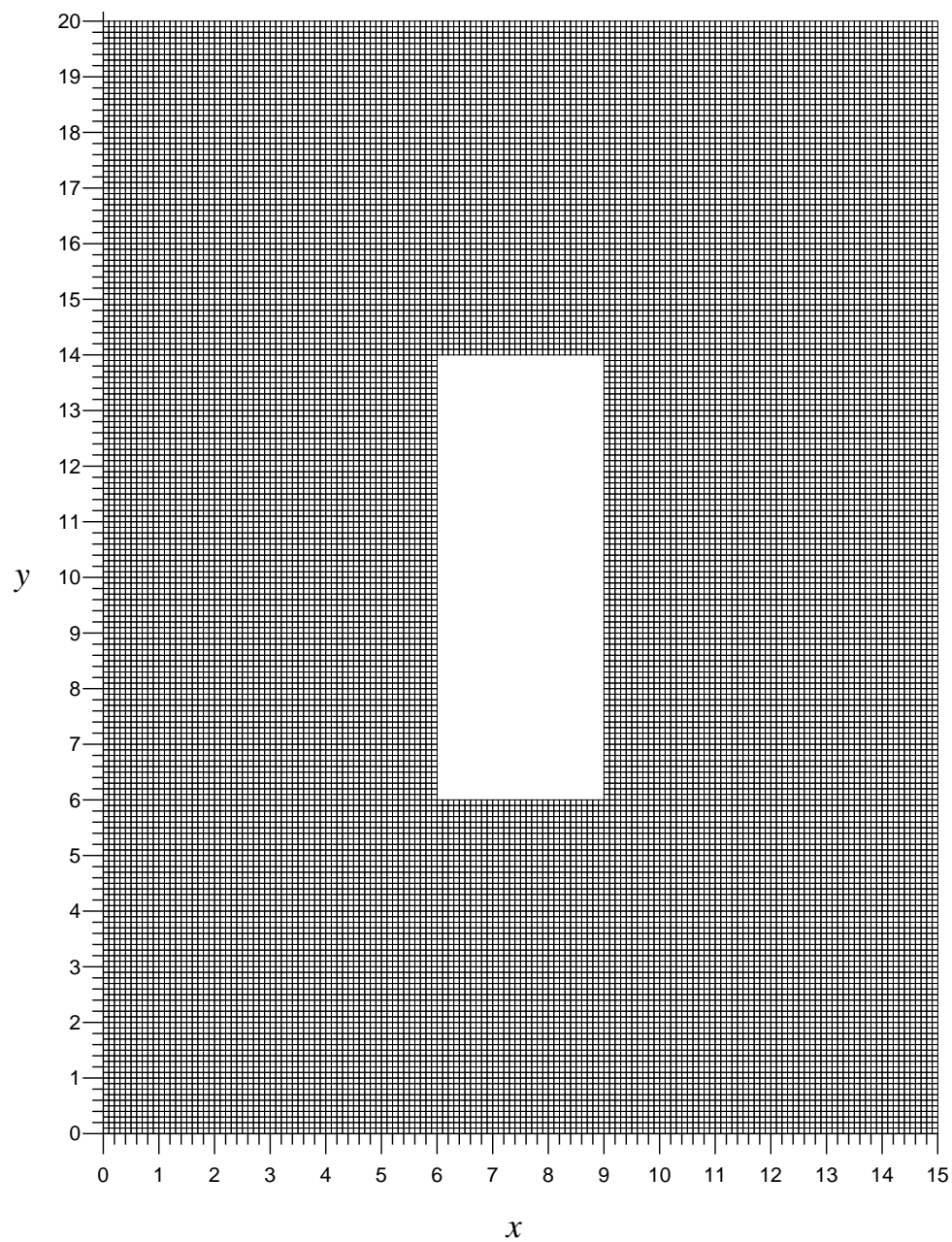
Figure 4.7. Domain mesh of $\Omega_0 - \mathcal{A}$ (dense grid).

is used for the domain of interest $\mathcal{A}$, see figure 4.5, and 50×100 rectangular elements is used for computing domain Ω, see figure 4.6. Note that both $\mathcal{A}$ and Ω are sub domain of Ω_0. The number of measurement points on left, right, top and bottom of rectangular $\mathcal{A}$ are 161, 161, 61 and 61 respectively. The measurement points at the corners of rectangular are shared by each sides and therefore the total number of independent measuring points is 440.

There is another domain in our computation which is $\Omega_0 - \mathcal{A}$, see figure 4.7. This domain is used for the exterior forward problem. It has the same grid size as Ω_0, there are totally 27,600 elements in $(\Omega_0 - \mathcal{A})$. The domain for computing equation (3.38) in subsection 3.3.2.3, the iterations for improving quality of tail, is also Ω_0.

4.1.5 Forward Problem

In our reconstruction simulation, we use the solution of the forward problem to generate the measurement data for the inverse problem, add noise to the measurement data, and reconstruct the absorption coefficient $a(\boldsymbol{x})$ in $\mathcal{A}$. Our new approach which different from [6][7][8] is that the domain $\mathcal{A}$ is not our basic computational domain for our inverse calculations.

For the forward problem, we calculated the solution of the diffusion equation

$$\nabla \cdot [D(\boldsymbol{x})\nabla w(\boldsymbol{x}, s)] - \mu_a w(\boldsymbol{x}, s) = -\delta(\boldsymbol{x} - \boldsymbol{x}_0) \quad , \quad \boldsymbol{x} \in \Omega_0 \qquad (4.1)$$

with the conventional boundary condition at the infinity

$$\lim_{|\boldsymbol{x}| \to \infty} w(\boldsymbol{x}, s) = 0 . \qquad (4.2)$$

Note that parameter s represents $\boldsymbol{x}_0 = (B, s)$ where $B = 3$cm or 12cm are constants in our numerical implementation. In our simulation, the setting of coefficients μ'_s and μ_a are according to what we mention in section 1.3. The reduced scattering coefficient μ'_s

are assumed to be constant. By typical value for biological tissues [1][11][30], we set the the diffusion coefficient $D(\boldsymbol{x}) = 1/(3\mu'_s(\boldsymbol{x})) = 0.0\dot{5}$cm, where optical coefficients $\mu'_s(\boldsymbol{x}) = 6.0$ and $\mu_a(\boldsymbol{x}) = 0.06$cm^{-1} at all grid except of the inclusions, and in inclusions μ_a ranges from 0.06 to 0.18cm^{-1}. The maximum inclusion/background contrast for μ_a is 3:1 in our computations. For this case, we let $a(\boldsymbol{x}) = 3(\mu'_s\mu_a)(\boldsymbol{x})$. Hence, instead of solving (4.1) we solve equation (1.1) with condition (1.2).

To simulate the measurement data, we calculate the forward problem with Robin boundary conditions at $\partial\Omega_0$, given the distribution of the absorption coefficients. And assign the simulated measurement with noise to the boundary of $\mathcal{A}$.

4.1.6 Exterior Forward Problem

The purpose of exterior forward problem is to replace our previous technique [6][7][8] in using the least-square polynomial to filter the noise in the measurement data. We compute equation (1.1) with condition (1.2) by assign dirichlet boundary which is measurement data with noise on $\partial\mathcal{A}$ and use Robin condition on $\partial\Omega_0$. This technique will provide us the smooth and continuous solution within domain of computation, i.e. area between $\partial\mathcal{A}$ and $\partial\Omega_0$ where $\partial\Omega \in \Omega_0 - \mathcal{A}$. From our numerical observation, we has noticed that the distance between $\partial\mathcal{A}$ and $\partial\Omega$ is relevant for the smoothness, i.e., the longer distance and the finer grid, the more smoothness on $\partial\Omega$. But we have also noticed that the longer the distance will give the worse quality of tail-function. Hence with this tradeoff, we select this distance to be 1cm on each side of rectangular and use the fine grids between $\partial\mathcal{A}$ and $\partial\Omega$. This fine grid consists of 100 elements per 1cm^2 in $\Omega_0 - \mathcal{A}$, see figure 4.7.

The approximation error of the solution of the exterior forward problem against the full forward problem on $\partial\Omega$ can be found in tables 4.1, 4.2 and see figure 4.8(b)
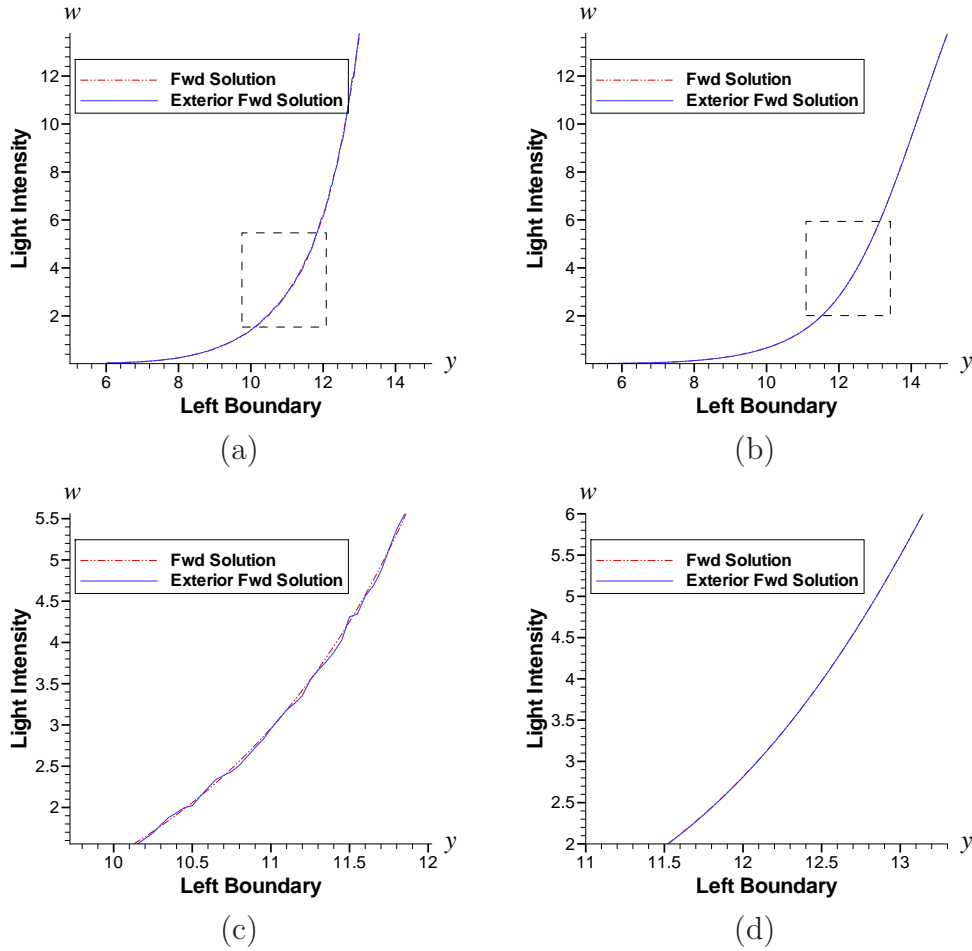
Figure 4.8. (a) Forward solution versus forward solution $+ 2\%$ noise on left boundary of $\mathcal{A}$. (b) Forward solution versus exterior forward solution on left boundary of Ω. (c) Expansion of figure (a) for area inside the box. (d) Expansion of figure (b) for area inside the box.

for the visual comparison of forward solution versus exterior forward solution on left boundary of Ω.

The Relative Root-Mean-Squared-Error (RMSE), Relative Absolute-Mean-Error (AME) and Relative Mean-Error (ME) are calculated as follows

$$\text{RMSE} = \frac{\sqrt{\sum_{k=1}^{N^{(\text{node})}} (w_k - \hat{w}_k)^2}}{N^{(\text{node})} \max_k |w_k|} \quad , \quad \text{AME} = \frac{\sum_{k=1}^{N^{(\text{node})}} |w_k - \hat{w}_k|}{N^{(\text{node})} \max_k |w_k|} \quad ,$$

$$\text{ME} = \frac{\sum_{k=1}^{N^{(\text{node})}} (w_k - \hat{w}_k)}{N^{(\text{node})} \max_k |w_k|} \, . \tag{4.3}$$

where w_k and $\hat{w}_k$ represent the solution at corresponding points of the full and exterior forward problem on $\partial\Omega$, respectively. $N^{(\text{node})}$ is the total number of nodes on $\partial\Omega$. RMSE measures better these larger differences, MAE is more indicative of average difference and ME compares with mean value difference.

Table 4.1. Errors of the exterior forward problem versus the full forward problem on $\partial\Omega$ of example #1, these are from 2% noise data

LIGHT#	RMSE	AME	ME
0	0.010811944064180	0.113783524730592	-0.059132289694731
1	0.009962963939674	0.104101115455916	-0.054046018358486
2	0.009279277734762	0.095243911278493	-0.049798762431824
3	0.008717856751564	0.086997793330275	-0.046267735122905
4	0.008239909575044	0.079331705596536	-0.043301401012661

Table 4.2. Errors of the exterior forward problem versus the full forward problem on $\partial\Omega$ of example #2, these are from 2% noise data

LIGHT#	RMSE	AME	ME
0	0.010812290171345	0.113800827755339	-0.059121912651744
1	0.009963693619538	0.104125490127432	-0.054040469590143
2	0.009279664383769	0.095261564648831	-0.049793150524432
3	0.008718135743947	0.087012215475611	-0.046259640974663
4	0.008239903972777	0.079339044475956	-0.043290319044263

This shows that our scheme of filtering is reasonable and that data on $\partial\Omega$ can be use for the reconstruction process.

4.1.7   Reconstruction (Inverse Problem)

This process simply follows the one we discuss in 3.2.2 for computing tail and 3.2.3 for the layer stripping. Note that, we use light sources located on 4 different

angles (3 lights source on each angle), see figure 4.2, for computing tail and we has been using 5 light sources (including 3 of tail) on top right of Ω for computing the layer stripping. Since five light source are used in the backward substitution (3.3.4), we will obtain four reconstructions, $\{a_i(\boldsymbol{x})\}_{i=0}^3$. After we average to get $a(\boldsymbol{x})$, the coefficient μ_a can be computed by, see equation (1.5),

$$\mu_a(\boldsymbol{x}) = a(\boldsymbol{x})/(3\mu'_s)(\boldsymbol{x}).$$

4.2 Numerical Results

In the following numerical examples, we illustrate the results in a few different shapes of the two inclusions. Our method has shown its success in dealing with those cases.

The convergence criterion for function $a_i(\boldsymbol{x})$ in the condition (3.40) in the iteration of improving quality of tail, subsection 3.3.2 is

$$\frac{\|a_{i_1}(\boldsymbol{x}) - a_{i_1-1}(\boldsymbol{x})\|}{\|a_{i_1-1}(\boldsymbol{x})\|} \equiv \frac{\sqrt{\sum_{j=1}^{N^{(\text{node})}}(a_{i_1,j} - a_{i_1-1,j})^2}}{N^{(\text{node})}\max_j |a_{i_1-1,j}|} < \varepsilon \qquad (4.4)$$

where $N^{(\text{node})}$ is number of finite element node in Ω domain. In all examples, $\varepsilon = 10^{-5}$.

The convergence criterion for function $q_{i,k}$ in the condition (3.52) in Numerical Computing of Layer stripping, subsection 3.3.3 is

$$\frac{\|q_{i,k} - q_{i,k-1}\|}{\|q_{i,k}\|} \equiv \frac{\sqrt{\sum_{j=1}^{N^{(\text{node})}}(q_{i,k,j} - q_{i,k-1,j})^2}}{N^{(\text{node})}\max_j |q_{i,k-1,j}|} < \varepsilon \qquad (4.5)$$

where $N^{(\text{node})}$ is number of finite element node in Ω domain In all examples, $\varepsilon = 10^{-5}$.

In all example, we assume μ'_s being a constant of value 6.0cm^{-1}. The only distribution at inclusion are μ_a and $a(\boldsymbol{x}) = (3\mu'_s\mu_a)(\boldsymbol{x})$.

4.2.1 Examples #1

Inclusions are two circles with a radius of 0.65cm, with their center are $(7.5\text{cm}, 7.5\text{cm})$ and $(7.5\text{cm}, 12.5\text{cm})$. The coefficient is $\mu_a(\boldsymbol{x}) = 0.18$ inside inclusions and $\mu_a(\boldsymbol{x}) = 0.06$ outside of inclusions. Hence coefficient $a(\boldsymbol{x}) = 3.24$ inside of inclusions and $a(\boldsymbol{x}) = 1.08$ outside of inclusions.

Total number of iterations for improving tail, subsection 3.3.2.3, are shown in table 4.3.

Table 4.3. Number of iterations for improving tail of examples #1

With respect to s_0	With respect to s_N
13	13

Figures 4.9(a) displays the original distribution and their 1D cross section. Figure 4.9(b) shows reconstruction from the noisy data and its 1D cross section, see additional figure in appendix B.1.

The relative errors of the reconstruction which are Root-Mean-Square-Error (RMSE), Absolute-Mean-Error (AME) and Relative Mean-Error (ME) are calculated as follows

$$\text{RMSE} = \frac{\sqrt{\sum_{k=1}^{N^{(\text{node})}} (a_k - \hat{a}_k)^2}}{N^{(\text{node})} \max_k |a_k|} \quad , \quad \text{AME} = \frac{\sum_{k=1}^{N^{(\text{node})}} |a_k - \hat{a}_k|}{N^{(\text{node})} \max_k |a_k|} \quad ,$$

$$\text{ME} = \frac{\sum_{k=1}^{N^{(\text{node})}} (a_k - \hat{a}_k)}{N^{(\text{node})} \max_k |a_k|} . \tag{4.6}$$

Note that $\{a_1, \dots, a_{N^{(\text{node})}}\}$ are the original distribution data in Ω and $\{\hat{a}_1, \dots, \hat{a}_{N^{\text{node}}}\}$ are its approximation, the values of them are taken at each of the grid points of the computation domain Ω, $N^{(\text{node})}$ is the total number of nodes in domain Ω.
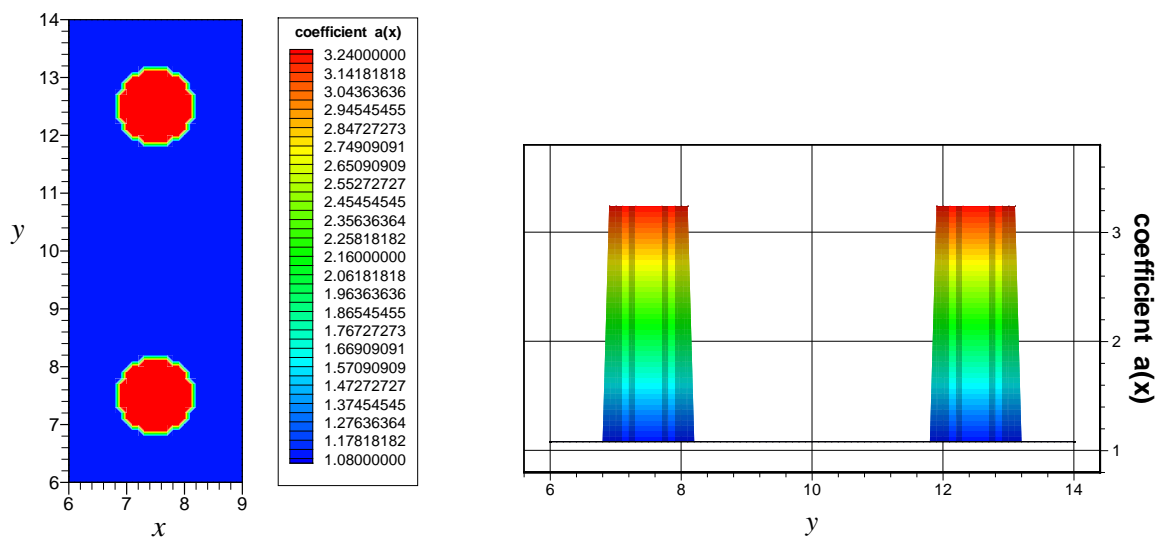
Average of left inclusion is 3.24 and right inclusion is 3.24.

(a)
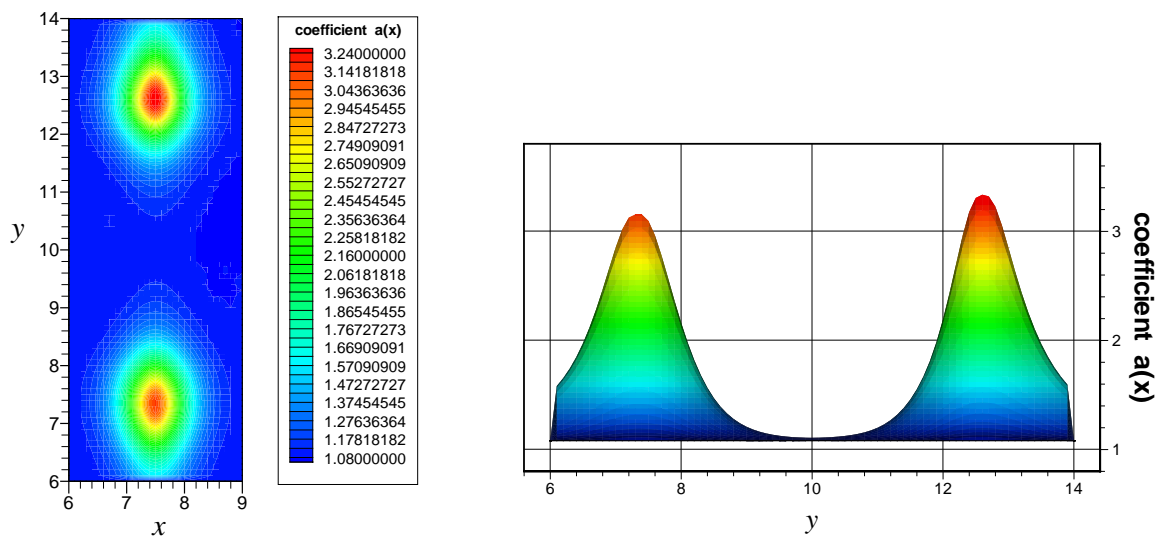
Peak value of left inclusion is 3.149 and right inclusion is 3.329.

(b)

Figure 4.9. (a) Displays the original coefficient $a(\boldsymbol{x})$ of example #1. (b) Shows its reconstruction result with 2% noise.

The relative errors of the reconstruction of this examples set are shown in following table.

Table 4.4. Relative errors of reconstructions of examples #1

RMSE	AME	ME
0.131168841277846	0.069546136198822	-0.003235976174744

4.2.2 Examples #2

Inclusions are two circles with a radius of 0.65cm, with their center are $(7.5\text{cm}, 7.5\text{cm})$ and $(7.5\text{cm}, 12.5\text{cm})$. The coefficient $\mu_a(\boldsymbol{x})$ is

$$\mu_a(\boldsymbol{x}) = \begin{cases} \max[0.3\cos\tilde{d}(\boldsymbol{x})(1+0.01\varrho_2(\boldsymbol{x})), 0.06] & \text{, inside inclusions} \\ 0.06 & \text{, outside of inclusions} \end{cases} \quad , \quad (4.7)$$

where $\tilde{d}(\boldsymbol{x}) = d(\boldsymbol{x})(1+0.1\varrho_1(\boldsymbol{x}))$, $d(\boldsymbol{x})$ is the minimum to center of each of circle radius r defining the inclusions. The inclusions also have random shape within the distance $\tilde{d}(\boldsymbol{x})$. Function ϱ_1 and ϱ_2 are a realization of a white noise valued between $[-1, 1]$. Hence coefficient $a(\boldsymbol{x}) \in [1.08, 3.24 + 1\%]$ inside of inclusions and $a(\boldsymbol{x}) = 1.08$ outside of inclusions. The random pattern is introduced to test the ability of our method to handle complex shapes.

Total number of iterations for improving tail, subsection 3.3.2.3, are show in table 4.5.

Table 4.5. Number of iterations for improving tail of examples #2

With respect to s_0	With respect to s_N
11	11

Figures 4.10(a) displays the original distribution and their 1D cross section. Figure 4.10(b) shows reconstruction from the noisy data and its 1D cross section, see additional figure in appendix B.2.

The relative errors of the reconstruction are as follows

Table 4.6. Relative errors of reconstructions in examples #2

RMSE	AME	ME
0.093793827273663	0.046578415964705	-0.002205327187045
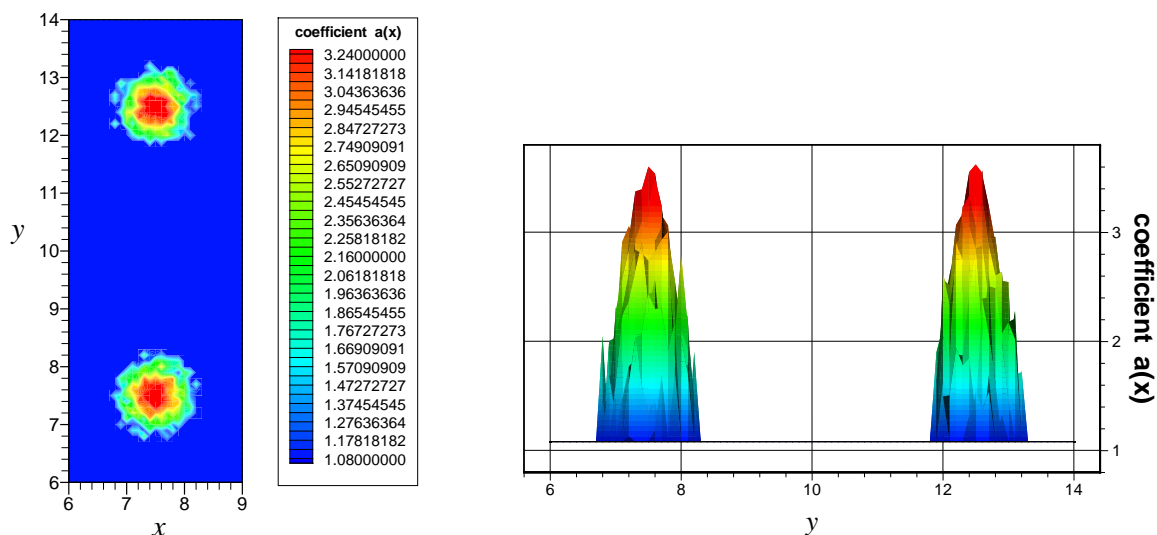
Average of left inclusion is 2.287 and right inclusion is 2.349.

(a)
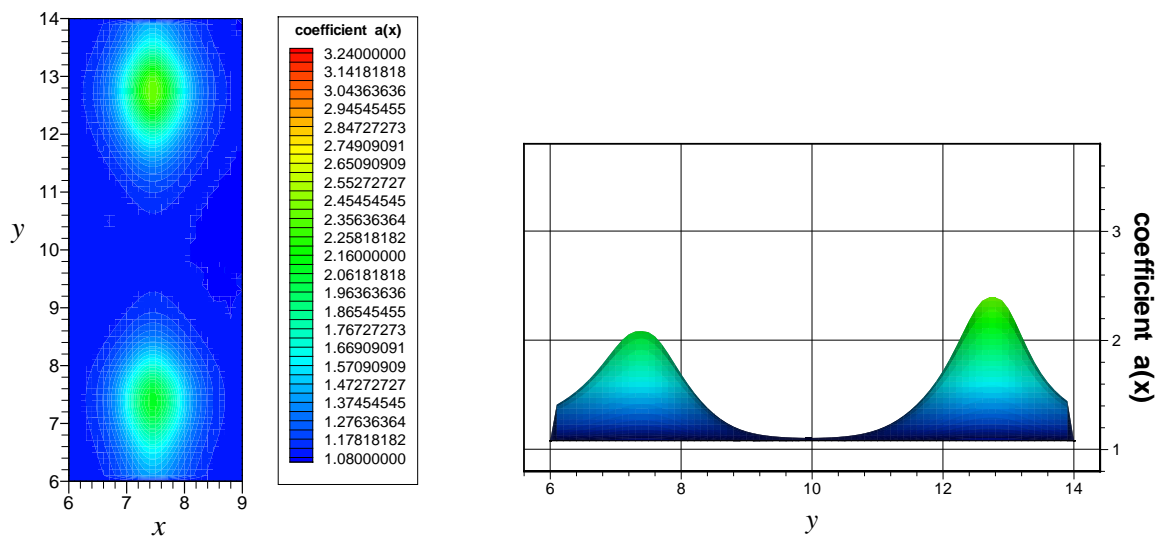
Peak value of left inclusion is 2.081 and right inclusion is 2.389.

(b)

Figure 4.10. (a) Displays the original coefficient $a(\boldsymbol{x})$ of example #2. (b) Shows its reconstruction result with 2% noise.

CHAPTER 5

CONCLUSIONS AND DISCUSSION

5.1 Conclusions

Our numerical experiments indicated that this method, globally convergent reconstruction (GCR), is quite stable. Computation results show a good performance for a realistic range of parameters. This method is particularly useful for reconstruction of the interesting domain of rectangular shape. It is also a useful tool for NIR reconstruction of the range of optical parameters typical for biological tissues [1][11][30]. It is also can be applied to an application include medical optical imaging, imaging of land mines via electrical impedance tomography and image of military targets through smogs and flames using lasers.

Our numerical results suggest that at most five measurements of light intensity at $\partial \mathcal{A}$ are sufficient to obtain a good quality reconstructed image. This is another advantage of this GCR method. We expected that an increase in measurements would lead to the more stable or regularized reconstructions for these ill-posed problems. However, our numerical experiments did not confirm that.

The major difficulty in our case is to figure out the tail-function. By using the transformation in equation (2.14) we obtain an approximation of tail as close as we want then improve the tail-function by using more light sources located on different angles and using iterations to improve quality of tail. The numerical results confirmed that this tail are approximated well and we get a good reconstruction image from this tail.

80
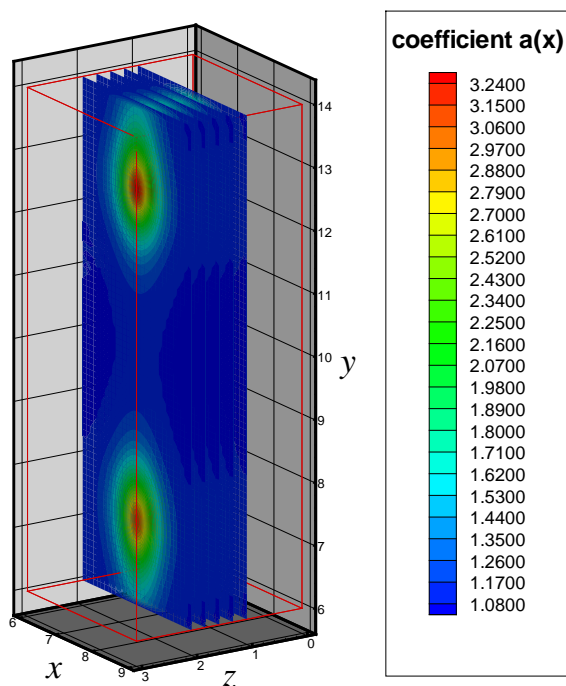
Figure 5.1. Sequence of 2D slices of 3D domain.

Our scheme of filtering noisy data by projecting them from $\partial \mathcal{A}$ to $\partial \Omega$ with solving exterior forward problem requires the physical setting related to "matching fluid." It is also important that to assign mathematically optical properties outside the domain of interest (in order to get that "matching fluid"), we do not need to know the optical properties within domain $\mathcal{A}$. Instead, we need to know the optical properties of the background at its boundary. The latter stresses the fact that we have a GCR rather than a locally convergent method and that our method needs far less presumption on the distribution of optical property at the interior of the domain $\mathcal{A}$.

For the reconstruction of 3D image, we can also use our current reconstruction version as a sequence of 2D slices of 3D domain, similar to CT scan, CT stands for "Computational Tomography", see figure 5.1.

5.2 Discussions

5.2.1 Computational Time

Computation time is one consideration in designing the reconstruction algorithm. Our algorithm consist of (1) forward problem, (2) forward exterior problem, and (3) inverse problem. The computation time for forward problem are not considered in the algorithm since, in the real case, we obtain the boundary data from the measurement of CCD Camera. The average computation time on *Intel(R) Core(TM)2 Quad CPU Q6600 2.4GHz with 3.24GB of RAM (Random Access Memory)* for the result in section 4.2 are shown in table 5.1.

Table 5.1. Computation time for results in section 4.2 in dense grid

Example No.	Forward exterior problem	Inverse problem	Total time
1	1 min. 6 sec.	15 min. 48 sec.	16 min. 54 sec.
2	1 min. 5 sec.	15 min. 54 sec.	16 min. 59 sec.

The computations take a large amount of time because they are computed in dense-grid. We will show that our algorithm also works well in a coarse-grid. The domain that are taking into account for the computation are Ω_0, $\mathcal{A}$, Ω and $(\Omega_0 - \mathcal{A})$. Suppose that now we will consider only (1) forward exterior problem and (2) inverse problem (assuming that the boundary data are obtain from CCD Camera). We have changed these domains to contain a new grid which are coarse-grid. Domain Ω_0 has total of 75×100, x, y direction, rectangular elements. It is used for computing the equation (3.38) in subsection 3.3.2.3. The total of 15×40 rectangular elements is used for the interested domain $\mathcal{A}$, see figure 5.3, and 25×50 rectangular elements is used for computing domain Ω, see figure 5.4. The number of measurement points on left, right, top and bottom of rectangular $\mathcal{A}$ are 81, 81, 31 and 31 respectively.
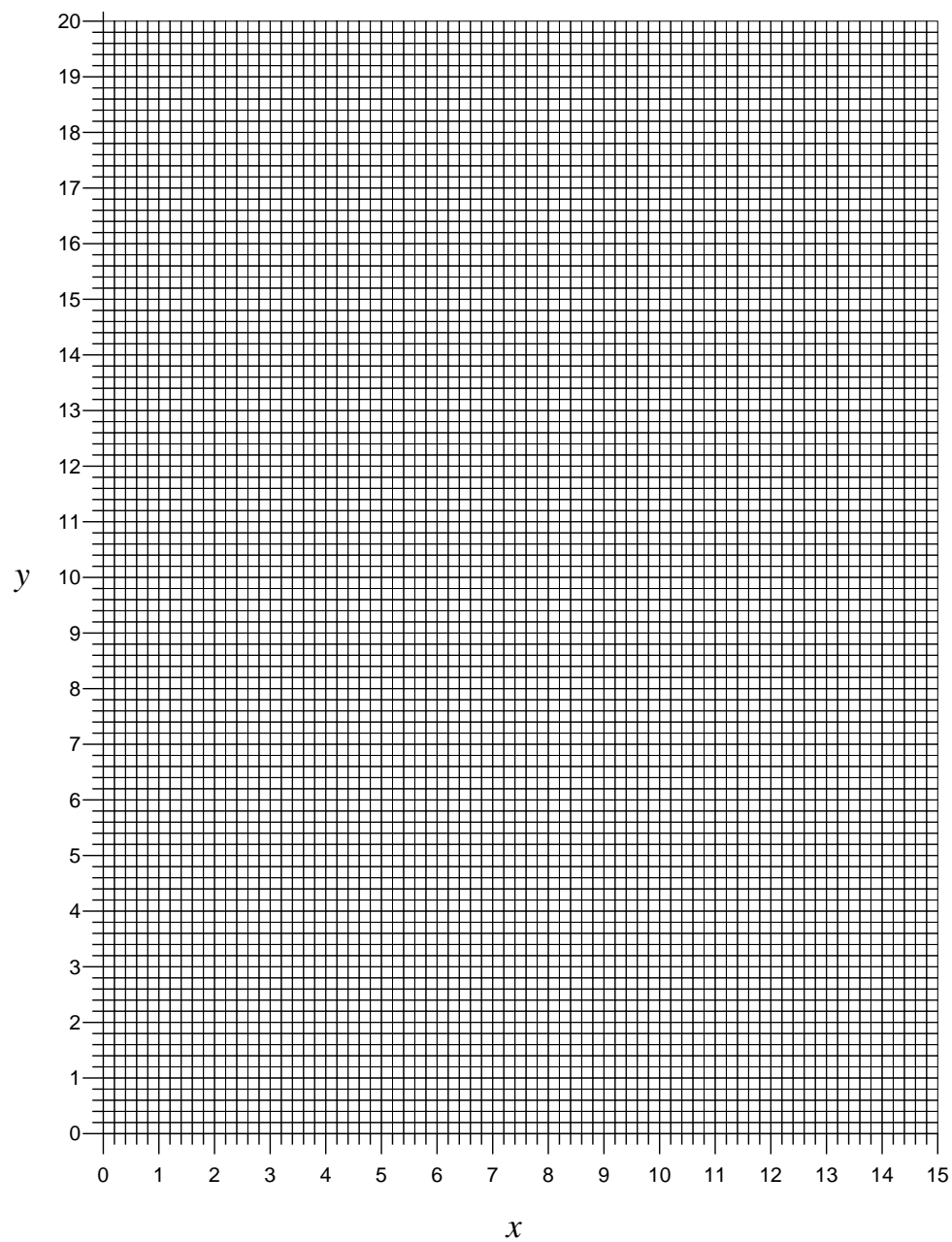
Figure 5.2. Domain mesh of Ω_0 (coarse grid).
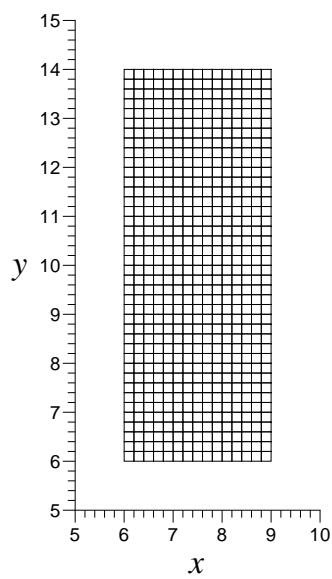
Figure 5.3. Domain mesh of $\mathcal{A}$ (coarse grid).
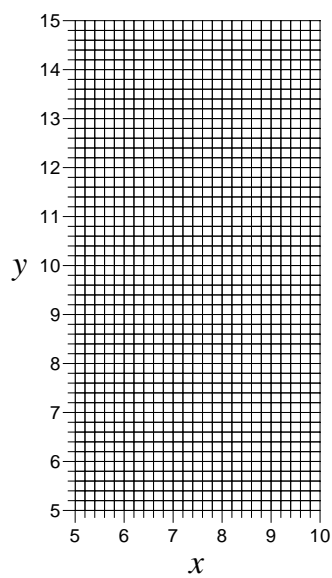
Figure 5.4. Domain mesh of Ω (coarse grid).
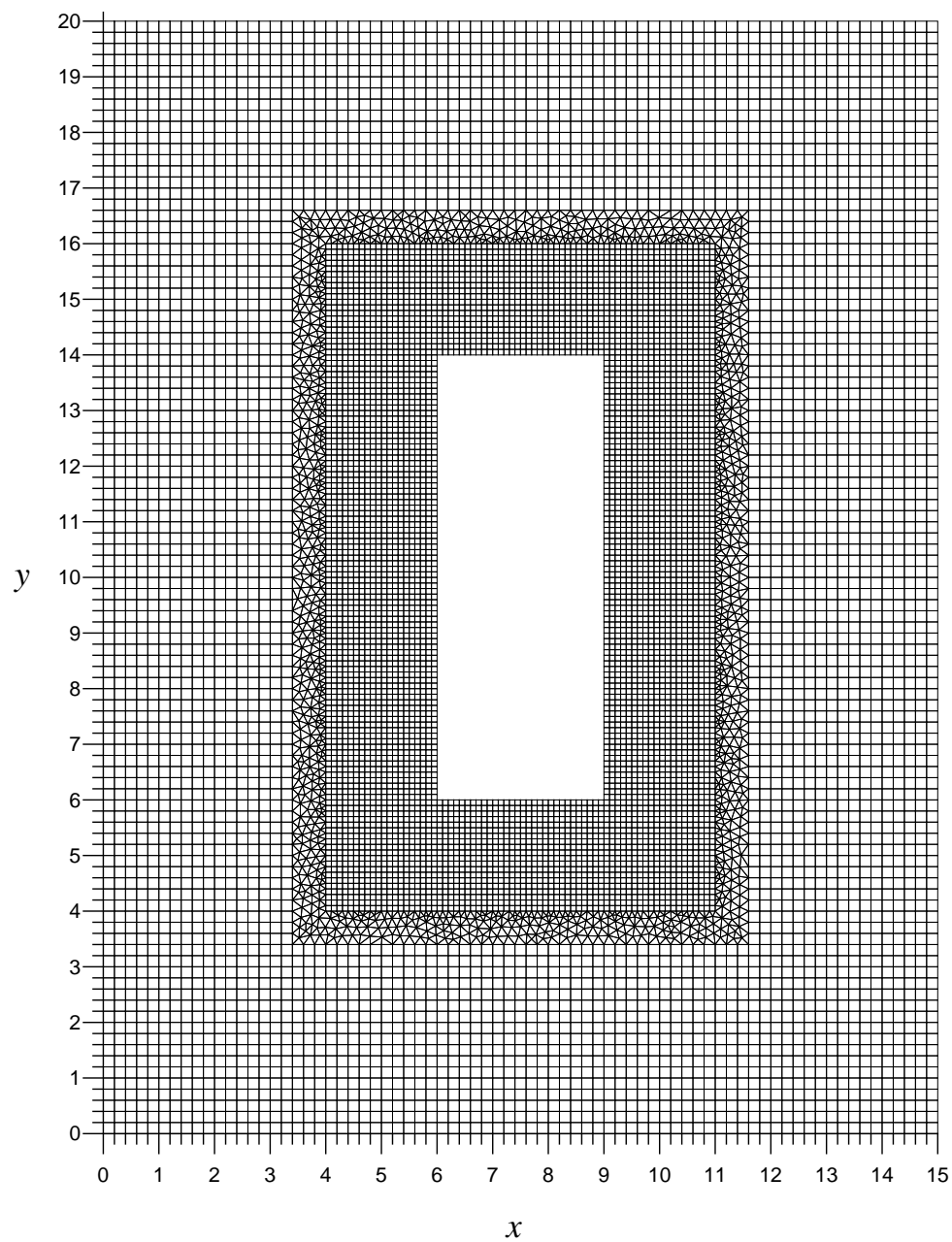
Figure 5.5. Domain mesh of $\Omega_0 - \mathcal{A}$ (coarse grid).

The measurement points at the corners of rectangular are shared by each sides and therefore the total number of independent measuring points is 220. Domain $(\Omega_0 - \mathcal{A})$ consists of two types of elements which are serendipity type of rectangular element and quadratic triangular element, see figure 4.3. The reason these two types of elements are combined, is because we need to get a smooth data of light intensity on Ω domain when we compute the forward exterior problem. Hence the area between $\partial\mathcal{A}$ and $\partial\Omega$ must be dense in order to filter the noise. And we use quadratic triangular element, see figure 4.3(b), to gradually change the dense grid to a coarse-grid. There are totally 13,282 elements in $(\Omega_0 - \mathcal{A})$, see figure 5.5.

Notice that the interior boundary of $\Omega_0 - \mathcal{A}$ is very dense but $\partial\mathcal{A}$ is not. When we assign the boundary of $\partial\mathcal{A}$ to $\partial(\Omega_0 - \mathcal{A})$, we use the linear interpolation on $\partial\mathcal{A}$ to assign the nodes of $\partial\mathcal{A}$ to the nodes on $\partial(\Omega_0 - \mathcal{A})$ that is not correspond to $\partial\mathcal{A}$. After the exterior forward problem is computed, we assign the solution on $\Omega_0 - \mathcal{A}$ to $\partial\Omega$ only at the corresponding point between $\Omega_0 - \mathcal{A}$ and $\partial\Omega$.

The reconstruction of same examples as in section 4.2 with these coarse-grids in the same machine are shown in figure 5.6 for example #1 and figure 5.7 for example #2. The average computation time of using coarse-grid are shown in table 5.2. We

Table 5.2. Computation time for results in section 4.2 in coarse grid

Example No.	Forward exterior problem	Inverse problem	Total time
1	0 min. 33 sec.	1 min. 39 sec.	2 min. 12 sec.
2	0 min. 32 sec.	1 min. 36 sec.	2 min. 8 sec.

can reduce a large amount of computation time by obtaining the similar results of reconstruction by using coarse-grid. This show that our algorithm are stable.
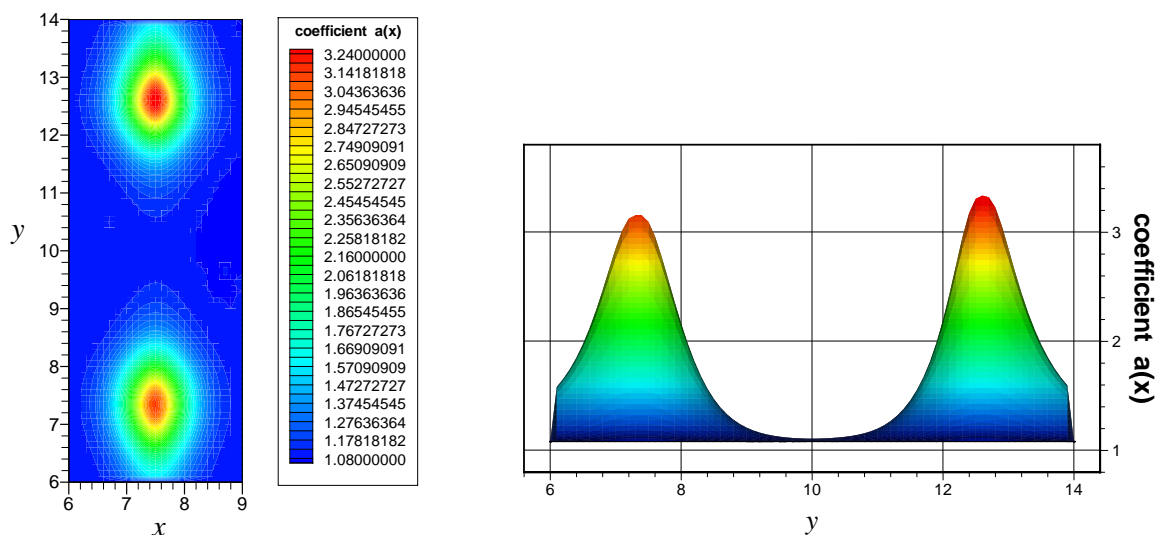
Peak value of left inclusion is 3.149 and right inclusion is 3.329.

(a)
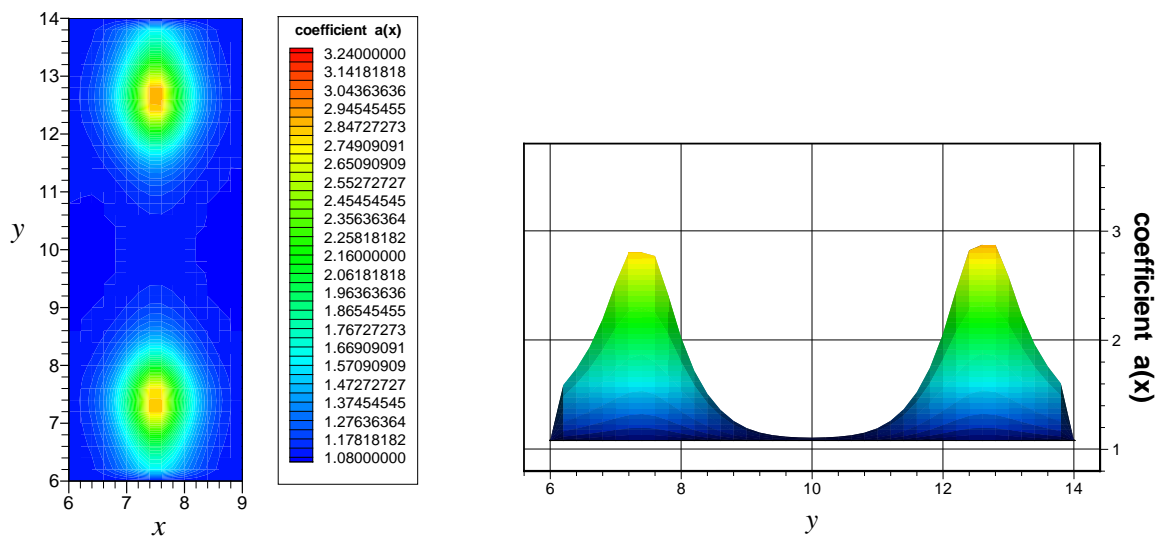
Peak value of left inclusion is 2.799 and right inclusion is 2.871.

(b)

Figure 5.6. (a) The reconstruction with 2% noise of example #1 in dense-grid. (b) The reconstruction with 2% noise of example #1 in coarse-grid.
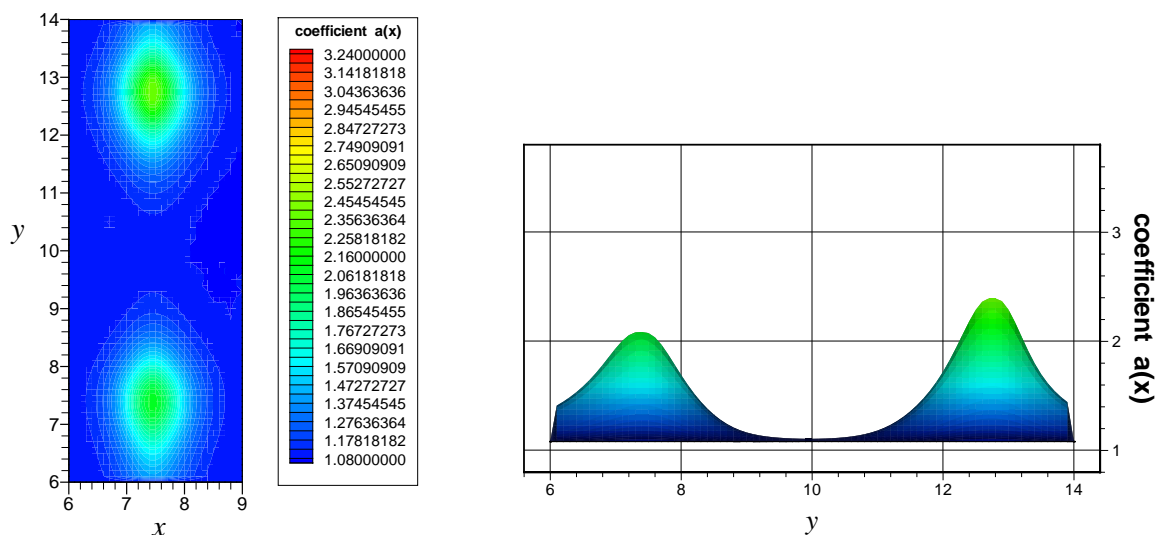
Peak value of left inclusion is 2.081 and right inclusion is 2.389.

(a)
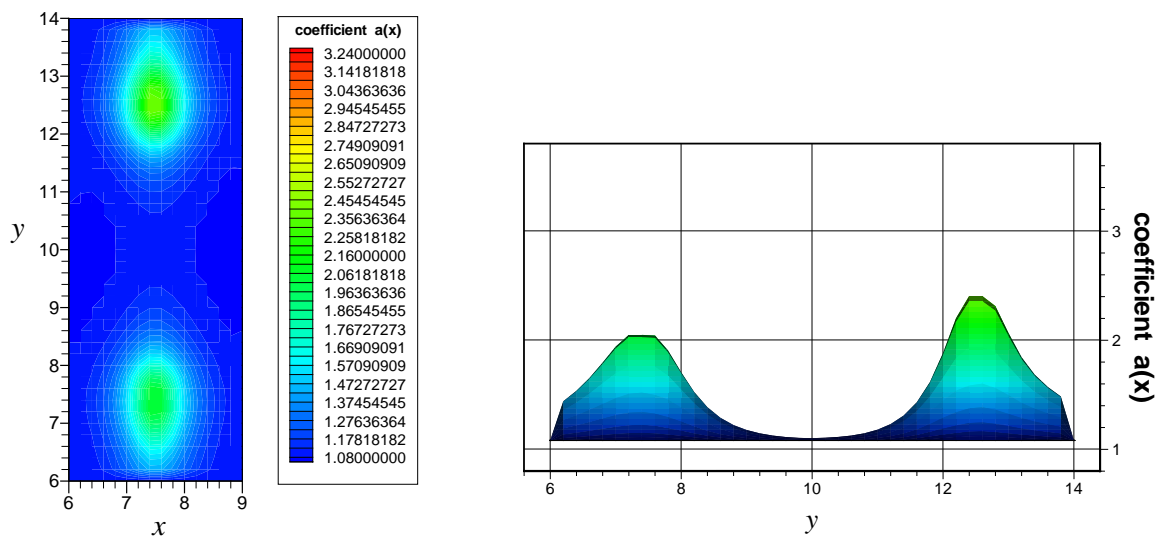
Peak value of left inclusion is 2.045 and right inclusion is 2.400.

(b)

Figure 5.7. (a) The reconstruction with 2% noise of example #2 in dense-grid. (b) The reconstruction with 2% noise of example #2 in coarse-grid.

5.2.2   Noise Level

We further carried on our numerical experiments with several noise level. As is known, when matching fluid is used in experiments, the light intensity at the measurement side should be much lower than without matching fluid. The noise level 4%, 6%, 8% and 10% are perform in our numerical experiments, see figure 5.8, 5.9, 5.10 and 5.11, respectively, for the reconstruction results.

As shown in those figures, we can see that the peak of the inclusion may get deteriorate, but the locations of the reconstructed inclusions are still correct.

5.2.3   Location of Inclusions

The location of inclusion may vary in different location in domain of interest $\mathcal{A}$. In this section we has shown the reconstruction of same type of inclusion as example #1 but different locations.

Figure 5.12(a) shows the original of example #3, we had moved the top inclusion a little further from the top boundary. The reconstruction, see figure 5.12(b), shows that when the inclusion locates far from the boundary, its peak value is not reconstructed well but the locations of the reconstructed inclusions are still correct.

Figure 5.13(a) shows the original of example #4, we had moved those two inclusion close to each other. The reconstruction, see figure 5.13(b), shows that those two inclusion will merge to each other where the one that is far from the boundary will merge to the one that close to the boundary and their peak value are not reconstructed well but the locations of the reconstructed inclusions are still correct.
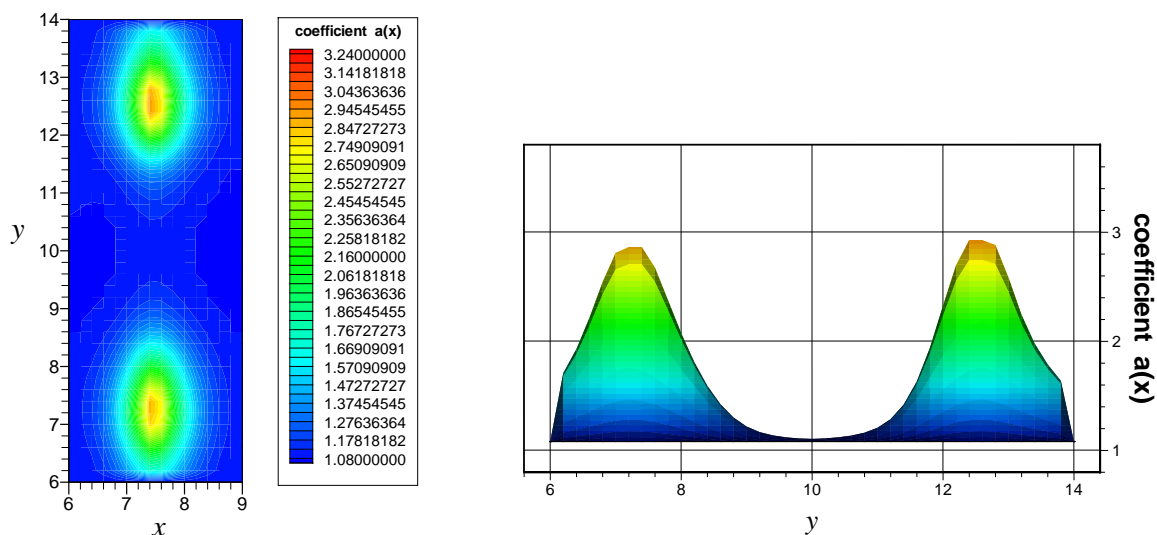
Peak value of left inclusion is 2.857 and right inclusion is 2.919.

(a)
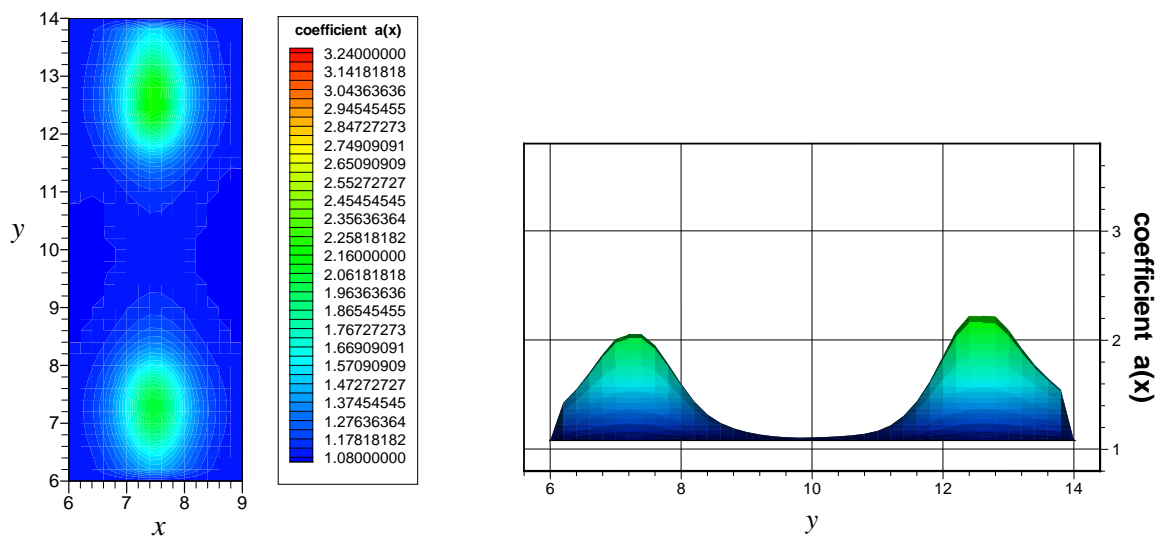
Peak value of left inclusion is 2.047 and right inclusion is 2.219.

(b)

Figure 5.8. (a) The reconstruction with 4% noise of example #1 in coarse-grid. (b) The reconstruction with 4% noise of example #2 in coarse-grid.
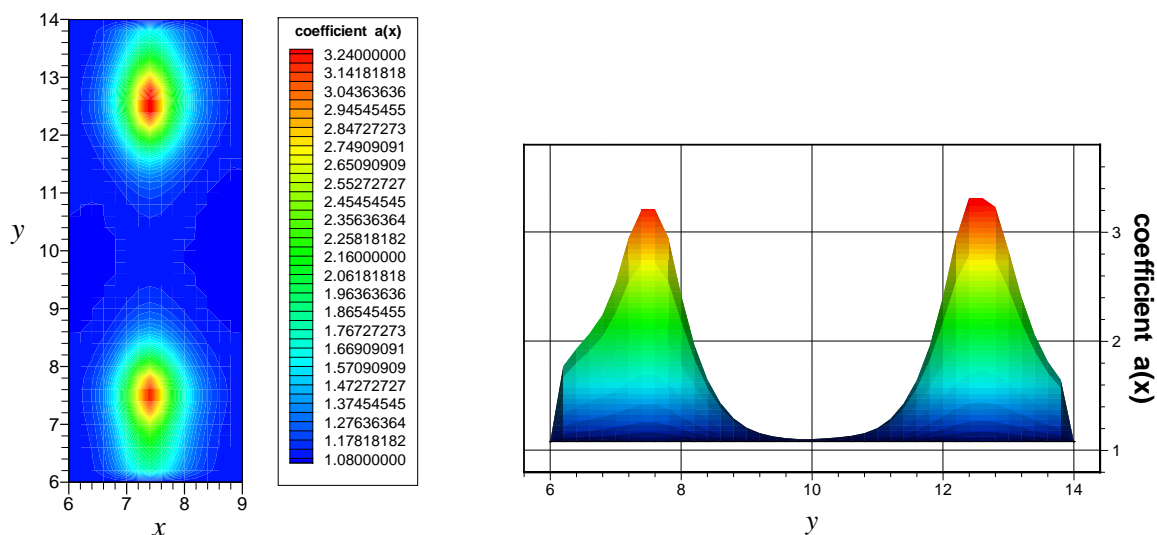
Peak value of left inclusion is 3.20 and right inclusion is 3.307.

(a)
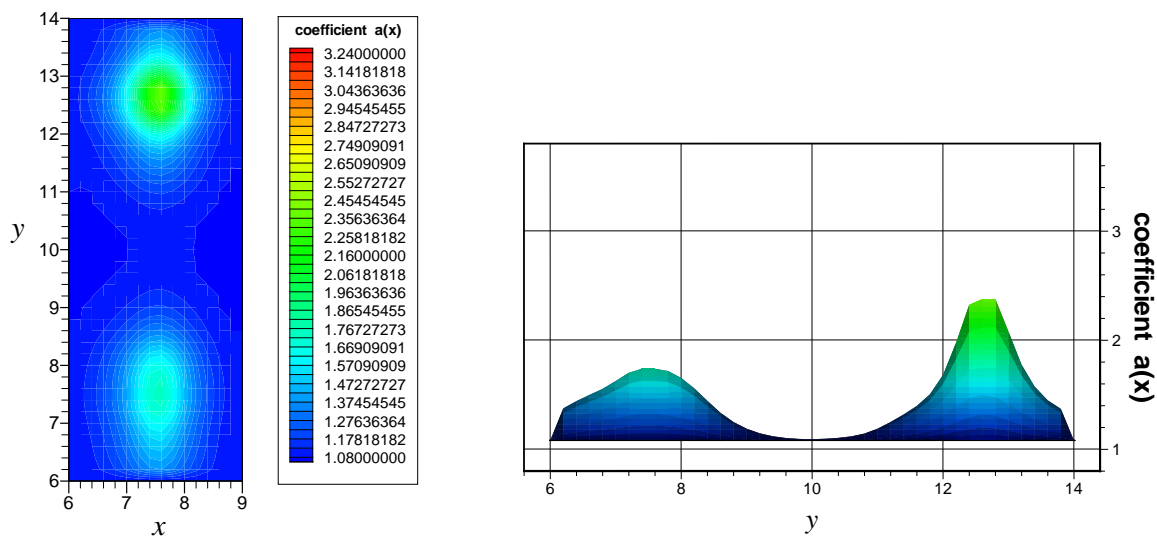
Peak value of left inclusion is 1.735 and right inclusion is 2.373.

(b)

Figure 5.9. (a) The reconstruction with 6% noise of example #1 in coarse-grid. (b) The reconstruction with 6% noise of example #2 in coarse-grid.
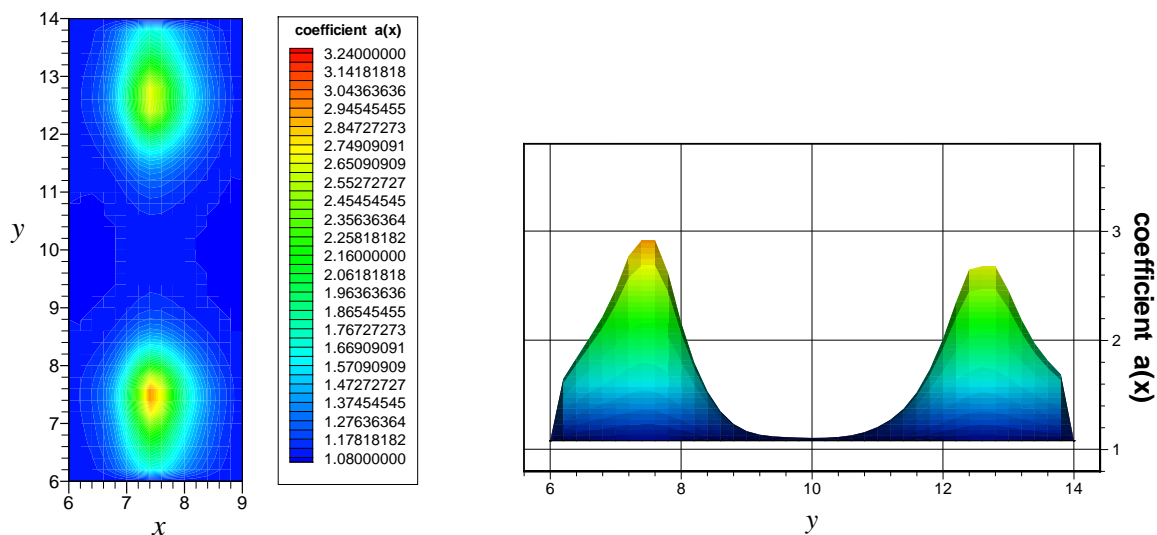
Peak value of left inclusion is 2.913 and right inclusion is 2.674.

(a)
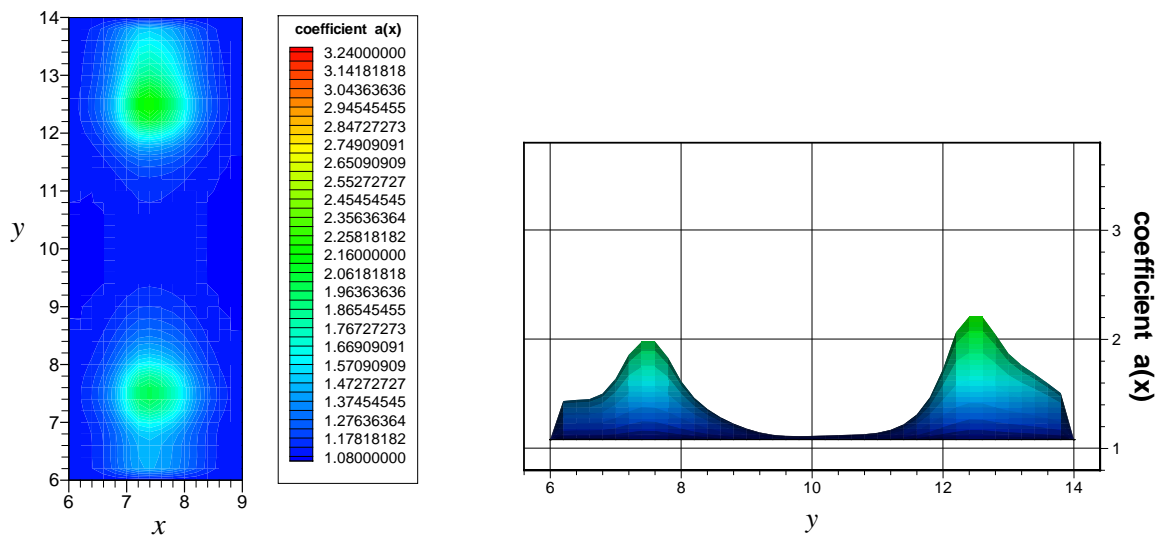
Peak value of left inclusion is 1.977 and right inclusion is 2.204.

(b)

Figure 5.10. (a) The reconstruction with 8% noise of example #1 in coarse-grid. (b) The reconstruction with 8% noise of example #2 in coarse-grid.
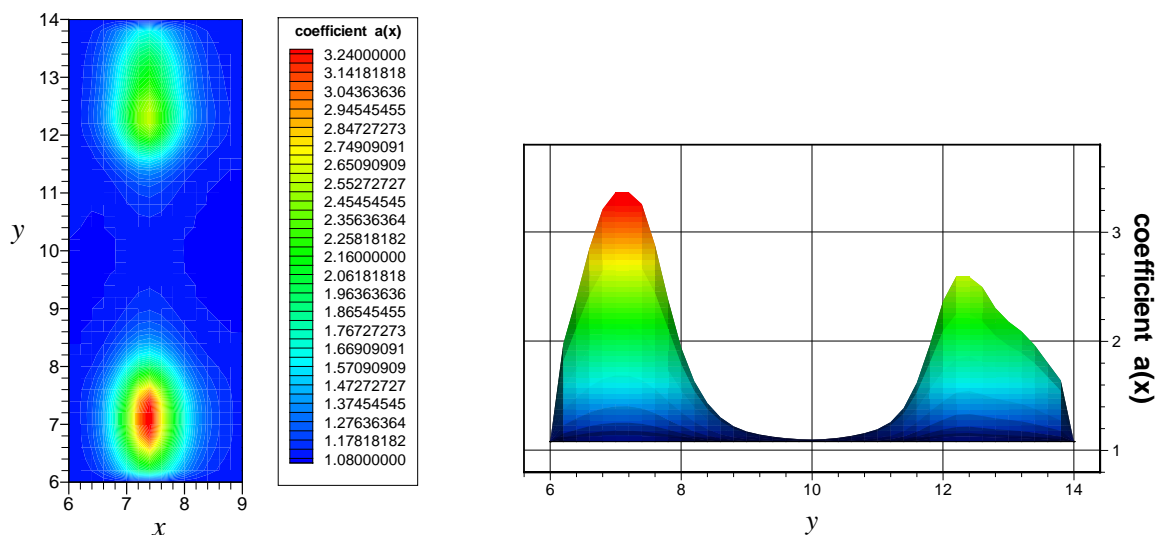
Peak value of left inclusion is 3.358 and right inclusion is 2.587.

(a)
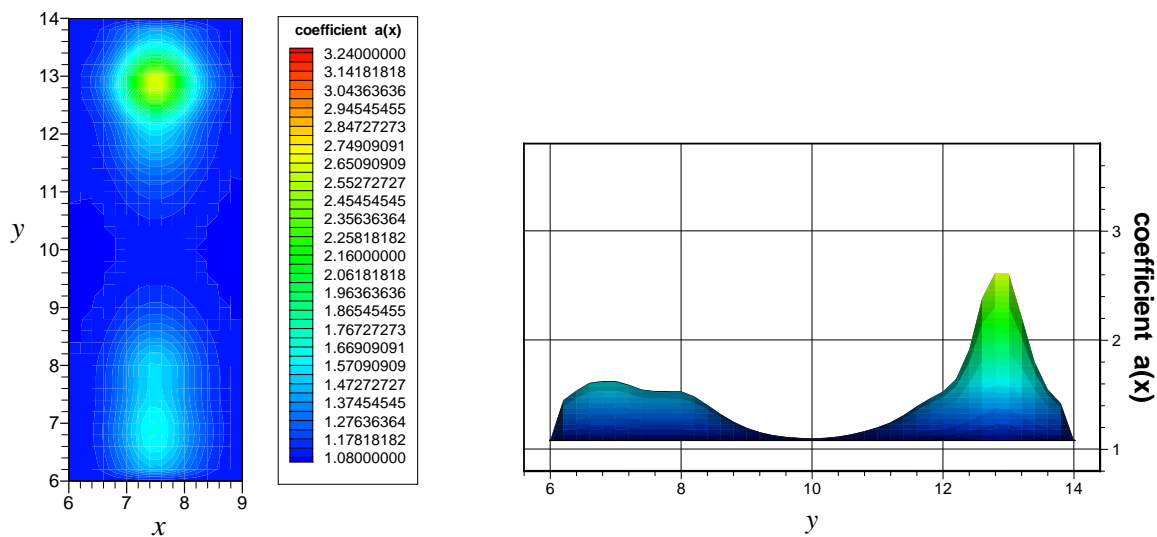
Peak value of left inclusion is 1.624 and right inclusion is 2.615.

(b)

Figure 5.11. (a) The reconstruction with 10% noise of example #1 in coarse-grid. (b) The reconstruction with 10% noise of example #2 in coarse-grid.
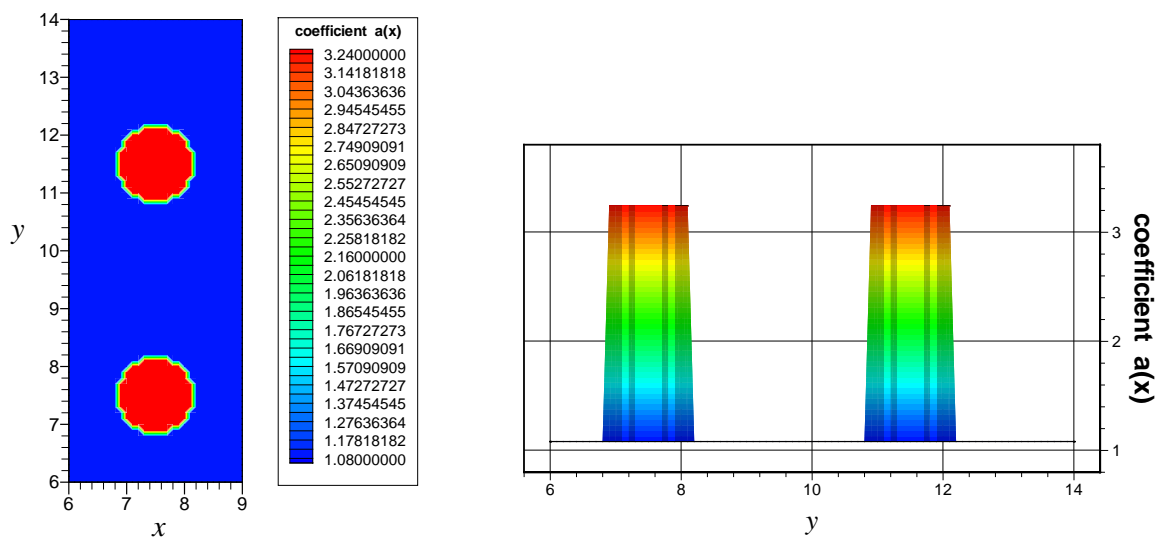
Peak value of left inclusion is 3.24 and right inclusion is 3.24.

(a)
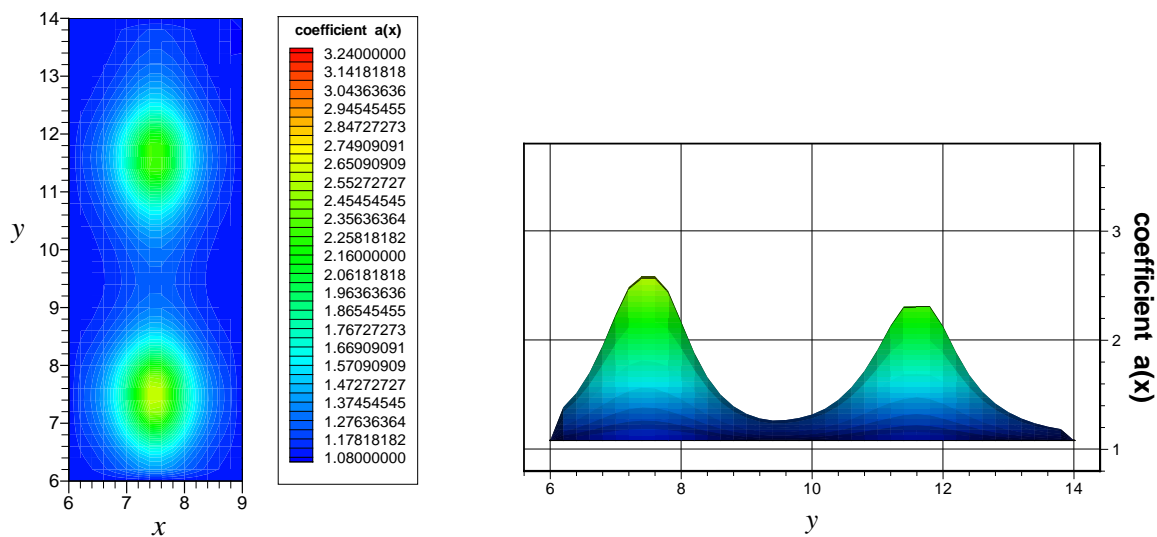
Peak value of left inclusion is 2.582 and right inclusion is 2.307.

(b)

Figure 5.12. (a) Displays the original coefficient $a(\boldsymbol{x})$ of example #3. (b) Shows its reconstruction result with 2% noise in coarse-grid.
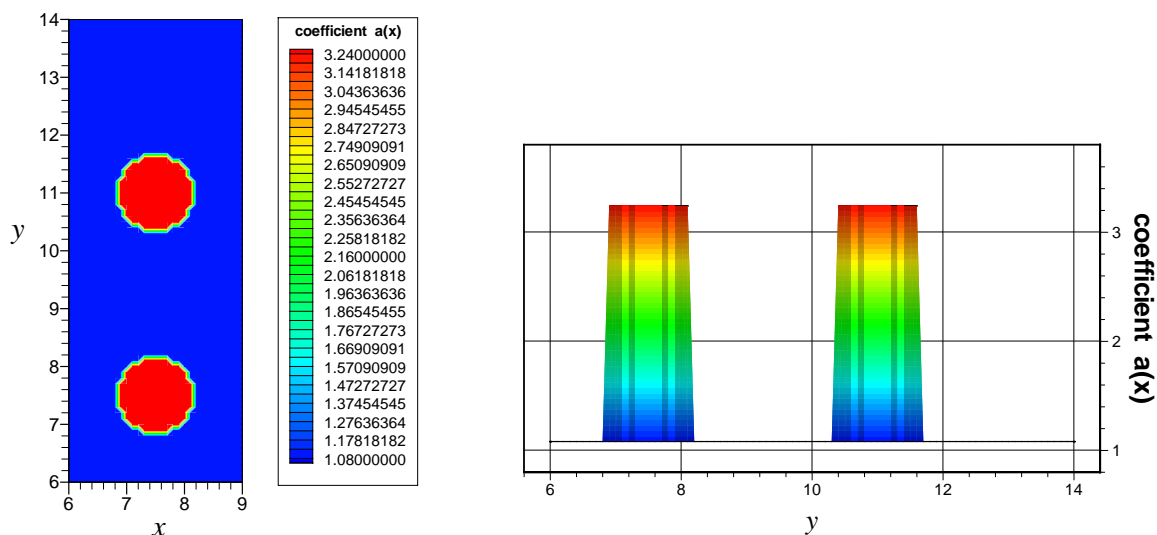
Peak value of left inclusion is 3.24 and right inclusion is 3.24.

(a)
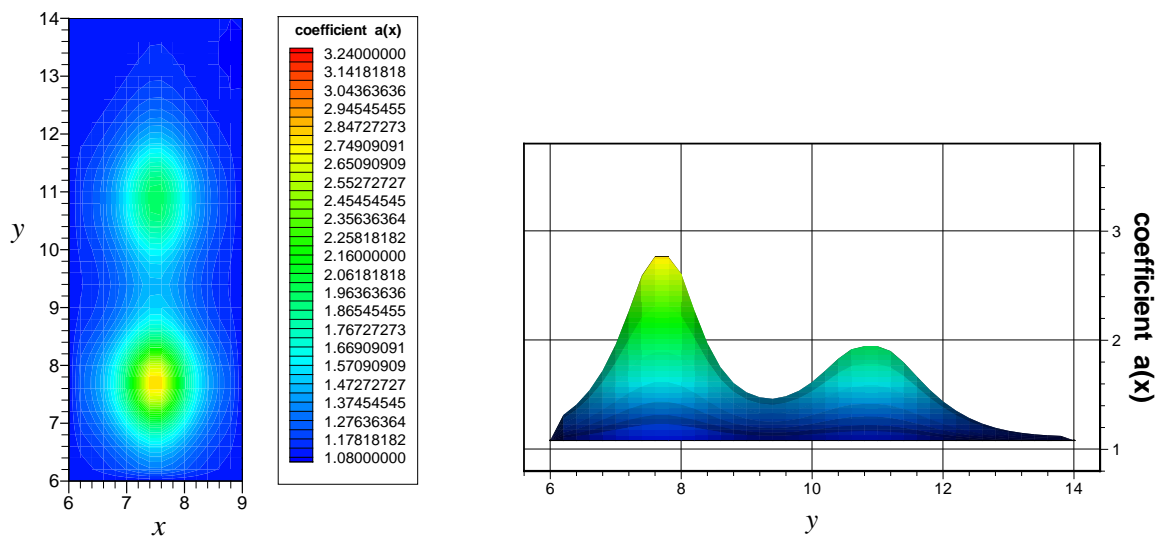
Peak value of left inclusion is 2.763 and right inclusion is 1.941.

(b)

Figure 5.13. (a) Displays the original coefficient $a(\boldsymbol{x})$ of example #4. (b) Shows its reconstruction result with 2% noise in coarse-grid.

APPENDIX A

DETAILS OF PROVING THEOREM 2.3.2

In this appendix, we present the proof of theorem 2.3.2 again by showing the derivation of each inequality.

A.1 Theorem 2.3.2

Let $\Omega \subset \mathbb{R}^2$ be a convex bounded domain with the boundary $\partial\Omega \in C^{2+\alpha}$. Suppose that an approximation v_∞ for the tail is constructed in such a way that

$$\|v_\infty\|_{C^{2+\alpha}(\overline{\Omega})} \leq \xi, \tag{A.1}$$

where $\xi \in (0,1)$ is a sufficient small number and that this function v_∞ is used in (2.33),(2.35) and (2.36). Denote $\eta = \max\{\sigma, h, \xi\}$, σ is noise level of data and h is step size, and suppose that the number $Nh = \overline{s} - \underline{s}$ is such that

$$Nh < \frac{1}{20KM^*}. \tag{A.2}$$

Then there exists a sufficiently small number $\eta_0 = \eta_0(K(M^*, \Omega), M^*, c, \underline{s}, \overline{s}) \in (0,1)$ such that for all $\eta \in (0, \eta_0)$ and for every integer $n \in [0, N-1]$ the following estimates hold

$$\|q_n^s - q_n^*\|_{C^{2+\alpha}(\overline{\Omega})} \leq KM^*(20\eta), \tag{A.3}$$

$$\|q_n^s\|_{C^{2+\alpha}(\overline{\Omega})} \leq 2M. \tag{A.4}$$

A.2 Proof of Theorem 2.3.2

This proof basically consists in estimating differences between our constructed functions $q_{n,k}^s$, and function q_n^*. We are doing this using the Schauder theorem. In this proof we assume that $\eta \in (0, \eta_0)$. Denote

$$\tilde{q}_{n,k}(\boldsymbol{x}) = q_{n,k}^s(\boldsymbol{x}) - q_n^*(\boldsymbol{x}), \quad \tilde{v}_\infty(\boldsymbol{x}) = v_\infty(\boldsymbol{x}) - \overline{v}^*(\boldsymbol{x}),$$

$$\tilde{\psi}_n(\boldsymbol{x}) = \psi_n^s(\boldsymbol{x}) - \psi_n^*(\boldsymbol{x}), \quad \tilde{T}_n(\boldsymbol{x}) = T_n(\boldsymbol{x}) - T_n^*(\boldsymbol{x}). \tag{A.5}$$

Note that, in this theorem $\|\cdot\|$ is equivalent to $\|\cdot\|_{C^{2+\alpha}(\overline{\Omega})}$. The proof basically consists in estimating these differences.

First we show the approximation of T_n, T_n^* and $\tilde{T}_n$. For $n = 1$ we have

$$\|T_1\| = \|v_\infty\| \leq \xi \quad , \quad \|T_1^*\| = \|\bar{v}^*\| \leq \xi \quad \text{and}$$

$$\|\tilde{T}_1\| = \|v_\infty - \bar{v}^*\| \leq \|v_\infty\| + \|\bar{v}^*\| = 2\xi \,.$$

And for $n \geq 2$ we have

$$
\begin{aligned}
\|T_n\| &= \left\| \frac{h}{2} \left(\tilde{q}_0 + 2\sum_{j=1}^{n-2} \tilde{q}_j + \tilde{q}_{n-1} \right) + \frac{h}{2} \left(q_0^* + 2\sum_{j=1}^{n-2} q_j^* + q_{n-1}^* \right) - v_\infty \right\| \\
&\leq h\sum_{j=0}^{n-1} \|\tilde{q}_j\| + h\sum_{j=0}^{n-1} \|q_j^*\| + \|v_\infty\| \\
&\leq h\sum_{j=0}^{n-1} \|\tilde{q}_j\| + hn \max_{0\leq j\leq n-1} \|q_j^*\| + \xi \\
&\leq h\sum_{j=0}^{n-1} \|\tilde{q}_j\| + S^* \max_{0\leq j\leq n-1} \|q_j^*\| + \xi \,, \\
\|T_n^*\| &= \left\| \frac{h}{2} \left(q_0^* + 2\sum_{j=1}^{n-2} q_j^* + q_{n-1}^* \right) - \bar{v}^* \right\| \\
&\leq h\sum_{j=0}^{n-1} \|q_j^*\| + \|\bar{v}^*\| \\
&\leq hn \max_{0\leq j\leq n-1} \|q_j^*\| + \xi \\
&\leq S^* \max_{0\leq j\leq n-1} \|q_j^*\| + \xi \quad \text{and} \\
\|\tilde{T}_n\| &= \|T_n - T_n^*\| \\
&= \left\| \frac{h}{2} \left(\tilde{q}_0 + 2\sum_{j=1}^{n-2} \tilde{q}_j + \tilde{q}_{n-1} \right) - \tilde{v}_\infty \right\| \\
&\leq h\sum_{j=0}^{n-1} \|\tilde{q}_j\| + \|v_\infty - \bar{v}^*\| \\
&\leq h\sum_{j=0}^{n-1} \|\tilde{q}_j\| + 2\xi \,.
\end{aligned}
$$

First, we estimate $\tilde{q}_0$. Subtract equation (2.45) from (2.33). We obtain

$$\Delta(q_0^s - q_0^*) + 2s_0^2[\nabla q_0^s \cdot \nabla v_\infty - \nabla q_0^* \cdot \nabla \bar{v}^*] + 4s_0[(\nabla v_\infty)^2 - (\nabla \bar{v}^*)^2]$$

$$= -\frac{2}{s_0}\Delta(v_\infty - \bar{v}^*)$$

$$\downarrow$$

$$\Delta\tilde{q}_0 + 2s_0^2[\nabla q_0^s \cdot \nabla v_\infty - \nabla q_0^*\nabla v_\infty + \nabla q_0^*\nabla v_\infty - \nabla q_0^* \cdot \nabla \bar{v}^*] + 4s_0\nabla(v_\infty - \bar{v}^*)\nabla(v_\infty + \bar{v}^*)$$

$$= -\frac{2}{s_0}\Delta(v_\infty - \bar{v}^*)$$

$$\downarrow$$

$$\Delta\tilde{q}_0 + 2s_0^2[\nabla\tilde{q}_0\nabla v_\infty + \nabla q_0^*\nabla(v_\infty - \bar{v}^*)] + 4s_0\nabla(v_\infty - \bar{v}^*)\nabla(v_\infty + \bar{v}^*)$$

$$= -\frac{2}{s_0}\Delta(v_\infty - \bar{v}^*)$$

$$\downarrow$$

$$\Delta\tilde{q}_0 + 2s_0^2\nabla\tilde{q}_0\nabla v_\infty = -2s_0^2\nabla q_0^*\nabla(v_\infty - \bar{v}^*)$$

$$-4s_0\nabla(v_\infty - \bar{v}^*)\nabla(v_\infty + \bar{v}^*) - \frac{2}{s_0}\Delta(v_\infty - \bar{v}^*). \tag{A.6}$$

Since $\|2s_0^2 v_\infty\| \leq 4\bar{s}^2\|\bar{v}^*\| \leq M^*$, by Schauder theorem, we have

$$
\begin{aligned}
\|\tilde{q}_0\| &\leq K\left[\|\tilde{\psi}_0\| + 2s_0^2\|q_0^*\|\|v_\infty - \bar{v}^*\| + 4s_0\|v_\infty - \bar{v}^*\|\|v_\infty + \bar{v}^*\| + \frac{2}{s_0}\|v_\infty - \bar{v}^*\|\right] \\
&\leq K\left[C_1(\sigma + h) + M^* \cdot \xi + 4s_0 \cdot 2\xi \cdot 2\xi + \frac{2}{s_0} \cdot 2\xi\right] \\
&\leq K\left[M^*(\sigma + h) + M^*\xi + M^*\xi + M^*\xi\right] \\
&\leq KM^*\left[\sigma + h + \xi + \xi + \xi\right] \\
&\leq KM^*(5\eta)
\end{aligned}
$$

And hence

$$\|q_0^s\| = \|\tilde{q}_0 + q_0^*\| \leq \|\tilde{q}_0\| + \|q_0^*\| \leq KM^*(5\eta) + M^* \leq 2M^*. \tag{A.7}$$

Second, we estimate $\tilde{q}_{1,1}$. Set in equation (2.46) $n = 1$ and subtract it from (2.35) at $k = 1$, recalling that $q_{1,0}^s = q_0^s$. We obtain

$$\Delta[q_{1,1}^s - q_1^*] - A_1[\nabla q_{1,1}^s \nabla q_0^s - (\nabla q_1^*)^2]$$

$$-B_1[\nabla q_{1,1}^s \nabla q_0^s - \nabla q_1^* \nabla q_0^*] - C_1[\nabla q_{1,1}^s \nabla T_1 - \nabla q_1^* \nabla T_1^*]$$

$$= D_1\Delta[q_0^s - q_0^*] + E_1\Delta[T_1 - T_1^*] - F_1[(\nabla q_0^s)^2 - (\nabla q_0^*)^2]$$

$$-G_1[\nabla q_0^s \nabla T_1 - \nabla q_0^* \nabla T_1^*] - H_1[(\nabla T_1)^2 - (\nabla T_1^*)^2] - R_1$$

$$\downarrow$$

$$\Delta\tilde{q}_{1,1} - A_1[\nabla(\tilde{q}_{1,1} + q_1^*)\nabla(\tilde{q}_0 + q_0^*) - (\nabla q_1^*)^2]$$

$$-B_1[\nabla(\tilde{q}_{1,1} + q_1^*)\nabla(\tilde{q}_0 + q_0^*) - \nabla q_1^* \nabla q_0^*] - C_1[\nabla q_{1,1}^s \nabla T_1 - \nabla q_1^* \nabla T_1 + \nabla q_1^* \nabla T_1 - \nabla q_1^* \nabla T_1^*]$$

$$= D_1\Delta\tilde{q}_0 + E_1\Delta\tilde{T}_1 - F_1[(\nabla q_0^s - \nabla q_0^*)(\nabla q_0^s + \nabla q_0^*)]$$

$$-G_1[\nabla q_0^s \nabla T_1 - \nabla q_0^* \nabla T_1 + \nabla q_0^* \nabla T_1 - \nabla q_0^* \nabla T_1^*] - H_1[(\nabla T_1 - \nabla T_1^*)(\nabla T_1 + \nabla T_1^*)] - R_1$$

$$\downarrow$$

$$\Delta\tilde{q}_{1,1} - A_1[\nabla\tilde{q}_{1,1}\nabla\tilde{q}_0 + \nabla\tilde{q}_{1,1}\nabla q_0^* + \nabla q_1^* \nabla\tilde{q}_0 + \nabla q_1^* \nabla q_0^* - \nabla q_1^* \nabla q_1^*]$$

$$-B_1[\nabla\tilde{q}_{1,1}\nabla\tilde{q}_0 + \nabla\tilde{q}_{1,1}\nabla q_0^* + \nabla q_1^* \nabla\tilde{q}_0 + \nabla q_1^* \nabla q_0^* - \nabla q_1^* \nabla q_0^*] - C_1[\nabla\tilde{q}_{1,1}\nabla T_1 + \nabla q_1^* \nabla\tilde{T}_1]$$

$$= D_1\Delta\tilde{q}_0 + E_1\Delta\tilde{T}_1 - F_1\nabla\tilde{q}_0(\nabla\tilde{q}_0 + \nabla q_0^* + \nabla q_0^*)$$

$$-G_1[\nabla\tilde{q}_0\nabla T_1 + \nabla q_0^* \nabla\tilde{T}_1] - H_1\nabla\tilde{T}_1(\nabla T_1 + \nabla T_1^*) - R_1$$

$$\downarrow$$

$$\Delta \tilde{q}_{1,1} - A_1 [\nabla \tilde{q}_{1,1} \nabla \tilde{q}_0 + \nabla \tilde{q}_{1,1} \nabla q_0^* + \nabla q_1^* \nabla \tilde{q}_0 + \nabla q_1^* \nabla q_0^* - \nabla q_1^* \nabla q_1^*]$$

$$-B_1 [\nabla \tilde{q}_{1,1} \nabla \tilde{q}_0 + \nabla \tilde{q}_{1,1} \nabla q_0^* + \nabla q_1^* \nabla \tilde{q}_0] - C_1 [\nabla \tilde{q}_{1,1} \nabla T_1 + \nabla q_1^* \nabla \tilde{T}_1]$$

$$= D_1 \Delta \tilde{q}_0 + E_1 \Delta \tilde{T}_1 - F_1 \nabla \tilde{q}_0 (\nabla \tilde{q}_0 + 2 \nabla q_0^*)$$

$$-G_1 [\nabla \tilde{q}_0 \nabla T_1 + \nabla q_0^* \nabla \tilde{T}_1] - H_1 \nabla \tilde{T}_1 (\nabla T_1 + \nabla T_1^*) - R_1$$

$$\downarrow$$

$$\Delta \tilde{q}_{1,1} - A_1 \nabla \tilde{q}_{1,1} \nabla \tilde{q}_0 - A_1 \nabla \tilde{q}_{1,1} \nabla q_0^* - B_1 \nabla \tilde{q}_{1,1} \nabla \tilde{q}_0 - B_1 \nabla \tilde{q}_{1,1} \nabla q_0^* - C_1 \nabla \tilde{q}_{1,1} \nabla T_1$$

$$= A_1 \nabla q_1^* \nabla \tilde{q}_0 + A_1 \nabla q_1^* \nabla q_0^* - A_1 \nabla q_1^* \nabla q_1^* + B_1 \nabla q_1^* \nabla \tilde{q}_0 + C_1 \nabla q_1^* \nabla \tilde{T}_1$$

$$+ D_1 \Delta \tilde{q}_0 + E_1 \Delta \tilde{T}_1 - F_1 \nabla \tilde{q}_0 \nabla \tilde{q}_0 - 2 F_1 \nabla \tilde{q}_0 \nabla q_0^*$$

$$- G_1 \nabla \tilde{q}_0 \nabla T_1 - G_1 \nabla q_0^* \nabla \tilde{T}_1 - H_1 \nabla \tilde{T}_1 \nabla T_1 - H_1 \nabla \tilde{T}_1 \nabla T_1^* - R_1 \,. \qquad \text{(A.8)}$$

Since

$$\|A_1 \nabla \tilde{q}_0\| \leq h \bar{s}^2 \|\tilde{q}_0\| \leq M^*$$

$$\|A_1 \nabla q_0^*\| \leq h \bar{s}^2 \|q_0^*\| \leq M^*$$

$$\|B_1 \nabla \tilde{q}_0\| \leq 2 h \bar{s}^2 \|\tilde{q}_0\| \leq M^*$$

$$\|B_1 \nabla q_0^*\| \leq 2 h \bar{s}^2 \|q_0^*\| \leq M^*$$

$$\|C_1 \nabla T_1\| \leq 8 \bar{s}^2 \|T_1\| \leq M^* ,$$

by Schauder theorem, we have

$$\|\tilde{q}_{1,1}\| \leq K \Big[\|\tilde{\psi}_1\| + \|A_1 \nabla q_1^* \nabla \tilde{q}_0\| + \|A_1 \nabla q_1^* \nabla q_0^*\| + \|A_1 \nabla q_1^* \nabla q_1^*\| + \|B_1 \nabla q_1^* \nabla \tilde{q}_0\|$$

$$+ \|C_1 \nabla q_1^* \nabla \tilde{T}_1\| + \|D_1 \Delta \tilde{q}_0\| + \|E_1 \Delta \tilde{T}_1\| + \|F_1 \nabla \tilde{q}_0 \nabla \tilde{q}_0\| + \|2 F_1 \nabla \tilde{q}_0 \nabla q_0^*\|$$

$$+ \|G_1 \nabla \tilde{q}_0 \nabla T_1\| + \|G_1 \nabla q_0^* \nabla \tilde{T}_1\| + \|H_1 \nabla \tilde{T}_1 \nabla T_1\| + \|H_1 \nabla \tilde{T}_1 \nabla T_1^*\| + \|R_1\| \Big]$$

$$\|\tilde{q}_{1,1}\| \leq K\Big[C_1(\sigma + h) + h\overline{s}^2\|q_1^*\|\|\tilde{q}_0\| + h\overline{s}^2\|q_1^*\|\|q_0^*\| + h\overline{s}^2\|q_1^*\|\|q_1^*\| + 2h\overline{s}^2\|q_1^*\|\|\tilde{q}_0\|$$

$$+4\overline{s}^2\|q_1^*\|\|\tilde{T}_1\| + h\|\tilde{q}_0\| + \|\tilde{T}_1\| + h\overline{s}^2\|\tilde{q}_0\|\|\tilde{q}_0\| + 2h\overline{s}^2\|\tilde{q}_0\|\|q_0^*\| + h\overline{s}^2\|\tilde{q}_0\|\|T_1\|$$

$$+h\overline{s}^2\|q_0^*\|\|\tilde{T}_1\| + \overline{s}^2\|\tilde{T}_1\|\|T_1\| + \overline{s}^2\|\tilde{T}_1\|\|T_1^*\| + C^*h\Big]$$

$$\leq K\Big[M^*(\sigma + h) + M^*h + M^*h + M^*h + M^*h + M^*\xi + M^*h + M^*\xi + M^*h$$

$$+M^*h + M^*h + M^*h + M^*\xi + M^*\xi + M^*h\Big]$$

$$\leq KM^*\Big[\sigma + h + h + h + h + h + \xi + h + \xi + h + h + h + h + \xi + \xi + h\Big]$$

$$\leq KM^*(16\eta).$$

Hence

$$\|q_{1,1}^s\| = \|\tilde{q}_{1,1} + q_1^*\| \leq \|\tilde{q}_{1,1}\| + \|q_1^*\| \leq KM^*(16\eta) + M^* \leq 2M^*. \qquad (A.9)$$

Now we estimate $\tilde{q}_{1,k}$. Assume that

$$\|\tilde{q}_{1,k-1}\| \leq KM^*(16\eta) \quad \text{and} \quad \|q_{1,k-1}^s\| \leq 2M^*. \qquad (A.10)$$

Set in equation (2.46) $n = 1$ and subtract it from (2.35). We obtain

$$\Delta[q_{1,k}^s - q_1^*] - A_1[\nabla q_{1,k}^s \nabla q_{1,k-1}^s - (\nabla q_1^*)^2]$$

$$-B_1[\nabla q_{1,k}^s \nabla q_0^s - \nabla q_1^* \nabla q_0^*] - C_1[\nabla q_{1,k}^s \nabla T_1 - \nabla q_1^* \nabla T_1^*]$$

$$= D_1 \Delta[q_0^s - q_0^*] + E_1 \Delta[T_1 - T_1^*] - F_1[(\nabla q_0^s)^2 - (\nabla q_0^*)^2]$$

$$-G_1[\nabla q_0^s \nabla T_1 - \nabla q_0^* \nabla T_1^*] - H_1[(\nabla T_1)^2 - (\nabla T_1^*)^2] - R_1$$

$$\downarrow$$

$$\Delta \tilde{q}_{1,k} - A_1 \nabla \tilde{q}_{1,k} \nabla \tilde{q}_{1,k-1} - A_1 \nabla \tilde{q}_{1,k} \nabla q_0^* - B_1 \nabla \tilde{q}_{1,k} \nabla \tilde{q}_0 - B_1 \nabla \tilde{q}_{1,k} \nabla q_0^* - C_1 \nabla \tilde{q}_{1,k} \nabla T_1$$

$$= A_1 \nabla q_1^* \nabla \tilde{q}_{1,k-1} + A_1 \nabla q_1^* \nabla q_0^* - A_1 \nabla q_1^* \nabla q_1^* + B_1 \nabla q_1^* \nabla \tilde{q}_0 + C_1 \nabla q_1^* \nabla \tilde{T}_1$$

$$+ D_1 \Delta \tilde{q}_0 + E_1 \Delta \tilde{T}_1 - F_1 \nabla \tilde{q}_0 \nabla \tilde{q}_0 - 2 F_1 \nabla \tilde{q}_0 \nabla q_0^*$$

$$- G_1 \nabla \tilde{q}_0 \nabla T_1 - G_1 \nabla q_0^* \nabla \tilde{T}_1 - H_1 \nabla \tilde{T}_1 \nabla T_1 - H_1 \nabla \tilde{T}_1 \nabla T_1^* - R_1 \,. \tag{A.11}$$

Since

$$
\begin{aligned}
\|A_1 \nabla \tilde{q}_{1,k-1}\| &\leq h \bar{s}^2 \|\tilde{q}_{1,k-1}\| \leq M^* \\
\|A_1 \nabla q_0^*\| &\leq h \bar{s}^2 \|q_0^*\| \leq M^* \\
\|B_1 \nabla \tilde{q}_0\| &\leq 2 h \bar{s}^2 \|\tilde{q}_0\| \leq M^* \\
\|B_1 \nabla q_0^*\| &\leq 2 h \bar{s}^2 \|q_0^*\| \leq M^* \\
\|C_1 \nabla T_1\| &\leq 8 \bar{s}^2 \|T_1\| \leq M^* \,,
\end{aligned}
$$

by Schauder theorem, we have

$$
\begin{aligned}
\|\tilde{q}_{1,k}\| &\leq K \Big[\|\tilde{\psi}_1\| + \|A_1 \nabla q_1^* \nabla \tilde{q}_{1,k-1}\| + \|A_1 \nabla q_1^* \nabla q_0^*\| + \|A_1 \nabla q_1^* \nabla q_1^*\| + \|B_1 \nabla q_1^* \nabla \tilde{q}_0\| \\
&\quad + \|C_1 \nabla q_1^* \nabla \tilde{T}_1\| + \|D_1 \Delta \tilde{q}_0\| + \|E_1 \Delta \tilde{T}_1\| + \|F_1 \nabla \tilde{q}_0 \nabla \tilde{q}_0\| + \|2 F_1 \nabla \tilde{q}_0 \nabla q_0^*\| \\
&\quad + \|G_1 \nabla \tilde{q}_0 \nabla T_1\| + \|G_1 \nabla q_0^* \nabla \tilde{T}_1\| + \|H_1 \nabla \tilde{T}_1 \nabla T_1\| + \|H_1 \nabla \tilde{T}_1 \nabla T_1^*\| + \|R_1\| \Big] \\
&\leq K \Big[C_1(\sigma + h) + h \bar{s}^2 \|q_1^*\| \|\tilde{q}_{1,k-1}\| + h \bar{s}^2 \|q_1^*\| \|q_0^*\| + h \bar{s}^2 \|q_1^*\| \|q_1^*\| + 2 h \bar{s}^2 \|q_1^*\| \|\tilde{q}_0\| \\
&\quad + 4 \bar{s}^2 \|q_1^*\| \|\tilde{T}_1\| + h \|\tilde{q}_0\| + \|\tilde{T}_1\| + h \bar{s}^2 \|\tilde{q}_0\| \|\tilde{q}_0\| + 2 h \bar{s}^2 \|\tilde{q}_0\| \|q_0^*\| + h \bar{s}^2 \|\tilde{q}_0\| \|T_1\| \\
&\quad + h \bar{s}^2 \|q_0^*\| \|\tilde{T}_1\| + \bar{s}^2 \|\tilde{T}_1\| \|T_1\| + \bar{s}^2 \|\tilde{T}_1\| \|T_1^*\| + C^* h \Big] \\
&\leq K \Big[M^*(\sigma + h) + M^* h + M^* h + M^* h + M^* h + M^* \xi + M^* h + M^* \xi + M^* h \\
&\quad + M^* h + M^* h + M^* h + M^* \xi + M^* \xi + M^* h \Big] \\
&\leq K M^* \Big[\sigma + h + h + h + h + h + \xi + h + \xi + h + h + h + h + \xi + \xi + h \Big] \\
&\leq K M^* (16 \eta) \,.
\end{aligned}
$$

Hence

$$|q^s_{1,k}\| = \|\tilde{q}_{1,k} + q^*_1\| \le \|\tilde{q}_{1,k}\| + \|q^*_1\| \le KM^*(16\eta) + M^* \le 2M^* \,. \tag{A.12}$$

And therefore we finally have

$$\|\tilde{q}_1\| \le KM^*(16\eta) \quad \text{and} \quad \|q^s_1\| \le 2M^* \,. \tag{A.13}$$

Now we estimate $\tilde{q}_{2,1}$. Set in equation (2.46) $n = 2$ and subtract it from (2.36) at $n = 2, k = 1$, recalling that $q^s_{2,0} = q^s_1$. We obtain

$$\Delta\tilde{q}_{2,1} - A_2\nabla\tilde{q}_{2,1}\nabla\tilde{q}_1 - A_2\nabla\tilde{q}_{2,1}\nabla q^*_1 - B_2\nabla\tilde{q}_{2,1}\nabla\tilde{q}_1 - B_2\nabla\tilde{q}_{2,1}\nabla q^*_1 - C_2\nabla\tilde{q}_{2,1}\nabla T_2$$

$$= A_2\nabla q^*_2\nabla\tilde{q}_1 + A_2\nabla q^*_2\nabla q^*_1 - A_2\nabla q^*_2\nabla q^*_2 + B_2\nabla q^*_2\nabla\tilde{q}_1 + C_2\nabla q^*_2\nabla\tilde{T}_2$$

$$+ D_2\Delta\tilde{q}_1 + E_2\Delta\tilde{T}_2 - F_2\nabla\tilde{q}_1\nabla\tilde{q}_1 - 2F_2\nabla\tilde{q}_1\nabla q^*_1$$

$$- G_2\nabla\tilde{q}_1\nabla T_2 - G_2\nabla q^*_1\nabla\tilde{T}_2 - H_2\nabla\tilde{T}_2\nabla T_2 - H_2\nabla\tilde{T}_2\nabla T^*_2 - R_2 \,. \tag{A.14}$$

Since

$$\|A_2\nabla\tilde{q}_1\| \le h\bar{s}^2\|\tilde{q}_{1,k-1}\| \le M^*$$

$$\|A_2\nabla q^*_1\| \le h\bar{s}^2\|q^*_1\| \le M^*$$

$$\|B_2\nabla\tilde{q}_1\| \le 2h\bar{s}^2\|\tilde{q}_1\| \le M^*$$

$$\|B_2\nabla q^*_1\| \le 2h\bar{s}^2\|q^*_1\| \le M^*$$

$$\|C_2\nabla T_2\| \le 4\bar{s}^2\|T_2\| \le 4\bar{s}^2\Big[Nh \cdot KM^*(16\eta) + \max_{0 \le j \le 1}\|q^*_j\| + \xi\Big]$$

$$\le 4\bar{s}^2\Big[\eta + \max_{0 \le j \le 1}\|q^*_j\| + \xi\Big] \le M^* \,,$$

by Schauder theorem, we have

$$
\begin{aligned}
\|\tilde{q}_{2,1}\| \;\leq\; & K\Big[\|\tilde{\psi}_2\| + \|A_2\nabla q_2^*\nabla\tilde{q}_1\| + \|A_2\nabla q_2^*\nabla q_1^*\| + \|A_2\nabla q_2^*\nabla q_2^*\| + \|B_2\nabla q_2^*\nabla\tilde{q}_1\| \\
& + \|C_2\nabla q_2^*\nabla\tilde{T}_2\| + \|D_2\Delta\tilde{q}_1\| + \|E_2\Delta\tilde{T}_2\| + \|F_2\nabla\tilde{q}_1\nabla\tilde{q}_1\| + \|2F_2\nabla\tilde{q}_1\nabla q_1^*\| \\
& + \|G_2\nabla\tilde{q}_1\nabla T_2\| + \|G_2\nabla q_1^*\nabla\tilde{T}_2\| + \|H_2\nabla\tilde{T}_2\nabla T_2\| + \|H_2\nabla\tilde{T}_2\nabla T_2^*\| + \|R_2\|\Big] \\
\leq\; & K\Big[C_2(\sigma+h) + h\overline{s}^2\|q_2^*\|\|\tilde{q}_1\| + h\overline{s}^2\|q_2^*\|\|q_1^*\| + h\overline{s}^2\|q_2^*\|\|q_2^*\| + 2h\overline{s}^2\|q_2^*\|\|\tilde{q}_1\| \\
& + 4\overline{s}^2\|q_2^*\|\|\tilde{T}_2\| + h\|\tilde{q}_1\| + \|\tilde{T}_2\| + h\overline{s}^2\|\tilde{q}_1\|\|\tilde{q}_1\| + 2h\overline{s}^2\|\tilde{q}_1\|\|q_1^*\| + h\overline{s}^2\|\tilde{q}_1\|\|T_2\| \\
& + h\overline{s}^2\|q_1^*\|\|\tilde{T}_2\| + \overline{s}^2\|\tilde{T}_2\|\|T_2\| + \overline{s}^2\|\tilde{T}_2\|\|T_2^*\| + C^*h\Big] \\
\leq\; & K\Big[M^*(\sigma+h) + M^*h + M^*h + M^*h + M^*h + 4\overline{s}^2\|q_2^*\|\big[Nh\cdot KM^*(16\eta) + 2\xi\big] \\
& + M^*h + \big[Nh\cdot KM^*(16\eta) + 2\xi\big] + M^*h + M^*h \\
& + h\overline{s}^2\|\tilde{q}_1\|\big[Nh\cdot KM^*(16\eta) + \max_{0\leq j\leq 1}\|q_j^*\| + \xi\big] + h\overline{s}^2\|q_1^*\|\big[Nh\cdot KM^*(16\eta) + 2\xi\big] \\
& + \overline{s}^2\big[Nh\cdot KM^*(16\eta) + 2\xi\big]\big[Nh\cdot KM^*(16\eta) + \max_{0\leq j\leq 1}\|q_j^*\| + \xi\big] \\
& + \overline{s}^2\big[Nh\cdot KM^*(16\eta) + 2\xi\big]\big[\max_{0\leq j\leq 1}\|q_j^*\| + \xi\big] + M^*h\Big] \\
\leq\; & K\Big[M^*(\sigma+h) + M^*h + M^*h + M^*h + M^*h + (M^*\eta + M^*\xi) + M^*h \\
& + (M^*\eta + M^*\xi) + M^*h + M^*h + M^*h + M^*h + (M^*\eta + M^*\xi) \\
& + (M^*\eta + M^*\xi) + M^*h\Big] \\
\leq\; & KM^*(\sigma + h + h + h + h + h + \eta + \xi + h + \eta + \xi + h + h + h + h + \eta + \xi \\
& + \eta + \xi + h) \\
\leq\; & KM^*(20\eta)\,.
\end{aligned}
$$

Hence

$$
\|q_{2,1}^s\| = \|\tilde{q}_{2,1} + q_2^*\| \leq \|\tilde{q}_{2,1}\| + \|q_2^*\| \leq KM^*(20\eta) + M^* \leq 2M^*\,. \tag{A.15}
$$

Now we estimate $\tilde{q}_{2,k}$. Assume that

$$
\|\tilde{q}_{2,k-1}\| \leq KM^*(16\eta) \quad \text{and} \quad \|q_{2,k-1}^s\| \leq 2M^*\,. \tag{A.16}
$$

Set in equation (2.46) $n = 2$ and subtract it from (2.36) at $n = 2$. We obtain

$$\Delta \tilde{q}_{2,k} - A_2 \nabla \tilde{q}_{2,k} \nabla \tilde{q}_{2,k-1} - A_2 \nabla \tilde{q}_{2,k} \nabla q_1^* - B_2 \nabla \tilde{q}_{2,k} \nabla \tilde{q}_1 - B_2 \nabla \tilde{q}_{2,k} \nabla q_1^* - C_2 \nabla \tilde{q}_{2,k} \nabla T_2$$

$$= A_2 \nabla q_2^* \nabla \tilde{q}_{2,k-1} + A_2 \nabla q_2^* \nabla q_1^* - A_2 \nabla q_2^* \nabla q_2^* + B_2 \nabla q_2^* \nabla \tilde{q}_1 + C_2 \nabla q_2^* \nabla \tilde{T}_2$$

$$+ D_2 \Delta \tilde{q}_1 + E_2 \Delta \tilde{T}_2 - F_2 \nabla \tilde{q}_1 \nabla \tilde{q}_1 - 2 F_2 \nabla \tilde{q}_1 \nabla q_1^*$$

$$- G_2 \nabla \tilde{q}_1 \nabla T_2 - G_2 \nabla q_1^* \nabla \tilde{T}_2 - H_2 \nabla \tilde{T}_2 \nabla T_2 - H_2 \nabla \tilde{T}_2 \nabla T_2^* - R_2 \,. \qquad (A.17)$$

Since

$$
\begin{aligned}
\|A_2 \nabla \tilde{q}_{2,k-1}\| &\leq h \bar{s}^2 \|\tilde{q}_{1,k-1}\| \leq M^* \\
\|A_2 \nabla q_1^*\| &\leq h \bar{s}^2 \|q_1^*\| \leq M^* \\
\|B_2 \nabla \tilde{q}_1\| &\leq 2 h \bar{s}^2 \|\tilde{q}_1\| \leq M^* \\
\|B_2 \nabla q_1^*\| &\leq 2 h \bar{s}^2 \|q_1^*\| \leq M^* \\
\|C_2 \nabla T_2\| &\leq 4 \bar{s}^2 \|T_2\| \ \leq 4 \bar{s}^2 \big[N h \cdot K M^* (16 \eta) + \max_{0 \leq j \leq 1} \|q_j^*\| + \xi \big] \\
&\leq 4 \bar{s}^2 \big[\eta + \max_{0 \leq j \leq 1} \|q_j^*\| + \xi \big] \ \leq \ M^* \,,
\end{aligned}
$$

by Schauder theorem, we have

$$
\begin{aligned}
\|\tilde{q}_{2,k}\| \ \leq \ & K \Big[\|\tilde{\psi}_2\| + \|A_2 \nabla q_2^* \nabla \tilde{q}_{2,k-1}\| + \|A_2 \nabla q_2^* \nabla q_1^*\| + \|A_2 \nabla q_2^* \nabla q_2^*\| + \|B_2 \nabla q_2^* \nabla \tilde{q}_1\| \\
& + \|C_2 \nabla q_2^* \nabla \tilde{T}_2\| + \|D_2 \Delta \tilde{q}_1\| + \|E_2 \Delta \tilde{T}_2\| + \|F_2 \nabla \tilde{q}_1 \nabla \tilde{q}_1\| + \|2 F_2 \nabla \tilde{q}_1 \nabla q_1^*\| \\
& + \|G_2 \nabla \tilde{q}_1 \nabla T_2\| + \|G_2 \nabla q_1^* \nabla \tilde{T}_2\| + \|H_2 \nabla \tilde{T}_2 \nabla T_2\| + \|H_2 \nabla \tilde{T}_2 \nabla T_2^*\| + \|R_2\| \Big] \\
\leq \ & K \Big[C_2 (\sigma + h) + h \bar{s}^2 \|q_2^*\| \|\tilde{q}_{2,k-1}\| + h \bar{s}^2 \|q_2^*\| \|q_1^*\| + h \bar{s}^2 \|q_2^*\| \|q_2^*\| + 2 h \bar{s}^2 \|q_2^*\| \|\tilde{q}_1\| \\
& + 4 \bar{s}^2 \|q_2^*\| \|\tilde{T}_2\| + h \|\tilde{q}_1\| + \|\tilde{T}_2\| + h \bar{s}^2 \|\tilde{q}_1\| \|\tilde{q}_1\| + 2 h \bar{s}^2 \|\tilde{q}_1\| \|q_1^*\| + h \bar{s}^2 \|\tilde{q}_1\| \|T_2\| \\
& + h \bar{s}^2 \|q_1^*\| \|\tilde{T}_2\| + \bar{s}^2 \|\tilde{T}_2\| \|T_2\| + \bar{s}^2 \|\tilde{T}_2\| \|T_2^*\| + C^* h \Big]
\end{aligned}
$$

$$\|\tilde{q}_{2,k}\| \leq K\Big[M^*(\sigma + h) + M^*h + M^*h + M^*h + M^*h + (M^*\eta + M^*\xi) + M^*h$$

$$+(M^*\eta + M^*\xi) + M^*h + M^*h + M^*h + M^*h + (M^*\eta + M^*\xi)$$

$$+(M^*\eta + M^*\xi) + M^*h\Big]$$

$$\leq KM^*(\sigma + h + h + h + h + h + \eta + \xi + h + \eta + \xi + h + h + h + h + \eta + \xi$$

$$+\eta + \xi + h)$$

$$\leq KM^*(20\eta).$$

Hence

$$\|q^s_{2,k}\| = \|\tilde{q}_{2,k} + q^*_2\| \leq \|\tilde{q}_{2,k}\| + \|q^*_2\| \leq KM^*(20\eta) + M^* \leq 2M^*. \tag{A.18}$$

And therefore we finally have

$$\|\tilde{q}_2\| \leq KM^*(20\eta) \quad \text{and} \quad \|q^s_2\| \leq 2M^*. \tag{A.19}$$

We now estimate the function $\tilde{q}_{n,k}$. Assume that

$$\|\tilde{q}_{n-1}\| \leq KM^*(20\eta) \quad, \quad \|q^s_{n-1}\| \leq 2M^* \tag{A.20}$$

and

$$\|\tilde{q}_{n,k-1}\| \leq KM^*(20\eta) \quad, \quad \|q^s_{n,k-1}\| \leq 2M^*. \tag{A.21}$$

Subtract equation (2.46) from (2.36), we obtain

$$\Delta\tilde{q}_{n,k} - A_n\nabla\tilde{q}_{n,k}\nabla\tilde{q}_{n,k-1} - A_n\nabla\tilde{q}_{n,k}\nabla q^*_{n-1}$$

$$-B_n\nabla\tilde{q}_{n,k}\nabla\tilde{q}_{n-1} - B_n\nabla\tilde{q}_{n,k}\nabla q^*_{n-1} - C_n\nabla\tilde{q}_{n,k}\nabla T_n$$

$$= A_n\nabla q^*_n\nabla\tilde{q}_{n,k-1} + A_n\nabla q^*_n\nabla q^*_{n-1} - A_n\nabla q^*_n\nabla q^*_n + B_n\nabla q^*_n\nabla\tilde{q}_{n-1} + C_n\nabla q^*_n\nabla\tilde{T}_n$$

$$+D_n\Delta\tilde{q}_{n-1} + E_n\Delta\tilde{T}_n - F_n\nabla\tilde{q}_{n-1}\nabla\tilde{q}_{n-1} - 2F_n\nabla\tilde{q}_{n-1}\nabla q^*_{n-1}$$

$$-G_n\nabla\tilde{q}_{n-1}\nabla T_n - G_n\nabla q^*_{n-1}\nabla\tilde{T}_n - H_n\nabla\tilde{T}_n\nabla T_n - H_n\nabla\tilde{T}_n\nabla T^*_n - R_n. \tag{A.22}$$

Since

$$
\begin{aligned}
\|A_n \nabla \tilde{q}_{n,k-1}\| &\leq h\overline{s}^2 \|\tilde{q}_{n,k-1}\| \leq M^* \\
\|A_n \nabla q^*_{n-1}\| &\leq h\overline{s}^2 \|q^*_{n-1}\| \leq M^* \\
\|B_n \nabla \tilde{q}_{n-1}\| &\leq 2h\overline{s}^2 \|\tilde{q}_{n-1}\| \leq M^* \\
\|B_n \nabla q^*_{n-1}\| &\leq 2h\overline{s}^2 \|q^*_{n-1}\| \leq M^* \\
\|C_n \nabla T_n\| &\leq 4\overline{s}^2 \|T_n\| \leq 4\overline{s}^2 \Big[Nh \cdot KM^*(16\eta) + \max_{0 \leq j \leq n-1} \|q^*_j\| + \xi \Big] \\
&\leq 4\overline{s}^2 \Big[\eta + \max_{0 \leq j \leq n-1} \|q^*_j\| + \xi \Big] \leq M^*,
\end{aligned}
$$

by Schauder theorem, we have

$$
\begin{aligned}
\|\tilde{q}_{n,k}\| &\leq K\Big[\|\tilde{\psi}_n\| + \|A_n \nabla q^*_n \nabla \tilde{q}_{n,k-1}\| + \|A_n \nabla q^*_n \nabla q^*_{n-1}\| + \|A_n \nabla q^*_n \nabla q^*_n\| \\
&\quad + \|B_n \nabla q^*_n \nabla \tilde{q}_{n-1}\| + \|C_n \nabla q^*_n \nabla \tilde{T}_n\| + \|D_n \Delta \tilde{q}_{n-1}\| + \|E_n \Delta \tilde{T}_n\| \\
&\quad + \|F_n \nabla \tilde{q}_{n-1} \nabla \tilde{q}_{n-1}\| + \|2F_n \nabla \tilde{q}_{n-1} \nabla q^*_{n-1}\| + \|G_n \nabla \tilde{q}_{n-1} \nabla T_n\| \\
&\quad + \|G_n \nabla q^*_{n-1} \nabla \tilde{T}_n\| + \|H_n \nabla \tilde{T}_n \nabla T_n\| + \|H_n \nabla \tilde{T}_n \nabla T^*_n\| + \|R_n\| \Big] \\
&\leq K\Big[C_n(\sigma + h) + h\overline{s}^2 \|q^*_n\| \|\tilde{q}_{n,k-1}\| + h\overline{s}^2 \|q^*_n\| \|q^*_{n-1}\| + h\overline{s}^2 \|q^*_n\| \|q^*_n\| \\
&\quad + 2h\overline{s}^2 \|q^*_n\| \|\tilde{q}_{n-1}\| + 4\overline{s}^2 \|q^*_n\| \|\tilde{T}_n\| + h\|\tilde{q}_{n-1}\| + \|\tilde{T}_n\| + h\overline{s}^2 \|\tilde{q}_{n-1}\| \|\tilde{q}_{n-1}\| \\
&\quad + 2h\overline{s}^2 \|\tilde{q}_{n-1}\| \|q^*_{n-1}\| + h\overline{s}^2 \|\tilde{q}_{n-1}\| \|T_n\| + h\overline{s}^2 \|q^*_{n-1}\| \|\tilde{T}_n\| \\
&\quad + \overline{s}^2 \|\tilde{T}_n\| \|T_n\| + \overline{s}^2 \|\tilde{T}_n\| \|T^*_n\| + C^* h \Big] \\
&\leq K\Big[M^*(\sigma + h) + M^* h + M^* h + M^* h + M^* h + (M^*\eta + M^*\xi) + M^* h \\
&\quad + (M^*\eta + M^*\xi) + M^* h + M^* h + M^* h + M^* h + (M^*\eta + M^*\xi) \\
&\quad + (M^*\eta + M^*\xi) + M^* h \Big] \\
&\leq KM^*(\sigma + h + h + h + h + h + \eta + \xi + h + \eta + \xi + h + h + h + h + \eta + \xi \\
&\quad + \eta + \xi + h) \\
&\leq KM^*(20\eta).
\end{aligned}
$$

Hence

$$\|q_{n,k}^s\| = \|\tilde{q}_{n,k} + q_n^*\| \leq \|\tilde{q}_{n,k}\| + \|q_n^*\| \leq KM^*(20\eta) + M^* \leq 2M^*. \qquad \text{(A.23)}$$

And therefore we finally have

$$\|\tilde{q}_n\| \leq KM^*(20\eta) \quad \text{and} \quad \|q_n^s\| \leq 2M^*. \qquad \text{(A.24)}$$

Estimates (A.24) completes the proof of this theorem. $\square$

APPENDIX B

ADDITIONAL FIGURES

In this appendix, we present some additional figure that we mention in section 4.2 and the last section show figure of $a_i(\boldsymbol{x})$ in each iterations for improving quality of tail.

B.1   Example #1

Reconstruction of example #1 using actual tail is shown in figure B.1, 2% noise is added to the boundary data. For the no noise case, we had show the reconstruction using approximated tail, section 3.3.2, in figure B.2. We show the comparison between actual tail and approximated tail in figure B.3. And lastly, graph of difference between two consecutive of $a_i(\boldsymbol{x})$ and comparing $a_i(\boldsymbol{x})$ with $a^*(\boldsymbol{x})$ are showed in figure B.4.
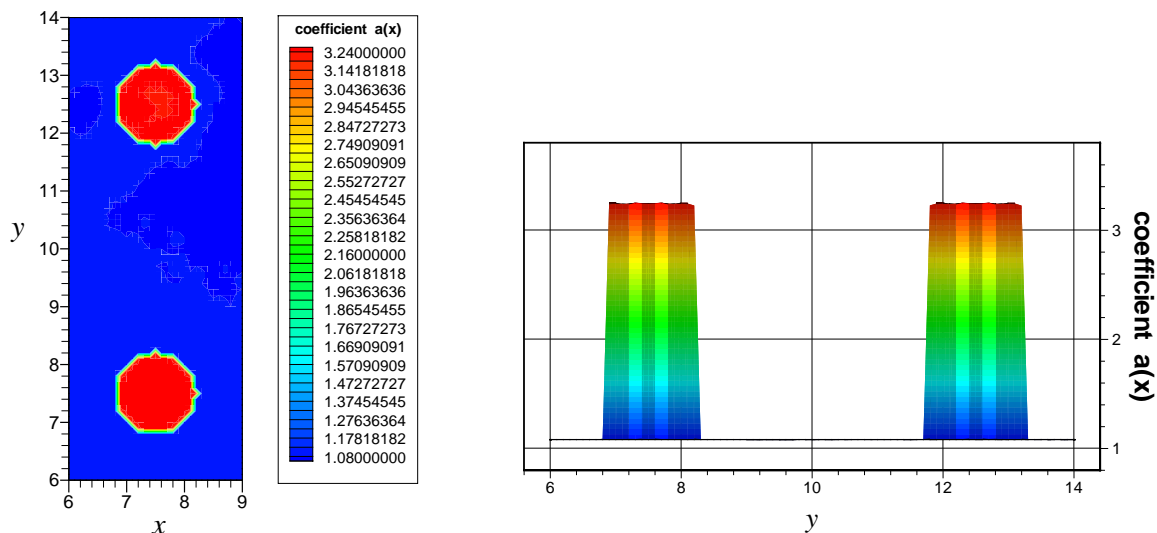
Peak value of left inclusion is 3.264 and right inclusion is 3.265.

Figure B.1. Shows reconstruction result with 2% noise using actual tail-function of example #1.
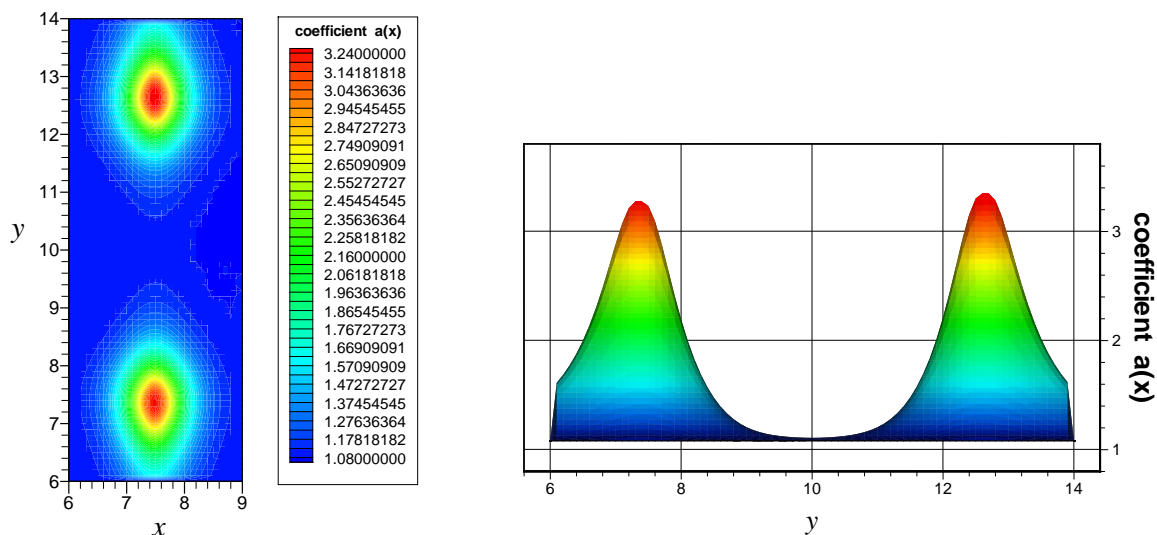
Peak value of left inclusion is 3.59 and right inclusion is 3.643.

Figure B.2. Shows reconstruction result without noise using approximated tail of example #1.

(a)   (b)
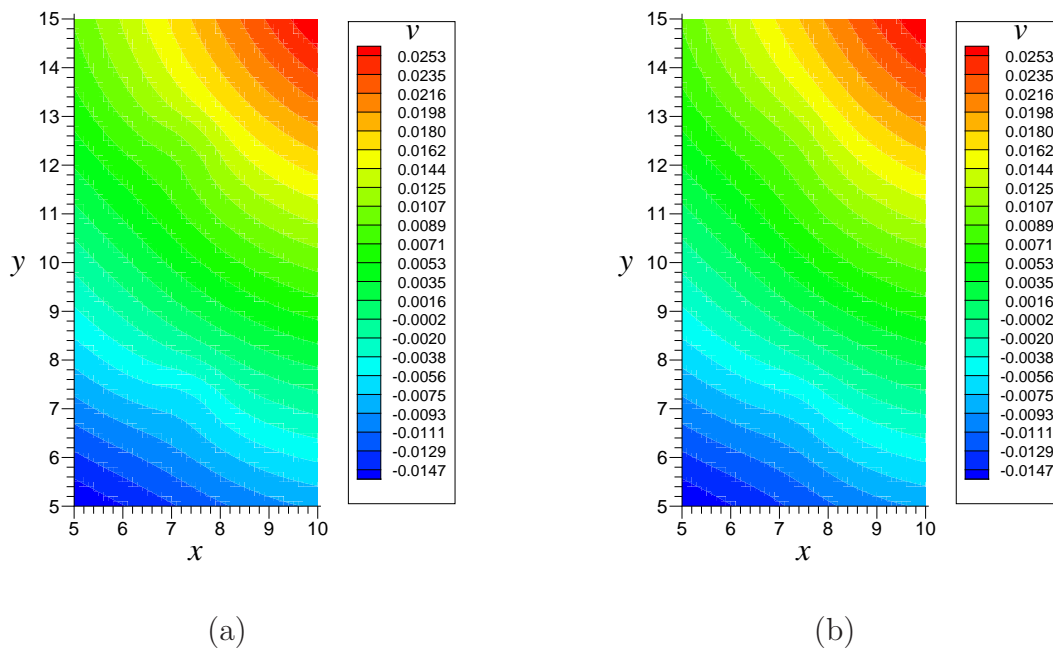
Figure B.3. Comparison between actual tail, $u(\boldsymbol{x}, s_0)$ (a) and approximated tail, $u_\infty(\boldsymbol{x})(b)$ of example#1.
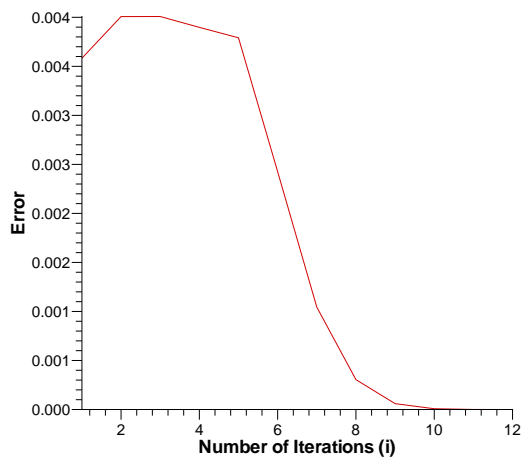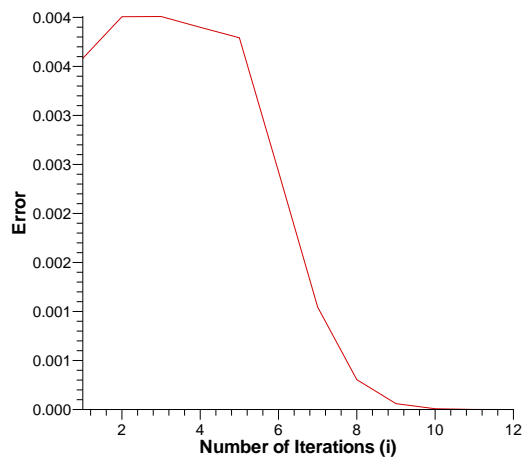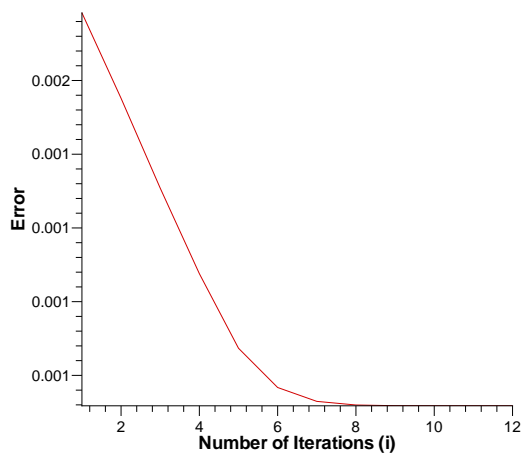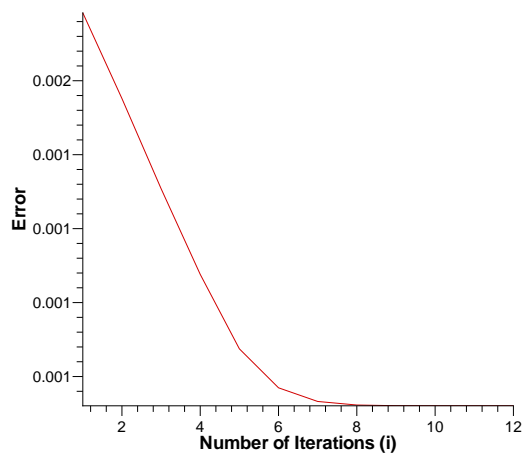
Figure B.4. Example #1 results, (a) Different between two consecutive of $a_i(\boldsymbol{x})$ in equation (3.39) of light s_0. (b) Different between two consecutive of $a_i(\boldsymbol{x})$ in equation (3.39) of light s_6. (c) Relative of $a_i(\boldsymbol{x})$ in equation (3.39) comparing with $a^*(\boldsymbol{x})$ of light s_0. (d) Relative of $a_i(\boldsymbol{x})$ in equation (3.39) comparing with $a^*(\boldsymbol{x})$ of light s_6.

B.2   Example #2

Reconstruction of example #2 using actual tail is shown in figure B.5, 2% noise is added to the boundary data. For the no noise case, we had show the reconstruction using approximated tail, section 3.3.2, in figure B.6. We show the comparison between actual tail and approximated tail in figure B.7. And lastly, graph of difference between two consecutive of $a_i(\boldsymbol{x})$ and comparing $a_i(\boldsymbol{x})$ with $a^*(\boldsymbol{x})$ are showed in figure B.8.
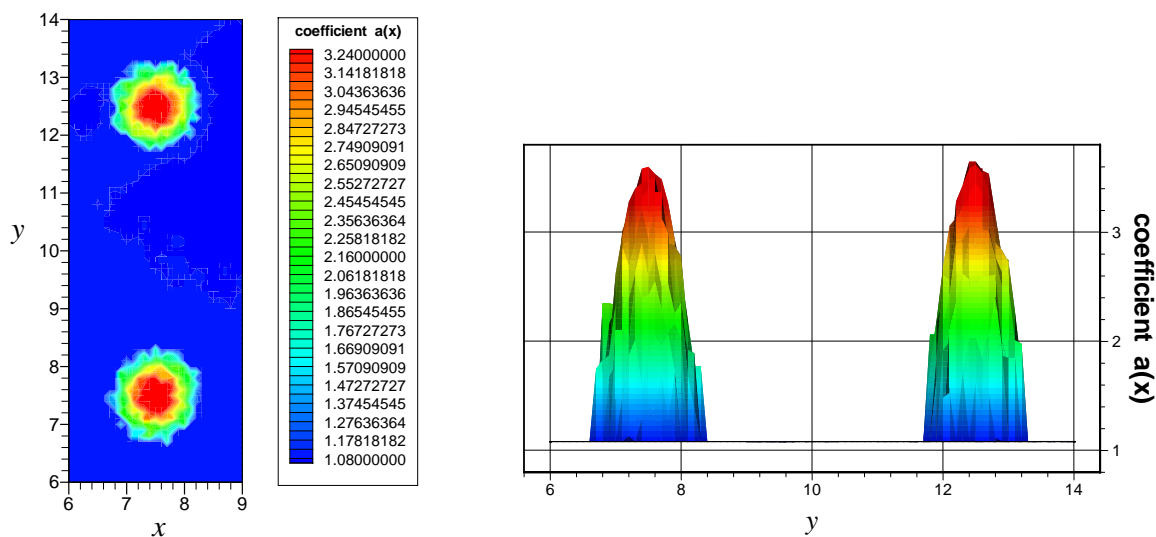
Average of left inclusion is 3.595 and right inclusion is 3.643.

Figure B.5. Shows reconstruction result with 2% noise using actual tail-function of example #2.
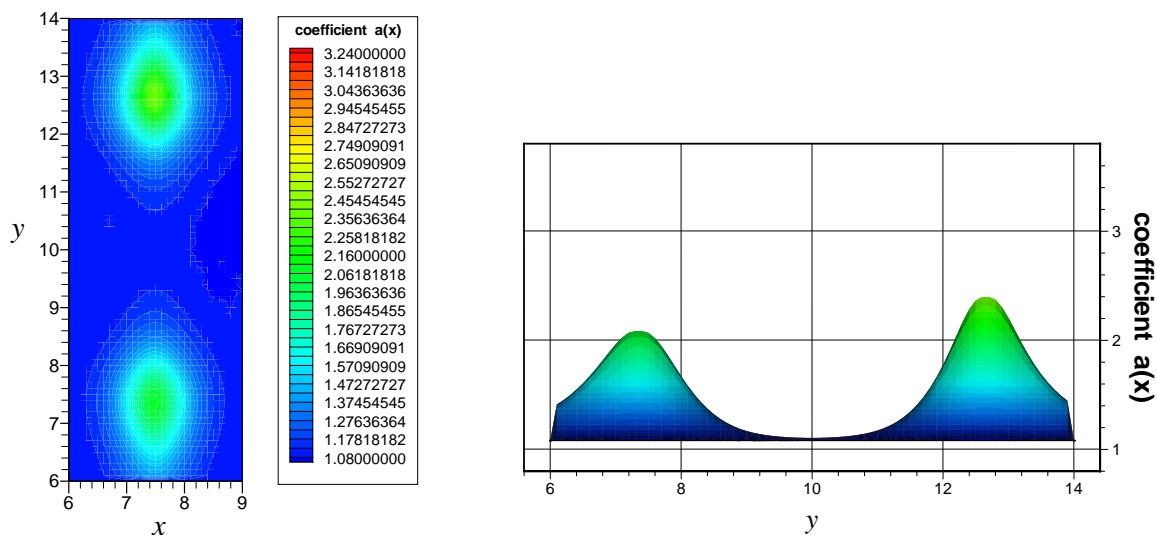
Peak value of left inclusion is 2.082 and right inclusion is 3.343.

Figure B.6. Shows reconstruction result without noise using approximated tail of example #2.

(a)   (b)
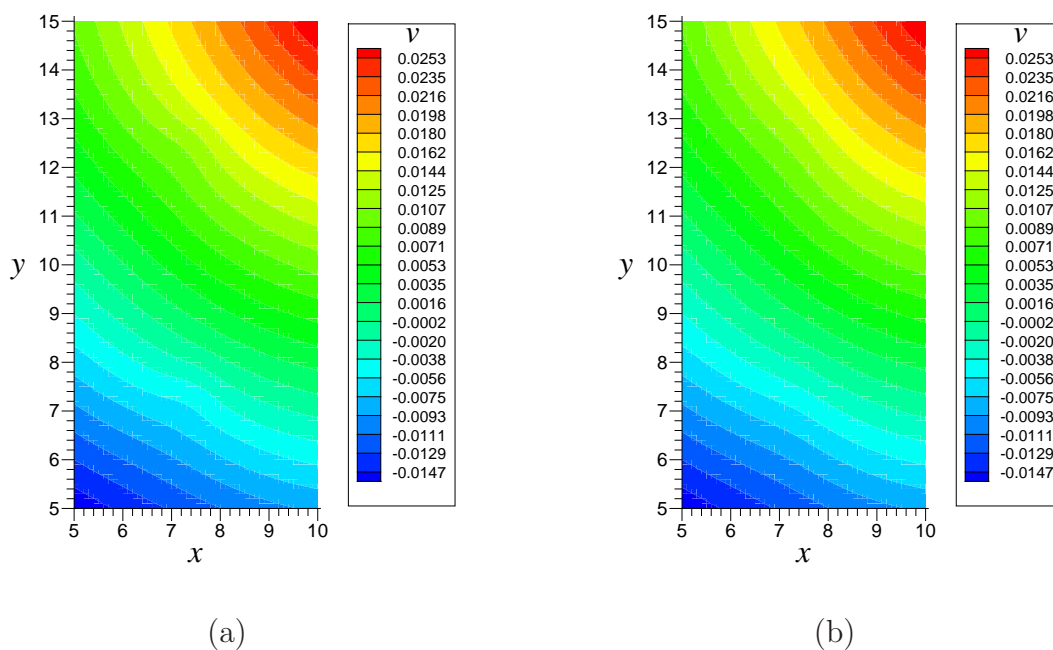
Figure B.7. Comparison between actual tail, $u(\boldsymbol{x}, s_0)$ (a) and approximated tail, $u_\infty(\boldsymbol{x})$ (b) of example#2.
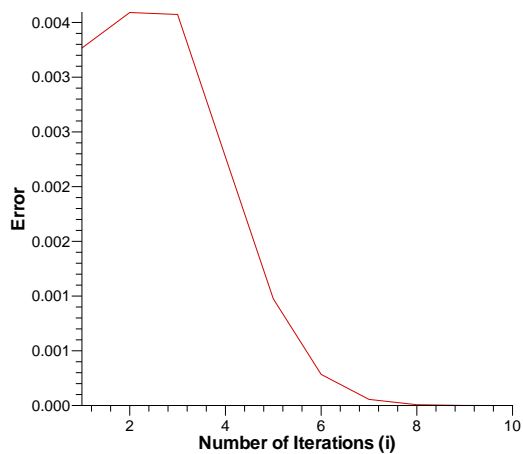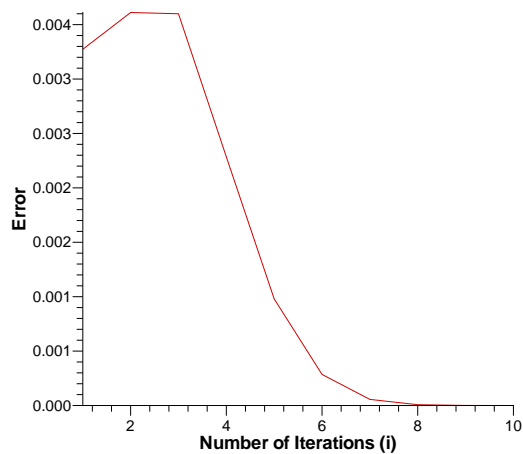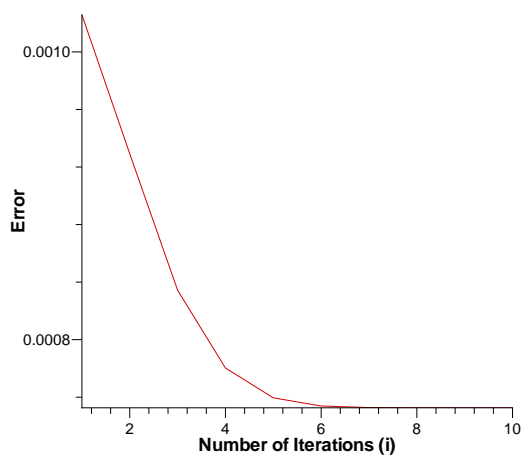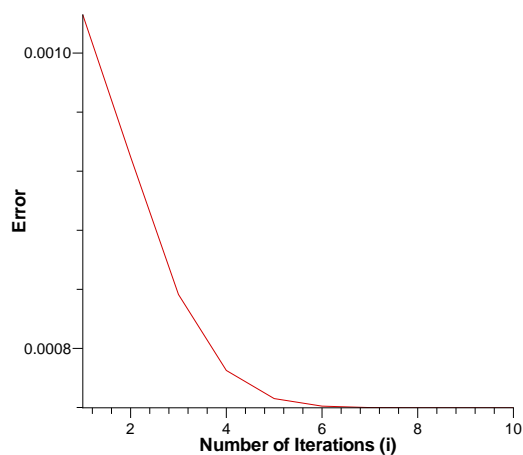
Figure B.8. Example #2 results, (a) Different between two consecutive of $a_i(\boldsymbol{x})$ in equation (3.39) of light s_0. (b) Different between two consecutive of $a_i(\boldsymbol{x})$ in equation (3.39) of light s_6. (c) Relative of $a_i(\boldsymbol{x})$ in equation (3.39) comparing with $a^*(\boldsymbol{x})$ of light s_0. (d) Relative of $a_i(\boldsymbol{x})$ in equation (3.39) comparing with $a^*(\boldsymbol{x})$ of light s_6.

B.3   Figure of the Iterations for Improving Quality of Tail

In this section we show figures of $a_i(\boldsymbol{x})$'s in each iterations for improving quality of tail. The $a_i(\boldsymbol{x})$'s we show here are the results from reconstruction process of example #1 with respect to s_0, see figure B.9, B.10, B.11 and B.12. There are totally 13 iterations, see table 4.3. We also show $a_i(\boldsymbol{x})$ of the last iteration with respect to s_6 which is the iteration #13 in figure B.13. Figure B.14, is the average of iteration #13 of s_0 and iteration #13 of s_6.

The result of example #2 are shown only the average of iteration #11 of s_0 and iteration #11 of s_6, see table 4.5. This average is shown in figure B.15.
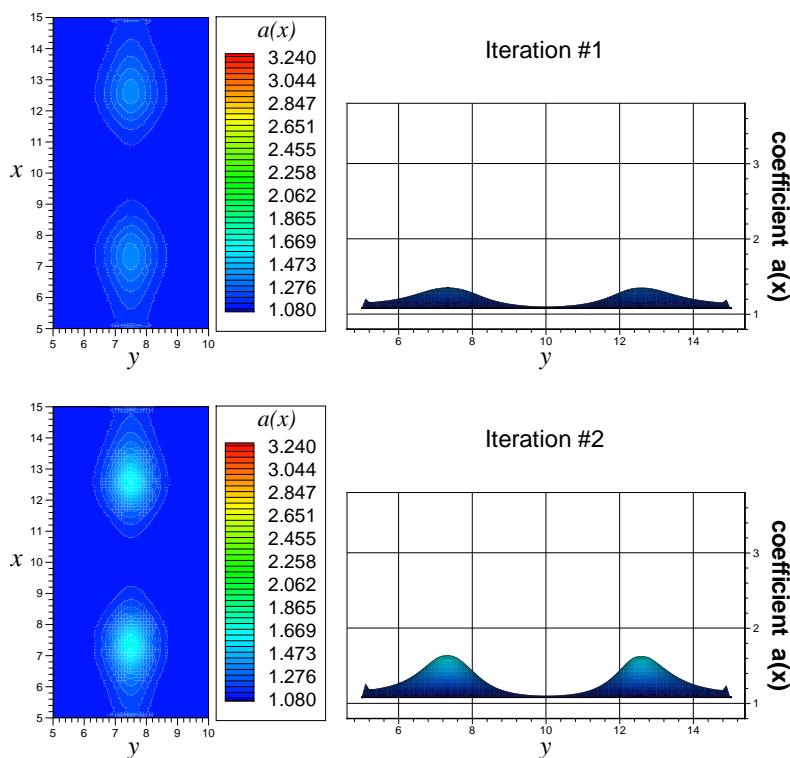
Figure B.9.   Show $a_1(\boldsymbol{x})$ and $a_2(\boldsymbol{x})$ in iterations for improving quality of tail with respect to s_0 of example #1.
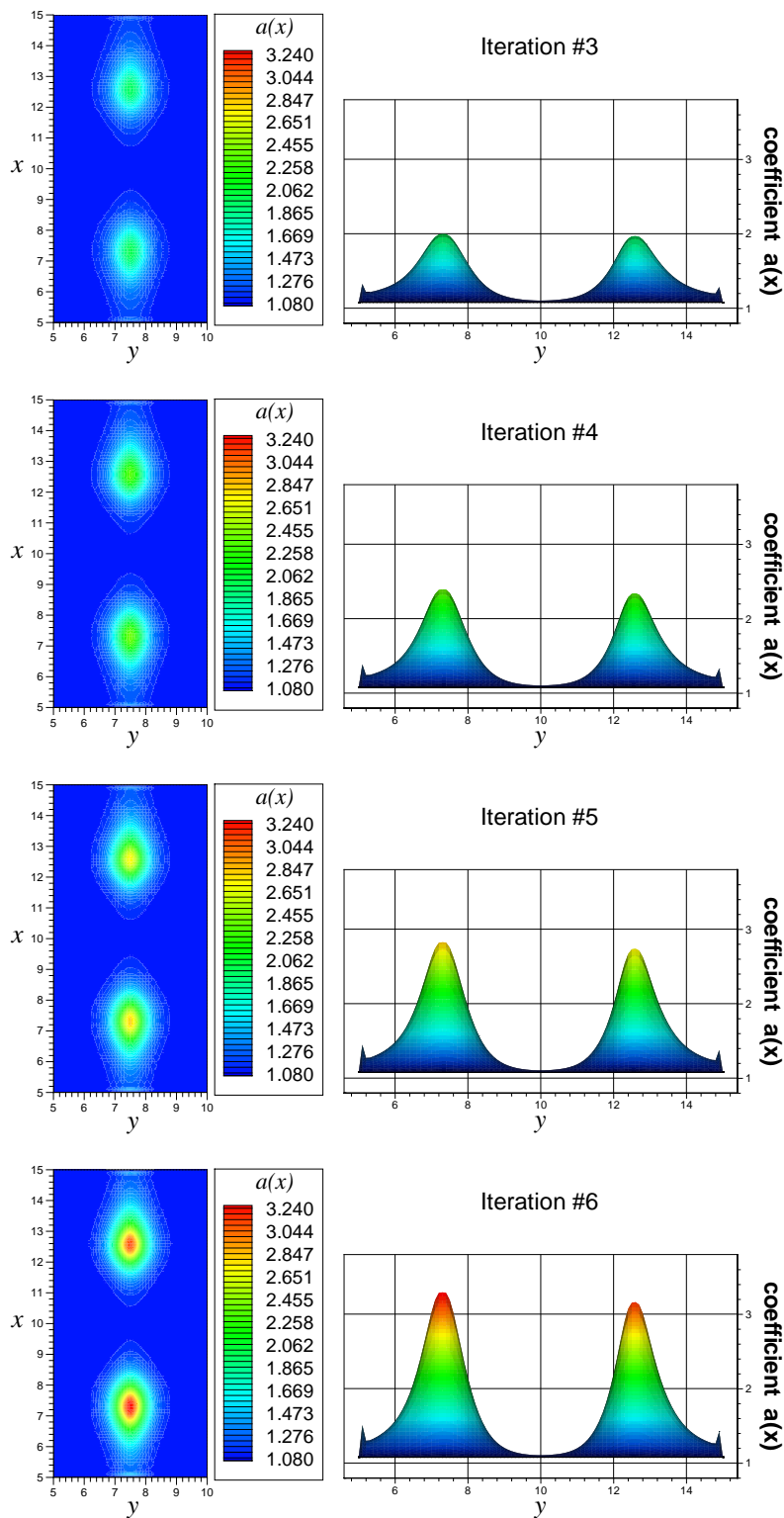
Figure B.10. Show $a_3(\boldsymbol{x})$, $a_4(\boldsymbol{x})$, $a_5(\boldsymbol{x})$ and $a_6(\boldsymbol{x})$ in iterations for improving quality of tail with respect to s_0 of example #1.
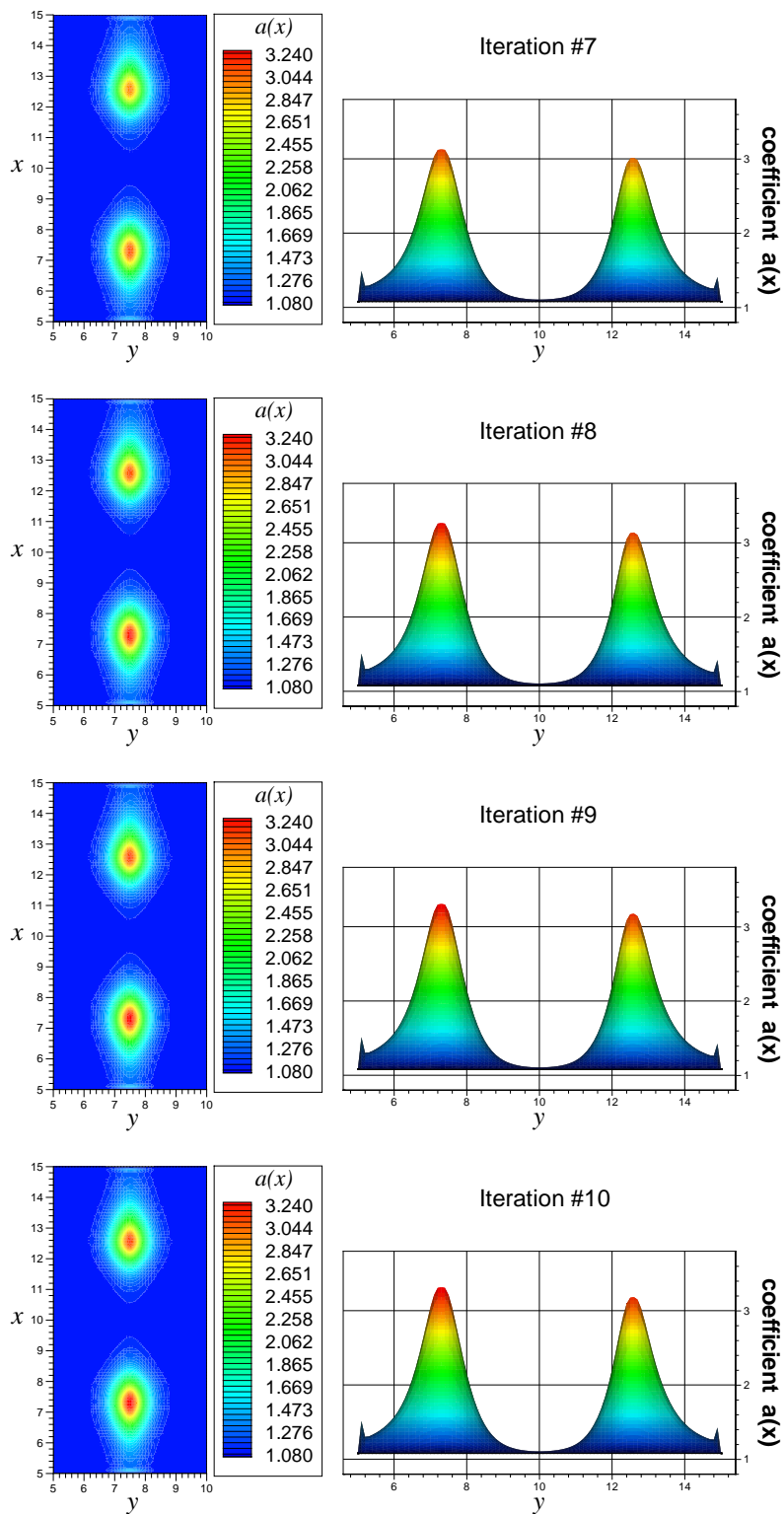
Figure B.11. Show $a_7(\boldsymbol{x})$, $a_8(\boldsymbol{x})$, $a_9(\boldsymbol{x})$ and $a_{10}(\boldsymbol{x})$ in iterations for improving quality of tail with respect to s_0 of example #1.
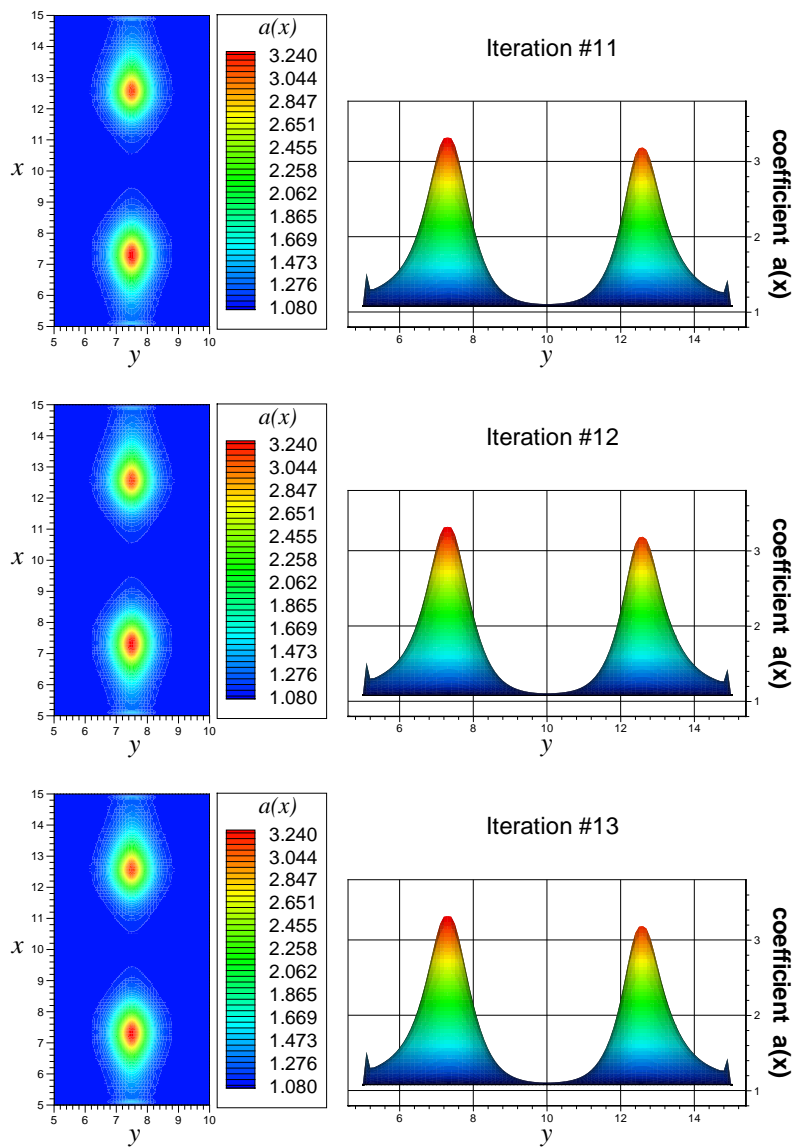
Figure B.12. Show $a_{11}(\boldsymbol{x})$, $a_{12}(\boldsymbol{x})$ and $a_{13}(\boldsymbol{x})$ in iterations for improving quality of tail with respect to s_0 of example #1.
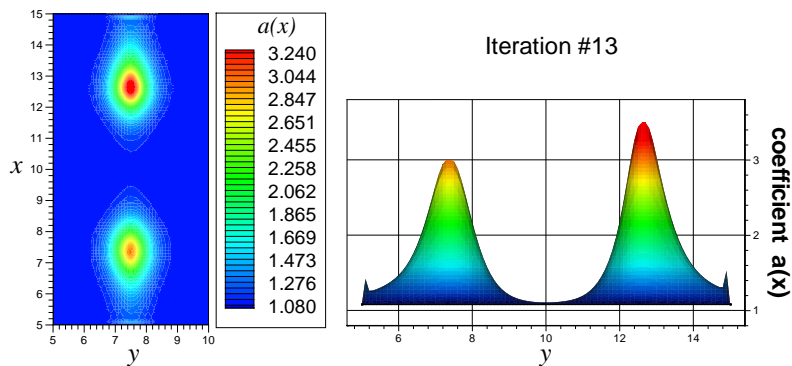
Figure B.13. Show $a_{13}(\boldsymbol{x})$ in iterations for improving quality of tail with respect to s_6 of example #1.
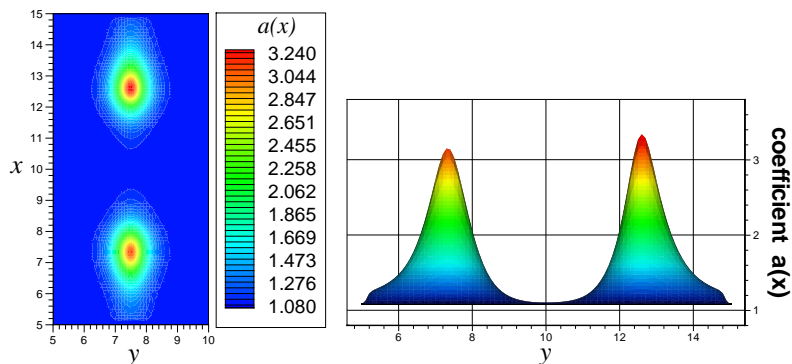
Figure B.14. Show the average of $a_i(\boldsymbol{x})$'s in iteration #13 of s_0 and iteration #13 of s_6 of example #1.
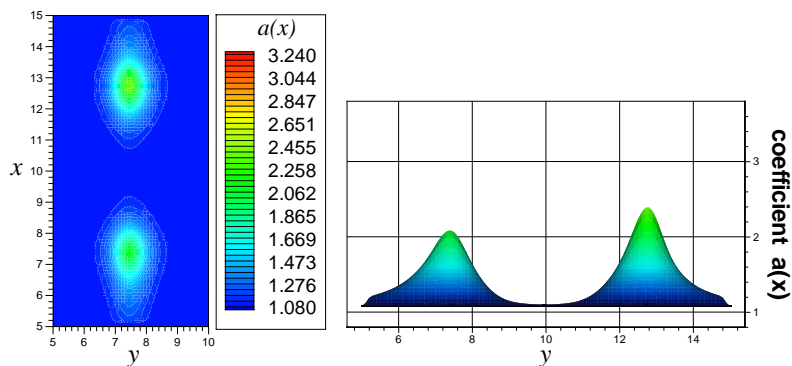
Figure B.15. Show the average of $a_i(\boldsymbol{x})$'s in iteration #11 of s_0 and iteration #11 of s_6 of example #2.

REFERENCES

[1] S. Arridge, "Optical tomography in medical imaging," *Inverse Problems*, vol. 15, pp. 841–893, 1999.

[2] A. B. Bakushinsky, T. Khan, and A. Smirnova, "Inverse problem in optical tomography and its numerical investigation by iteratively regularized methods," *J. Inv. Ill-Posed Problems*, vol. 13, pp. 537–551, 2005.

[3] Yu. A. Grazin, M. V. Klibanov, and T. R. Lucas, "Numerical solution of a subsurface imaging inverse problem," *SIAM J. Appl. Math.*, vol. 62, pp. 664–683, 2001.

[4] E. Haber, U. M. Asher, and D. Oldenburg, "On optimization techniques for solving nonlinear inverse problems," *Inverse Problems*, vol. 16, pp. 1263–1280, 2000.

[5] M. V. Klibanov and A. Timonov, *Carleman Estimates for Coefficient Inverse Problems and Numerical Applications*. Utrecht: VSP, 2004.

[6] H. Shan, M. V. Klibanov, H. Liu, N. Pantong, and J. Su, "Numerical implementation of the convexification algorithm for an optical diffusion tomograph," *Inverse Problems*, vol. 24, p. 025006, 2008.

[7] H. Shan, M. V. Klibanov, N. Pantong, J. Su, and H. Liu, "A globally accelerated numerical method for optical tomography with continuous wave source," *J. Inv. Ill-Posed Problems*, vol. 16, pp. 765–792, 2008.

[8] N. Pantong, J. Su, H. Shan, M. V. Klibanov, and H. Liu, "Globally accelerated reconstruction algorithm for diffusion tomography with continuous-wave source

in an arbitrary convex shape domain," *J. Optical Society of America A*, vol. 26, pp. 456–472, 2009.

[9] L. Beilina and M. V. Klibanov, "A globally convergent numerical method for a coefficient inverse problem," *SIAM J. Sci. Comp.*, vol. 31, pp. 478–509, 2008.

[10] H. B. Keller and D. J. Perozzi, "Fast seismic ray tracing," *SIAM J. Appl. Math.*, vol. 43, pp. 981–992, 1983.

[11] R. R. Alfano, R. R. Pradhan, , and G. C. Tang, "Optical spectroscopic diagnosis of cancer and normal breast tissues," *J. Opt. Soc. Am.*, vol. B 6, pp. 1015–1023, 1989.

[12] S. Srinivasan, B. W. Pogue, B. Brooksby, S. Jiang, H. Dehghani, C. Kogel, S. P. Poplack, and K. D. Paulsen, "Near-infrared characterization of breast tumors in vivo using spectrally-constrained reconstruction," *Technol. Cancer Res. Treatment*, vol. 4, pp. 513–526, 2005.

[13] S. Srinivasan, B. W. Pogue, H. Dehghani, S. Jiang, X. Song, and K. D. Paulsen, "Improved quantification of small objects in near-infrared diffuse optical tomography," *J. Biomed. Opt.*, vol. 9, pp. 1161–1171, 2004.

[14] C. Schmitz, D. Klemer, R. Hardin, M. Katz, Y. Pei, H. Graber, M. Levin, R. Levina, N. Franco, W. Solomon, and R. Barbour, "Design and implementation of dynamic nearinfrared optical tomographic imaging instrumentation for simultaneous dual-breast measurements," *Appl. Opt.*, vol. 44, pp. 2140–2153, 2005.

[15] Y. Xu, X. Gu, L. Fajardo, and H. Jiang, "In vivo breast imaging with diffuse optical tomography based on higherorder diffusion equations," *Appl. Opt.*, vol. 42, pp. 3163–3169, 2003.

[16] A. Godavarty, A. B. T. Jr., R. Roy, M. Gurfinkel, M. J. Eppstein, C. Zhang, and E. M. Sevick-Muraka, "Diagnostic imaging of breast cancer using fluores-

cenceenhanced optical tomography: phantom studies," *J. Biomed. Opt.*, vol. 9, pp. 488–496, 2004.

[17] A. Y. Bluestone, M. Stewart, J. Lasker, G. S. Abdoulaev, and A. H. Hielscher, "Three-dimensional optical tomographic brain imaging in small animals part 1: hypercapnia," *J. Biomed. Opt.*, vol. 9, pp. 1046–1062, 2004.

[18] S. Gopinath, C. S. Robertson, R. G. Grossman, and B. Chance, "Near-infrared spectroscopic localization of intracranial hematomas," *J. Neurosurg*, vol. 79, pp. 43–47, 1993.

[19] G. Zhang, A. Katz, R. R. Alfano, A. D. Kofinas, P. G. Stubblefield, W. Rosenfeld, D. Beyer, D. Maulik, and M. R. Stankovic, "Brain perfusion monitoring with frequencydomain and continuous-wave near-infrared spectroscopy: a cross-correlation study in newborn piglets," *Phys. Med. Biol.*, vol. 45, pp. 3143–3158, 2000.

[20] A. G. Yodh and D. A. Boas, "Functional imaging with diffusing light," in *Biomedical Photonics Handbook*, t. vo-dinh ed. ed. CRC Press, 2003.

[21] B. Chance, E. Anday, S. Nioka, S. Zhou, L. Hong, K. Worden, C. Li, T. Murray, Y. Ovetsky, D. Pidikiti, and R. Thomas, "A novel method for fast imaging of brain function non-invasively with light," *Opt. Express*, vol. 2, pp. 411–423, 1998.

[22] D. A. Boas, T. Gaudette, G. Strangman, X. Cheng, J. J. A. Marota, and J. B. Mandeville, "The accuracy of near infrared spectroscopy and imaging during focal changes in cerebral hemodynamics," *Neuroimage*, vol. 13, pp. 76–90, 2001.

[23] T. O. McBride, B. W. Pogue, S. Jiang, U. L. Österberg, and K. D. Paulsen, "Initial studies of in vivo absorbing and scattering heterogeneity in near-infrared tomographic breast imaging," *Opt. Lett.*, vol. 26, pp. 822–824, 2001.

[24] M. Solonenko, R. Cheung, T. M. Busch, A. Kachur, G. M. Griffin, T. Vulcan, T. C. Zhu, H. W. Wang, S. M. Hahn, and A. G. Yodh, "In vivo reflectance

measurement of optical properties blood oxygenation and motexafin lutetium uptake in canine large bowels kidneys and prostates," *Phys. Med. Biol.*, vol. 47(6), pp. 857–73, 2002.

[25] K. L. Du, R. Mick, T. M. Busch, T. C. Zhu, J. C. Finlay, G.Yu, A. G. Yodh, S. B. Malkowicz, D. Smith, R. Whittington, D. Stripp, and S. M. Hahn, "Preliminary results of interstitial motexafin lutetium-mediated pdt for prostate cancer," *Lasers Surg. Med.*, vol. 38, pp. 427–34, 2006.

[26] W. B. Wang, J. H. Ali, J. H. Vitenson, J. M. Lombardo, and R. R. Alfano, "Spectral polarization imaging of human rectum-membrane-prostate tissues," *IEEE J. Select. Topics Quantum Electron.*, vol. 9, pp. 288–293, 2003.

[27] W. B. Wang, J. H. Ali, M. Zevallos, and R. R. Alfano, "Near infrared imaging of human prostate cancerous and normal tissues based on water absorption," in *Advances in Optical Imaging and Photon Migration (CD-ROM)*. Optical Society of America, 2004.

[28] B. Chance, "High sensitivity and specificity in human breast cancer detection with near-infrared imaging," in *Biomedical Topical Meeting*, vol. 71 in osa trends in optics and photonics ed. Optical Society of America, 2002, pp. 450–455.

[29] S. R. Arridge and J. C. Hebden, "Optical imaging in medicine: Ii. modeling and reconstruction," *Phys. Med. Biol.*, vol. 42, pp. 841–853, 1997.

[30] D. Grosenick, H. Wabnitz, H. H. Rinneberg, K. T. Moesta, and P. M. Schlag, "Development of a time-domain optical mammograph and first in vivo applications," *Applied Optics*, vol. 38, pp. 2827–2943, 1999.

[31] O. A. Ladyzhenskaya and N. N. Uralceva, *Linear and Quasilinear Elliptic Equations*. New York: Academic Press, 1969.

[32] S. I. Kabanikhin, A. D. Satybaev, and M. A. Shishlenin, *Direct Methods of Solving Multidimensional Inverse Hyperbolic Problems*. Utrecht: VSP, 2004.

[33] L. C. Evans, *Partial Differential Equations.* American Mathematical Society, 1998.

BIOGRAPHICAL STATEMENT

Natee Pantong was born in Lamphun, Thailand, in 1973. He received his B.S. degree in Computer Science from The Royal Thai Air Force Academy (RTAFA), Thailand, in 1996, his first M.S. in Computer Science from Asian Institute of Technology, Thailand, in 2000. From 1997 to 2005, he was with the department of Mathematics and Computer Science, RTAFA, as an Instructor in the Computer Programming Languages and System Programming. He got M.S. and Ph.D. degrees in Mathematical Science from The University of Texas at Arlington in 2007 and 2009, respectively. After getting his Ph.D., he joined The University of North Carolina at Charlotte, working as a Postdoctoral Research Associate in Department of Mathematics and Statistics. His current research interest is in the area of Numerical Solution to Inverse Problems and Numerical Computation Scheme with Object Oriented Programming. He is a member of Society for Industrial and Applied Mathematics (SIAM) and American Mathematical Society (AMS).